Università degli Studi di Cagliari

DOTTORATO DI RICERCA

Scienze della Terra

Ciclo XXV

Depositional and welding processes in low aspect ratio ignimbrites: examples from the Sulcis Volcanic District (Sardinia, Italy)

Settore scientifico disciplinari di afferenza

Area 04 - GEO/08

Presentata da:	Dott. Maurizio Mulas
Coordinatore Dottorato	Prof. Marcello Franceschelli
Relatore	Prof. Raffaello Cioni
Tutor	Dott.ssa Laura Pioli

Esame finale anno accademico 2011 – 2012

If you can't be a pine on the top of the hill,

be a shrub in the valley,

but be the best little shrub at the side of the stream;

(...)

It isn't the size that you win or you fail,

be the best of whatever you are.

(Martin Luther King - Be the best of whatever you are)

RIASSUNTO

Le ignimbriti saldate, reomorfiche e di alto grado sono un particolare tipo di deposito da correnti di densità piroclastiche (PDC) solitamente associate ad attività vulcanica esplosiva ad alta intensità (VEI>4). Queste sono caratterizzate da un' alta variabilità delle caratteristiche fisiche e sedimentologiche, che testimoniano differenti meccanismi deposizionali dei PDC e la loro differente risposta alla topografia durante e dopo la fine dei processi deposizionali. Quando le temperature dei depositi sono superiori a quelle dell'intervallo di transizione vetrosa (Tg), i depositi possono subire locali riaggiustamenti per lunghi periodi e le deformazioni avvengono per lo più in maniera plastica.

L'obbiettivo di questa tesi di dottorato è stato quello di investigare quali processi hanno guidato la formazione di ignimbriti saldate da riolitiche a comenditiche, come e quando avvengono i diversi processi reomorfici e quali fattori hanno influenzato la formazione delle principali strutture conservate.

Il distretto Vulcanico del Sulcis (SW della Sardegna - Italia) è un buon laboratorio di terreno dove affiorano 16 ignimbriti saldate ben esposte, ben conservate e non deformate da recenti processi tettonici. Tutte queste caratteristiche permettono di studiare e analizzare i principali processi reomorfici nonostante l'età compresa tra 17.6 e 13.8 Ma. La ricerca ha focalizzato la sua attenzione su tre unità ignimbritiche: l'unità di Punta Senoglio, l'unità di Ventrischio e l'unità di Monte Ulmus. Successivamente ci si è concentrati sull' ignimbrite di Monte Ulmus (MUI) che ha conservato meglio le evidenze legate a questi processi. Tramite lo studio sistematico e dettagliato dei depositi, e la descrizione alle differenti scale e l'analisi dei prodotti, sono state riconosciute le principali fasi eruttive e i principali processi, con una particolare attenzione alla loro cronologia relativa. La MUI mostra evidenze di processi di saldatura e di reomorfismo contemporanei e successivi alla deposizione. Le analisi delle caratteristiche micro-strutturali sulle sezioni sottili mostrano chiare evidenze di un processo deposizionale che varia da aggradazionale graduale a step-wise.

I depositi della MUI conservano perfettamente le strutture primarie tipiche di ignimbriti di alto grado (foliazioni, lineazioni, e variazioni delle litofacies), le strutture tipiche di ignimbriti reomorfiche (frammenti solidi ruotati, pieghe a differente scala, rampe, etc) e strutture legate ai processi di raffreddamento e degassamento (blisters, degassing pipes e facies di devetrificazione).

La MUI è un ignimbrite saldata di alto grado, di composizione da riolitica a trachitica, localmente reomorfica e a basso rapporto di aspetto. Essa affiora principalmente nelle isole di Sant' Antioco e San Pietro e nel Sulcis, su un area di circa 300 km^2 e con un volume minimo stimato intorno ai 2,5 km^3. La più probabile area sorgente è localizzata nel settore settentrionale, alcuni chilometri a nord dell'isola di San Pietro. Sono state distinte quattro principali unità di flusso piroclastico nominate A0, A1, A2 e B, precedute da un deposito di fall basale (F). All'interno della MUI sono state distinte sette principali litofacies che riflettono differenti regimi di flusso dei PDC (da turbolenti a laminari) e differenti processi deposizionali (da deposizione aggradazionale continua a step-wise). Tutte queste litofacies permettono inoltre di ricostruire i diversi processi di saldatura e deformativi. Le proprietà fisiche della MUI risultano essere fortemente influenzate dalle condizioni paleotopografiche (alti o bassi topografici o condizioni pianeggianti). Localmente i depositi registrano rapidi riaggiustamenti in massa, anche in condizioni di piccole pendenze (~10°), durante la deposizione, probabilmente dovuti alla bassa viscosità dei prodotti e alle alte quantità di gas intrappolati, come suggerito dalla frequente presenza di blisters e parting planes. Le basse temperature di transizione vetrosa (~ 415 °C) stimate per i prodotti della MUI giustificano una permanenza degli stessi allo stato plastico per lunghi periodi, favorendone la rimobilizzazione per lunghi periodi dopo la fine dei processi deposizionali. La prima metà del deposito si è formata dalla deposizione continua e graduale da flussi continui. L'eruzione inizia con un iniziale deposizione da flussi particolati turbolenti che depongono in maniera graduale. Questi flussi diventano laminari con l'aumentare del run-out, diversi con la deposizione di traction carpets multipli deposti in massa in maniera step-wise. La seconda parte dell'eruzione è caratterizzata da flussi non continui, probabilmente legati alla formazione di una caldera. I depositi si formano per una rapida deposizione da flussi laminari. I processi di saldatura della porzione sommitale della MUI sono successivi alla messa in posto e sono guidati principalmente dal carico litostatico.

ABSTRACT

The rheomorphic, high-grade, welded ignimbrites are a special type of pyroclastic density current (PDC) deposits usually associated with high intensity volcanic explosive activity (VEI >4). They are characterized by a high variability of physical features and sedimentological structures that may testify different emplacement mechanisms from a PDC and a different response to topography during and after the end of the depositional processes. When the temperatures of the deposits are higher than the glass transition temperature (Tg) and the deposits stay hot for long periods, they can undergo important local readjustments.

The purpose of this PhD thesis is to investigate the processes which control the deposition and deformation of rhyolitic to comenditic welded ignimbrites, how and when the different processes occurred and which factors influenced the formation of the main structures.

The Sulcis Volcanic District (SW of Sardinia - Italy) is a good field laboratory where sixteen, well exposed, well conserved and not affected by recent tectonic processes, welded ignimbrites crop out. All these features permit to study and analyze the main processes, despite their Miocene age.

The research focalized its attention on three ignimbritic units: Punta Senoglio Unit, Ventrischio Unit and Monte Ulmus Unit. In particular, attention was pointed on the Monte Ulmus Ignimbrite (MUI), where all these processes are particularly well recorded along the numerous available outcrops .

A systematic and detailed study of the deposits was carried out. The description at different scales of the main features of the deposits and the analysis of the products with different methodologies, permitted to recognize the main eruptive phases and the main processes driving the formation of the ignimbrite, together with their relative timing. The deposits of all the three studied ignimbrites show evidences of syn- and post-emplacement welding and rheomorphism. The analysis of the micro-structural features

on thin sections clear evidences an upward variations in strain rate, suggesting deposition varying from gradual to step-wise aggradation.

The MUI well preserves primary structures typical of high grade ignimbrites (foliations, lineations, welding and facies variations), structures typical of rheomorphic ignimbrites (rotated solid fragments, different scale folds, ramps, etc) and structures related with cooling and degassing processes (blisters, degassing pipes, devitrification facies).

The MUI is a high-grade, rhyolitic to trachytic, locally rheomorphic, low-aspect-ratio welded ignimbrite. It crops out mainly in Sant'Antioco and San Pietro islands and in the Sulcis, on an area of 300 km^2 with a minimum estimated volume of 2.5 km^3. The most likely position of the source area is in the northern sector, few kilometers N of the San Pietro Island. Four main pyroclastic flow units (in the sense of Smith 1960) that cooled together, named A0, A1, A2 and B and preceded by a basal fall-out deposit (F), have been distinguished. In addition, seven main lithofacies were recognized inside the MUI, reflecting the different flow regimes of PDC (from turbulent to laminar) and the different depositional processes (from gradual to step-wise aggradation). All the described lithofacies are suggestive of welding and deformation processes are syn- and post emplacement. MUI physical features are strongly related to the paleotopographic conditions (topographic highs, topographic lows or flat conditions). Locally, the deposits record quick syn-emplacement en-masse readjustment, also on gently dipping slopes (~10°), probably due to generally low viscosity of the products or to the large amount of gas entrapped inside the deposits. The low values of Tg estimated for the MUI products (~415 °C) possibly resulted in protracted, nearly plastic conditions of the deposits, enhancing the remobilization of the deposits also during the final phases of emplacement.

The first, turbulent, steady flows were characterized by high depositional rates and the related deposits were emplaced by gradual aggradation. The flows became progressively laminar with the increase of the run-out, and different traction carpets were emplaced en-masse by step-wise aggradation. The second half of eruption was characterized by an unsteady mass flow, possibly related with a caldera-forming phases. The deposits grew up by quick gradual aggradation from laminar flows. Welding processes of the upper portion of MUI are mainly post-emplacement and they were driven principally by lithostatic load.

ACKNOWLEDGEMENTS

PREFACE

This thesis is the result of a three years, mainly field-related research, also made in collaboration of the Department of Mineralogy of the University of Geneve. Basing on a detailed study of the deposits of three ignimbrite units of the Sulcis Volcanic District (Sardinia, Italy), the main objectives are : I) to discuss the main processes controlling the formation of low-aspect ratio welded ignimbrites, II) to study the role of preexisting topography on these processes and III) to define the relative timing of the main depositional and deformational processes which control the formation of the main structures observed in welded, low-aspect ratio ignimbrites.

The thesis is divided into 7 chapters. Chapter 1 is a review of the state of art about the main processes affecting low aspect ratio ignimbrites and the main factors influencing these processes. Chapter 2 is focused on the geological setting of the Sulcis Volcanic District, with a short description of the geodynamic framework of the West Mediterranean area during the period comprised between 30 to 16 Ma ago and of the general volcanic stratigraphy of the district. Chapter 3 attempts to describe the stratigraphy and the main features of two main comenditic units emplaced in the Sulcis area. Starting from Chapter 4, the attention is focused on the Monte Ulmus Ignimbrite. In Chapter 4 the main structures recognized on the field in the ignimbrite deposit are described, discerning structures related with primary rheomorphism from structures related with secondary rheomorphic processes. Chapter 5 represents the core of this thesis. In this chapter the general stratigraphy, the main lithofacies, the features of the main stratigraphic sections and the lateral variation of lithofacies are presented and discussed. Field evidences are also used to infer the possible vent area. Chapter 6 presents all the physical and compositional data used to characterize the Monte Ulmus product. Finally, in Chapter 7 the main goals of this thesis are summarized with a brief discussion on the stratigraphy, the emplacement processes, the welding processes, the secondary rheomorphism and the final degassing phases.

TABLE OF CONTENTS

CHAPTER 5 : STRATIGRAPHY AND LITHOFACIES OF MONTE ULMUS IGNIMBRITE 59

CHAPTER 6 : PHYSICAL AND COMPOSITIONAL PROPERTIES OF THE MONTE ULMUS IGNIMBRITE   103

CHAPTER 7 : DISCUSSION   121

CHAPTER 1

INTRODUCTION

Volcanic explosive activity of high intensity is characterized by a large range of eruptive processes, which disperse magma fragments both through plumes which enter in the atmosphere, and through pyroclastic density currents (PDC). PDC are mixture of particles and gas, gravity driven, moving across topography. They can be generated by different processes (Fig. 1.1): total o partial collapse of eruptive columns, disruption of lava domes, lateral blasts (Mt. Saint Helens, 1980 - Hoblitt, 1986) or gravitational collapse of a lava fronts (i.e. Merapi - Bardintzeff, 1984; Montserrat - Cole et al., 1998).
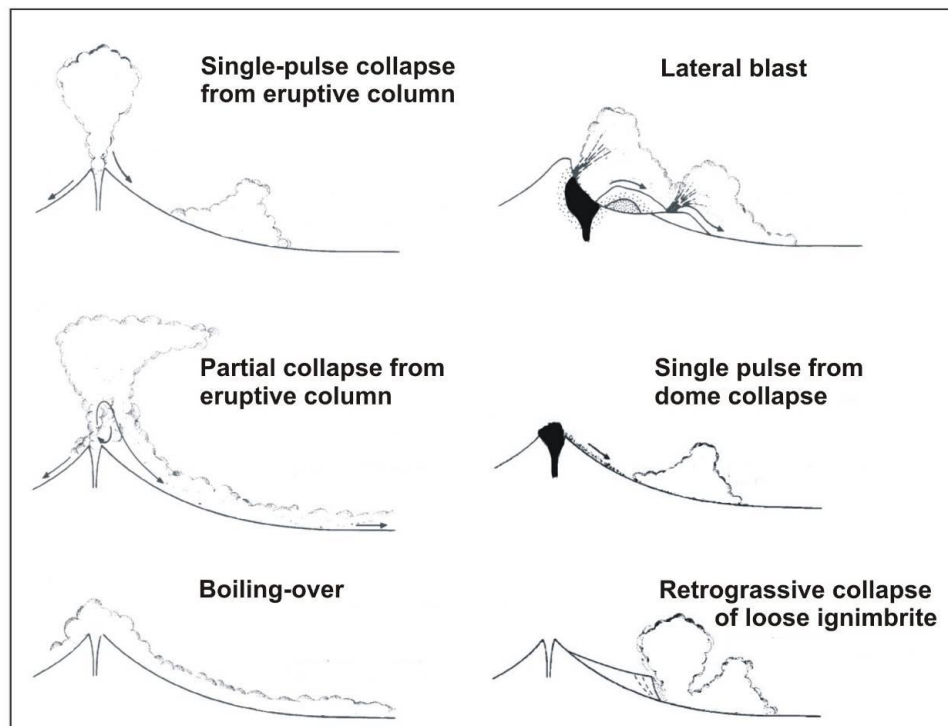
Fig.1.1: Different origin of pyroclastic density currents (mod. Branney and Kokelaar, 2002)

Ignimbrites are a special type of PDC deposits, represented by welded or unwelded, pumice-bearing, ash-rich, matrix supported deposits (Sparks 1973, Walker, 1983). The present thesis deals with sedimentological and depositional features of this type of deposits, mainly focusing on welded ignimbrites.

Welded ignimbrites are present in a large spectrum of geological settings, from continental arcs (Bad Step Tuff - Branney and Kokelaar, 1992), to intra-continental (Snake River Plan, Idaho - Bonnichsen and Citron, 1982), to intraoceanic volcanoes (Mogàn Formation, Gran Canaria; Schmincke, 1974). Ignimbrites have high variability in bulk volume (from <1 to >1000 km^3 DRE – Freundt, 1999), travelled distance from the source (from 1 to >100 km), aspect ratio and response to topography (channel confined to radially symmetrical), sedimentary structures (massive to stratified), welding degree (up to to lava-like), clast type and size (accidental clasts to pumice dominated, ash- to block-rich), deformation structures, and chemical composition (mafic through felsic, often compositionally zoned) (Carey, 1991; Druitt, 1998; Freundt and Bursik, 1998; Freundt et al., 1999). The emplacement temperatures are greater than the temperature of glass transition (T_g), usually estimated around 650°C for rhyolitic products (Giordano et al., 2005). The ignimbrite features are influenced by different factors as the initial magmatic temperature (at the source), transport path through the atmosphere, adiabatic decompression and heat loss during transport (Cas and Wright, 1987).

Two main emplacement models for the high temperature ignimbrites were formulated during the years (Fig. 1.2). In the first one, formulated by Sparks (1976) and later supported by Wright and Walker (1981), Fisher (1986), Carey (1991) and Druitt (1998), the ignimbrite is emplaced by a high concentration, non-turbulent particulate flow stopping and deflating en-masse like a debris flow (Jonhson, 1970). The pyroclastic flow body moves like a laminar or plug flow (Sparks, 1976), and the poor sorting of the ignimbrite is a consequence of the high particle concentration of the poorly expanded flow. In addition, the steep-sided pumiceous levees and distal frontal lobes are suggestive of a pyroclastic flow with high yield strength (Wilson and Head, 1981). In the second model, formulated by Branney and Kokelaar (1992), the ignimbrite deposits are emplaced gradually through the continuous deposition of pyroclastic particles during the passage of a highly expanded PDC. The main pieces of evidence for the progressive

aggradation derive from a series of dynamic processes recorded inside the deposits as: I) gradual changes upward in the flow direction, related to the continuous re-arrangement of the topographic conditions following aggradational deposition; II) presence of shearing fabrics inside the whole sheet; III) presence of vertical compositional zoning; IV) lateral changes in lithofacies.

In describing and discussing the ignimbrite deposits object of these thesis, we will continuously use some terms that it is opportune to briefly discuss and define in the following.
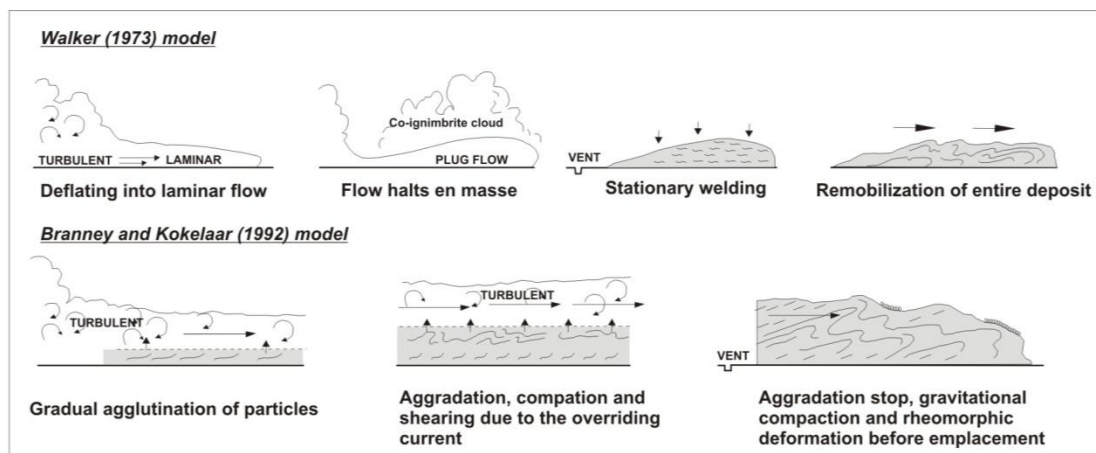
Fig. 1.2: *The two main emplacement models for high temperature ignimbrites*

1.1 Welding

1.1.1 Welding process

Welding is the process which promotes agglutination or cohesion of glassy fragments (ash and pumice lapilli) (Smith 1960a; Sparks et al., 1999, Branney and Kokelaar, 1992). This process occurs by the sintering of ash particles, the compaction and the following flattening of pyroclasts occurring at temperatures above the glass transition (T_g).

In agreement with Branney and Kokelaar (1992), the term agglutination is referred to the immediate particle sintering, and is recorded by still visible particle outlines. Agglutination does not refer to any emplacement mode, and it depends on pyroclasts viscosity, the duration of the contact and the applied force (Branney and Kokelaar, 2002). Inside the deposit, if particle are still in the fluid state, they rapidly transform to a

homogenous liquid (non- particulate flow - NPF) and the particles become "coalescent" (particle outlines are totally obliterated).

The welding process is favored by different factors: pyroclasts rheology (Giordano et al., 2005; Dingwell and Hess, 1998), deposition rate, high emplacement temperature (Freundt, 1998), melt composition and eruption style (Andrews and Branney, 2010; Smith, 1960).

The pyroclasts rheology is the main parameter which influences the rate and intensity of welding (Andrews, 2006). In the case of pyroclastic products, two main parameters controll the final rheology: I) the rheology of the silicate melt before the eruption, and II) the change in rheology during the different phases of the eruption (transport, deposition, cooling and degassing phases). Rheology of pyroclasts is also influenced by other factors: temperature (at the vent and during emplacement), melt composition, volatile (concentration and composition), crystal content, vesicularity.

1.1.1.1 Temperature

The influence on welding of temperature must be analyzed at two different stages: during the earlier phases of eruption (magmatic temperature) and during the latest phases of eruption (emplacement temperature).

Eruptive temperatures of rhyolitic magmas can vary in a large range, between 660° (Bindeman and Valley, 2003) and 1150°C (Chapeco volcanic field – Kirstein et al., 2001). Lower values, observed in partly crystallized lavas, possibly correspond to the limiting conditions under which magmas can flow. Magmas do not crystallize instantaneously, but over temperature range. Few magmas, however, have a wide enough range of crystallization to remain mobile at temperatures far below those at which they begin to crystallize. Eruptive temperatures in rhyolitic magmas with AI index 0.9 - 1.05 and volatiles content ranging from 0.5 to 4.5 % have eruptive temperatures comprise between 850 - 980 °C (Andrews - 2006).

The emplacement temperature of a rhyolitic magma is usually considered as equal or lower than the magmatic temperature, and depends on the cooling rate during transport (Thomas and Sparks, 1992). In rhyolitic ignimbrites, the main parameters affecting the emplacement temperature are: eruption temperature, gas content, mass flux, flow dynamics, the amount of air engulfed in the flow during transport, the amount of lithic

clasts and the run-out of the pyroclastic flow (Pioli, 2002). Recently some authors, using thermal demagnetization of magnetic mineral-rich lithic clasts embedded in the ignimbrite, have estimated the minimum emplacement temperatures. These temperatures range from 180 to 380 °C in 79 AD of Vesuvius - Cioni et al., 2004) and from 260 to 360 °C (472 AD of Vesuvius - Zanella et al., 2008) in non-welded ignimbrites. The emplacement temperatures can range from 200 to >580 °C (1630 BC eruption of Santorini - McClelland and Druitt, 1989), from 150 to >580 °C (1.8 ka eruption of Taupo - McClelland et al., 2004) and ~620°C (2Ma eruption of Cerro Galàn - Lesti et al., 2011) in no-welded to densely welded ignimbrites. In rhyolitic melts, the estimated temperature loss during transport varies from 100 °C to 150°C (Riehle et al., 1995; Sheridan and Wang, 2005). A key concept linked with temperatures, is the concept of glass transition (T_g). The glass transition is a kinetic boundary between viscous and mechanical response to an applied stress (Giordano et al., 2005). In ignimbritic deposits, in the temperature range above T_g, particles can deform and produce welding; below the glass transition, particles behaves elastically and will not weld. T_g is strongly related to melt composition, volatile composition and cooling rate, and it is represented by a time-temperature curve.

1.1.1.2 Viscosity

Viscosity is the internal resistance of a fluid to flow. It represents the ratio between the shear stress applied to a layer of thickness Z and permanently deformed in a direction x parallel to the stress, and the strain rate. A general formula for viscosity is expressed by:

$$\sigma = \sigma_o + \eta \, (\delta m/\delta t)^n$$

where σ is the total shear stress applied parallel to the direction of deformation; σ_o is the yield strength of the fluid or the stress required to initiate flow; η is the viscosity, expressed in Pa x s); $\delta m/\delta t$ is the gradient of velocity dx/dt or strain rate over a distance Z normal to the direction of shear; and n is an exponent with a value of 1.0 or less depending on the form of the velocity gradient.

Various factors control magmatic liquid viscosity (Fig. 1.3): temperature, melt composition, type and concentration of dissolved volatile, crystal content and vesicularity (Dingwell, 1998). While the dependence of the viscosity of a rhyolitic melt on composition and volatile content are well known (Dingwell et Hess, 1998; Giordano et al., 2005; Stevenson et al., 1998), the effects of crystal content on viscosity are more complex, and these can be very important when discussing welding properties of an ignimbrite deposit.

1.1.1.3 Crystal content

As a general rule, the effect of suspended crystals is to increase the effective viscosity of the magma.At a first approximation, the effective viscosity can by estimated from the Einstein-Roscoe equation:

$$\eta = \eta_o (1 - RC)^{-2.5}$$

where η is the effective viscosity of a magmatic liquid, C is the volume fraction of suspended solids; η_o is the viscosity of the magmatic liquid alone; and, R is a constant with a best-estimated value of 1.67. Viscosity shows a strong increase when crystal content is around 40%, due to a interaction between inter-crystals (Stevenson et al. 1996), while when crystal content is around 70% the melt behaves like a solid. Costa (2005) has proposed a more general relation linking η and C, valid also at high solid concentrations.
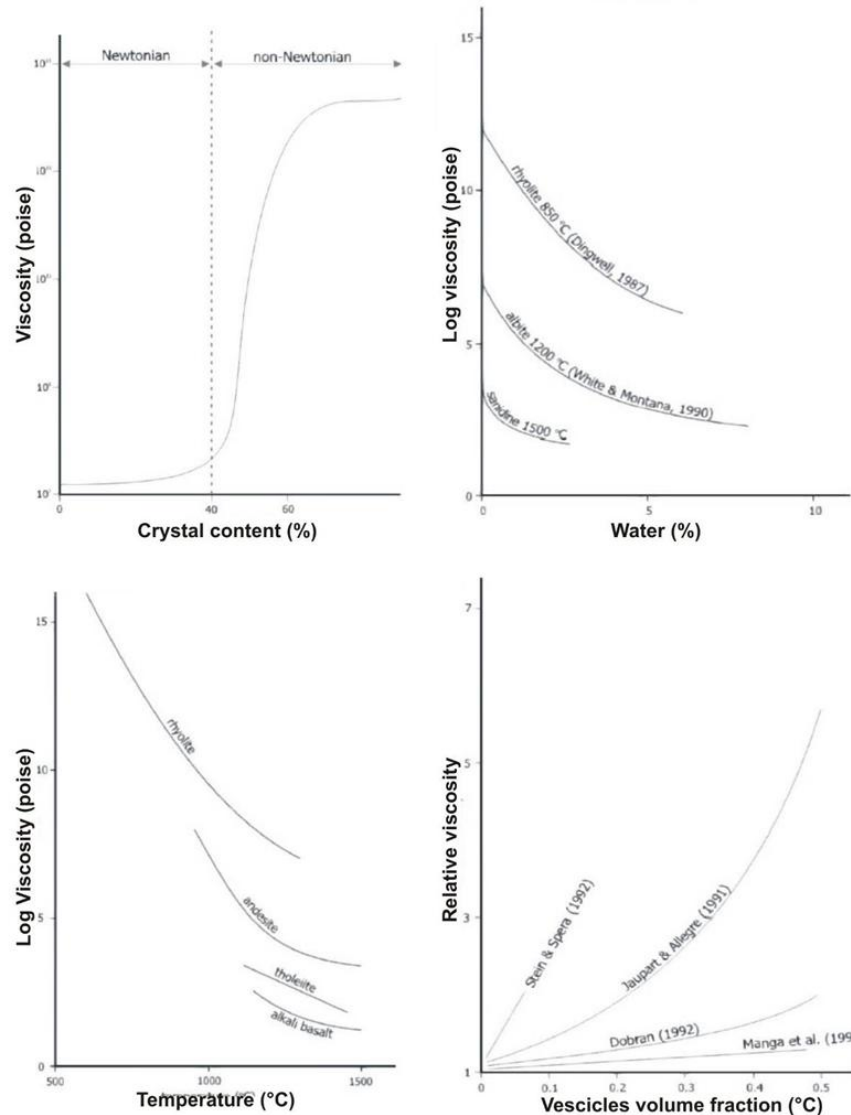
Fig. 1.3: *Main factors influencing viscosity of melts (modif. from Andrews-2006)*

1.1.2 Welding mechanism

The welding process may occur by pre-agglutination of glassy fragments during low fountaining activity (spatter cone building or clastogenic spatter fed lava flows), aggregation of particles into the pyroclastic flows (Chapin and Lowell, 1979) or during the post-emplacement phases (Ross and Smith, 1961; Wolff and Wright, 1981; Kobberger and Schmincke, 1999) characterized by cooling, gas expulsion and compaction of the deposit. As a consequence, the welding process can occur gradually during the entire depositional phase (Branney and Kokelaar, 1992) or after the

deposition of the whole deposit (Sparks, 1976; Druitt, 1998), and can be considered occurring as a "continuum" (Branney and Kokelaar, 1992). Freundt (1999) proposed the existence of two end-members for the welding processes: *Load welding* (where the welding degree mainly depends on the final thickness of the deposit, in accord with Riehle et al., 1995) and *aggregation welding* (in which welding starts before emplacement). The load welding model is applied principally to moderately welded ignimbrites, and it is well recorded in the observed variation of the vertical welding profile, characterized by higher welding values around the lower third of the ignimbrite), by the development of an eutaxitic structure characterized by the flattening of the fiammae (Aspect Ratio AR; Smith, 1960; Riehle et al., 1995), and by the porosity profile (Ross and Smith, 1961).

The load welding model does not justify completely the evidences shown by some high or extremely high grade ignimbrites (P1 ignimbrite – Freundt and Schmincke, 1995; Brown's View Member – Andrews et al., 2008). These deposits show densely welded facies associated to thickness lower than 10m.

In the "aggregation welding model", hot pyroclastic particles can rapidly aggregate and agglutinate within the PDC (Freundt 1998) because they are characterized by low viscosity and they can weld instantaneously also in the absence of a load strain (Branney and Kokelaar, 1992; Freundt, 1998; Capaccioni and Cuccoli, 2005; Andrews 2006). When agglutination starts, two main processes occur: aggregation rapidly increases the mean particle diameter into the particulate flow, favoring the formation of a non particulate underflow. This non-particulate depositional system is the responsible for the formation of mass flow structures, the progressive coalescence of liquid particles and finally the complete obliteration of primary vitroclastic structures (lava-like facies – Pioli, 2002). This process can be quantified by the particle aggregation rate representing the number of aggregation events for unit volume and time, a proxy for the probability of occurrence of stable coalescence.

1.1.3 Welding intensity

The welding intensity may range from a first stage of *incipient welding*, marked by the onset of cohesion between particles, passing to a state of *intermediate (moderate) welding* to finish in a densely (*completely*) welded state, characterized by the complete

cohesion between the particle surface, the elimination of pore space and, possibly, the homogenization of glass (Smith, 1960). In more recent years, different ranks of welding have been defined. Quane and Russell (2005) divided the welding degree into six classes (I to VI) on the basis of the physical proprieties of the ignimbrite (density, porosity, pumice oblateness, particle orientation, point load and uniassial compressive strength). Streck and Grunder (1995), recognized five main welding facies: no-welded, incipiently welded, partially welded with pumice, partially welded with fiammae, and densely welded. They divided the different welding degrees on the base of density, deformation of clasts (pumice vs. fiammae), adhesion of clasts, and color and luster. Mundula et al. (2009) presented a scheme subdividing the welding degree into three main classes on the basis of the aspect ratio of the fiammae, the strenght of the glass shards alignment and the style of crystallization of the matrix.

1.2 Ignimbrite classification

One of the criteria used to classify ignimbrite deposits was introduced by Walker (1983), and is the aspect ratio. The Aspect ratio of an ignimbrite is defined as the ratio of the average thickness to the diameter of a circle with an area equal to the deposit. It commonly ranges between 10^{-5} and 10^{-2} (low aspect-ratio and high-aspect-ratio ignimbrites, respectively) and it can be used as a proxy for the energy of the current. A high aspect ratio ignimbrite (HARI) testifies to the deposition of a highly concentrated PDC, strongly topographically controlled and with a short run-out. Conversely, a low-aspect ratio ignimbrite (LARI) results from the passage of a highly energetic, low concentration PDC, not strongly influenced by the presence of topographic irregularities or barriers.

On the base of the presence or not of welded facies, Walker (1983) distinguishes two main kinds of ignimbrite: low-grade and high-grade ignimbrites.

Low-grade ignimbrites are pyroclastic deposits which are totally unwelded even they are more 50 m thick. On the contrary, "high-grade ignimbrites" correspond to densely welded deposits ("*even where they are less than 5m thick*" – Walker, 1983), emplaced at temperature above their minimum welding temperature (around 650 °C for rhyolitic compositions; Grunder et al., 2005; Bindeman and Valley, 2003).

Following the Branney and Kokelaar classification (1992) (Fig. 1.4) we recognize five categories of ignimbrite gradually passing from extremely low-grade (no-welded) to extremely high-grade ignimbrites. These five main categories are established on the base of a "continuum" variation of physical properties (temperatures, viscosity, yield strenght), lithofacies (lineations, % in lithic fragments, flow folds) and eruptive and welding processes (column height, coalescence and agglutination).

1) Low- grade ignimbrites are totally (or with little evidence) no welded but may be weakly lithified by vapor-phase crystallization.

2) Intermediate-grade ignimbrites (or Non Rheomorphic welded ignimbrite) usually present a welded central part and non-welded facies in the upper and lower portions. This type of ignimbrite is usually pumice and fiammae-rich, and is usually related to load welding processes.

3) High-grade (or Rheomorphic) ignimbrites are completely and intensely welded from the base to the top, and present rheomorphic zones. They are characterized by the presence of fiammae, and welding results from a combination between load and aggregation welding.

4) Extremely high-grade (or Lava-like) ignimbrites mainly derive from aggregation welding, and are characterized by intensely welded, lava like facies andrheomorphic facies. Ash particles are completely coalescent and the vitroclastic texture is poorly visible (Andrews and Branney, 2010).

5) Fountain-fed lava flows represent the extreme degree of welding of a pyroclastic product, and are mainly related to Hawaiian lava fountain activity, where the very low viscosity of particles and their very high temperature are responsible of the liquid-like behavior of particles and of their complete coalescence.
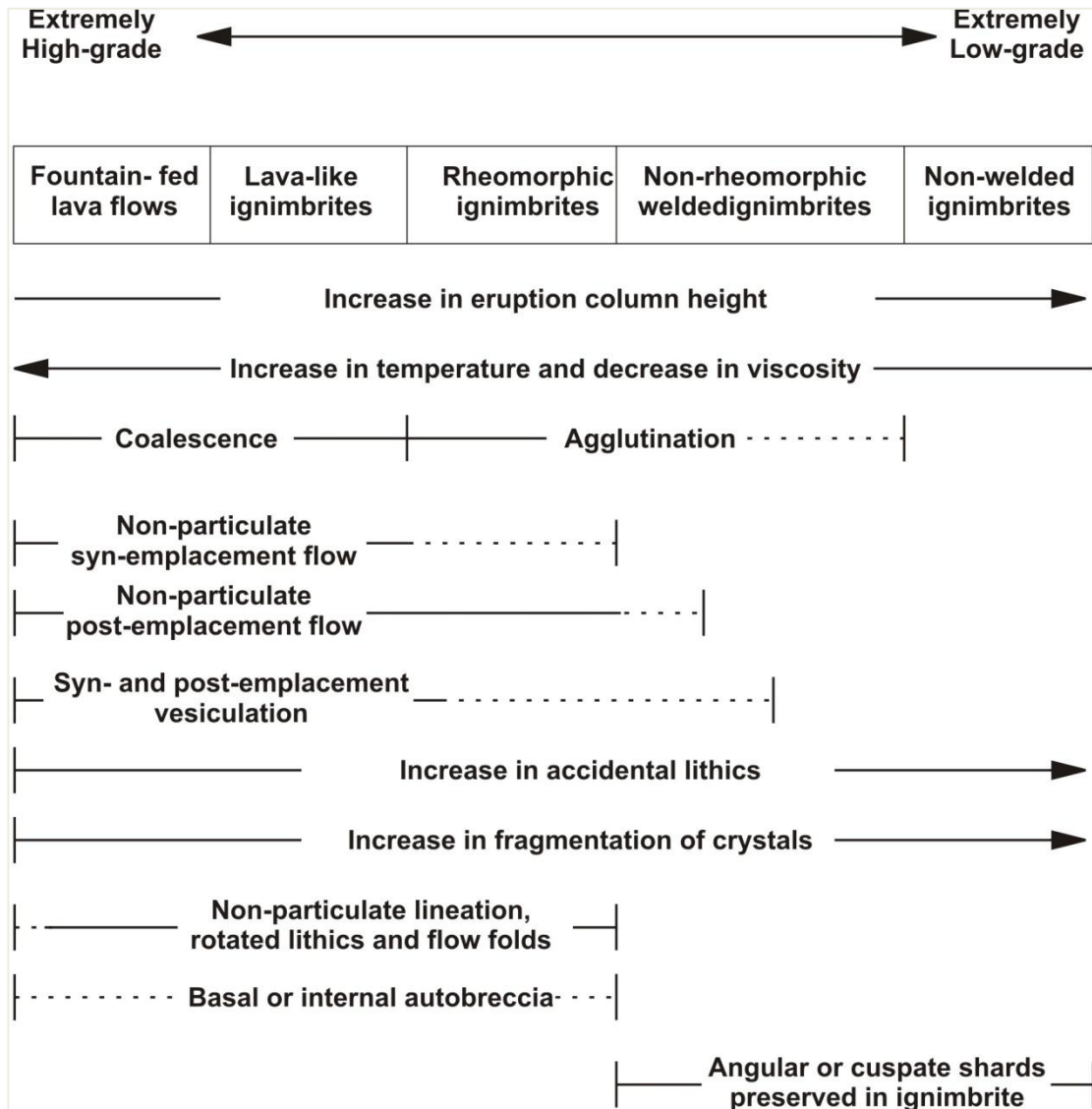
Fig. 1.4: Branney and Kokelaar (1992) diagram showing the five main categories, as defined on the base of a "continuum" variation of physical properties

1.3 Rheomorphism

Rheomorphism is the syn and post-emplacement, hot-state ductile flow of welded tuff (Branney and Kokelaar, 1992) that occurs at temperature above the glass transition (Tg; Giordano et al., 2005). It is one of the last stages which characterize the formation of welded tuffs, after magma chamber processes, eruption, transport, deposition and

welding (Andrew, 2006) and it commonly occurs in high grade ignimbrites (Sparks, 1973; Branney and Kokelaar, 1992; Wolff and Wright, 1981).

Two main rheomorphic phases exist (syn-depositional and post-emplacement rheomorphism), but both the timing of the process and the deformation style related to these phases are still not clear.

The rheomorphic process is influenced by three main mechanisms: 1) gravity (when ignimbrite is deposited on a slope); 2) lateral momentum associated to aggrading pyroclasts; 3) shearing (due to the coupling with the over-passing PDC).

In this work the term "syn-depositional (or primary) rheomorphism" is referred to all these deformations occurring during the passage and emplacement of the PDC. This rheomorphism is responsible of the formation of structures characterized by a simple shear component, without any evidence of pure shear (e.g. compaction). In contrast, post-emplacement (or secondary) rheomorphism is related to all the processes of remobilization of a still plastic deposit after the passage of PDC. This rheomorphism is characterized by large-scale structures with consequent deformation of the whole deposit thickness (or of a large part of it) and may deform pre-existing structures related to primary rheomorphism.

The kind of structures forming during the rheomorphic process depends on the predominance of pure shear vs. simple shear components. In pure shear flow, also defined as "coaxial flow", a pair of lines is continuously kept parallel to the instantaneous stretching axes, and the orientation of the principal strain axes does not change during deformation. Conversely, in simple shear flow the orientation of the principal strain axes continuously changes (rotates) during deformation, and this kind of deformation is also called rotational. The strain regime affecting the flow can be deduced from the geometry of the strain ellipsoid (Passchier and Trouw, 1996). Rheomorphic processes produce a characteristic association of deformational structures comprising: folds, pervasive sheet joints, prolate fiammae and vesicles, local boudinage, thrusts and local autobrecciation (Andrews and Branney, 2010; Pioli and Rosi, 2005; Chapin and Lowell, 1979).

1.3.1 Rheomorphic Structures

The rheomorphic processes produce different structures inside the deposits, which can be subdivided into 4 main groups (Andrew, 2006): planar fabrics, linear fabrics, kinematic indicators and folds.

Planar fabrics may be mechanically isotropic (responding passively to strain) or anisotropic (influencing the distribution, scale and style of structural of elements). With the term "planar fabrics" we group together any penetrative planar feature. Two main types of planar structures exist: initial planar structures (bedding) and "following" planar structures (primary and secondary – *in sensu* Passchier and Trouw – 2005). Primary planar structures (S_0) are those structures folded during the first deformational phase while the secondary planar structures are those structures produced by following deformational phases (S_n). Example of planar fabrics are: eutaxitic fabric (Wolff and Wright, 1981; Sumner and Branney, 2002), compositional banding (Kobberger and Schmincke, 1999), embricated fiammae, foliations and vesiculated parting surfaces (Pioli and Rosi, 2005).

Linear fabrics are typical of prolate and linear elements, and they group all the fabrics that can be described by referring to a line. They can be penetrative or superficial (Twiss and Moore, 1992). In ignimbrites, linear fabrics are fundamental to define the general transport direction during deformation, as they are generally oriented parallel to the maximum principal strain axis. Linear fabrics structures are: stretched vesicles (Pioli and Rosi, 2005), stretched fiammae and lineation in tuff matrix (Chapin and Lowell, 1979). Kinematic indicators group all those fabrics and structural elements that record the sense of shear. They can be divided into two main groups: rotational (rotated porphyroclast, asymmetric boudins) or no-rotational (shear bands) (Andrew, 2006). Rotating structures around crystals or lithic fragments, crystal orientation and shard texture are good shear sense indicators (Pioli, 2002). A rigid fragment into an homogeneous, viscous, non-coaxial flow can follow two different paths. In the first one, the symmetry axes of the fragment undergoes continuous rotation, while in the second one, after onset of rotation, the fragment reaches a stable position in the plane of flow (Gosh and Ramberg, 1976). Different structures (Fig. 1.5) are associated to these two different styles. Continuously rotanting objects will form δ-type structures, while stable objects will develop σ-type structures with stair-stepping symmetry.
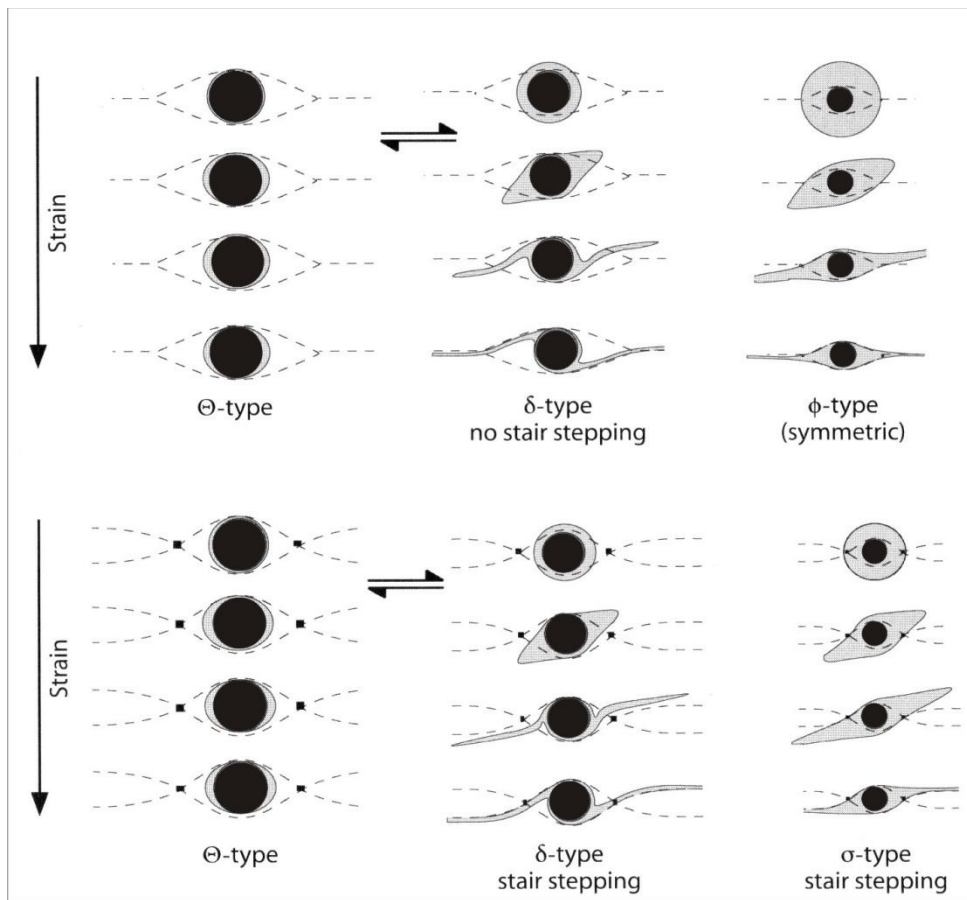
Fig. 1.5: *Main structures related with increasing strain rate (Passchier and Trouw, 2005)*

The ropy flow structures described by Pioli and Rosi (2005 - Fig. 1.6) are also good shear sense indicators: these elongated vesicles have the main axes parallel to the shear direction. The name derives from the fact that the cavities which characterize these structures show arcuate folds hinge lines, similar to rapes. The convexity of the crests in the lower and upper surfaces are opposite, with the convexity in the lower portion opposite respect the flow direction
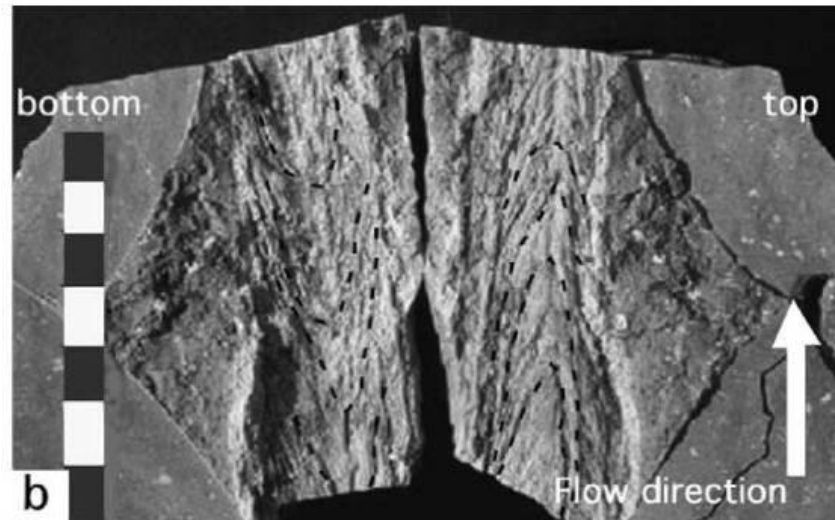
Fig. 1.6: *Ropy structures in Nuraxi Ignimbrite (Pioli and Rosi, 2005)*

Folds develop when planar fabrics undergo ductile shortening, and they may vary from micrometric to decametric. Fold types are influenced by physical conditions and mechanical proprieties of the ignimbrite during folding (Andrews, 2006). Sheath-folds (Fig. 1.7) are common in rheomorphic ignimbrites and are interpreted to have formed by progressive non coaxial shear of a cylindrical fold (Branney et al., 2004).
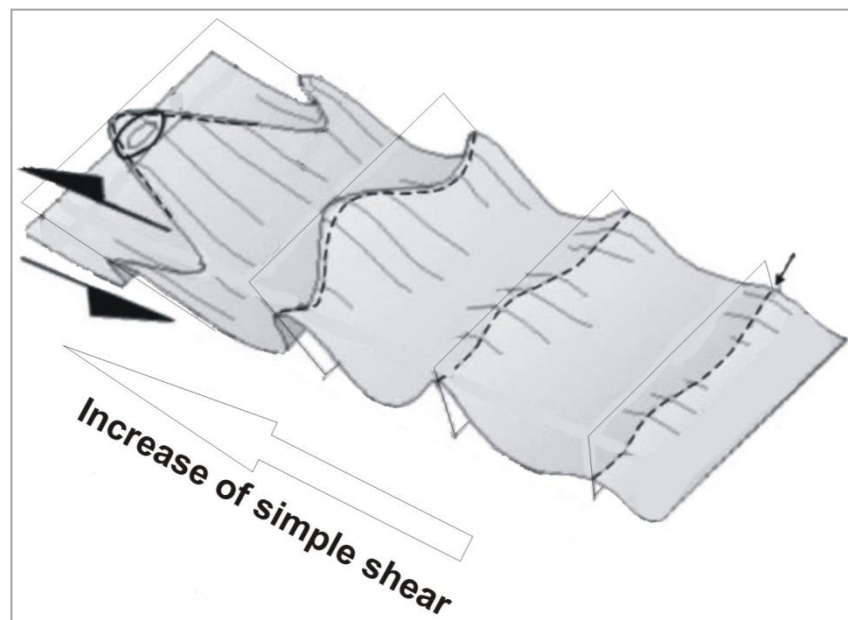
Fig. 1.7: *Sheath fold (modif. from Andrews and Branney, 2010)*

CHAPTER 2
GEOLOGICAL SETTING

Tertiary volcanism of Sardinia is related to the complex geodynamic evolution of the West Mediterranean area, mainly developed following the Alpine orogenic cycle.

2.1 Geodynamic framework of western Mediterranean area

The Alpine Orogenic cycle started during Langhian, due to the collision and the initial eastward subduction of the European continental margin beneath the northern margin of the African plate (Gattacceca, 2001; Rosenbaum et al., 2002; Lacombe et Jolivet, 2005; Lustrino et al., 2009) followed by a W-NW subduction of the African lithosphere beneath the European continental margin (Carmignani et al 1994; Lecca et al., 1997) (Fig. 2.1).
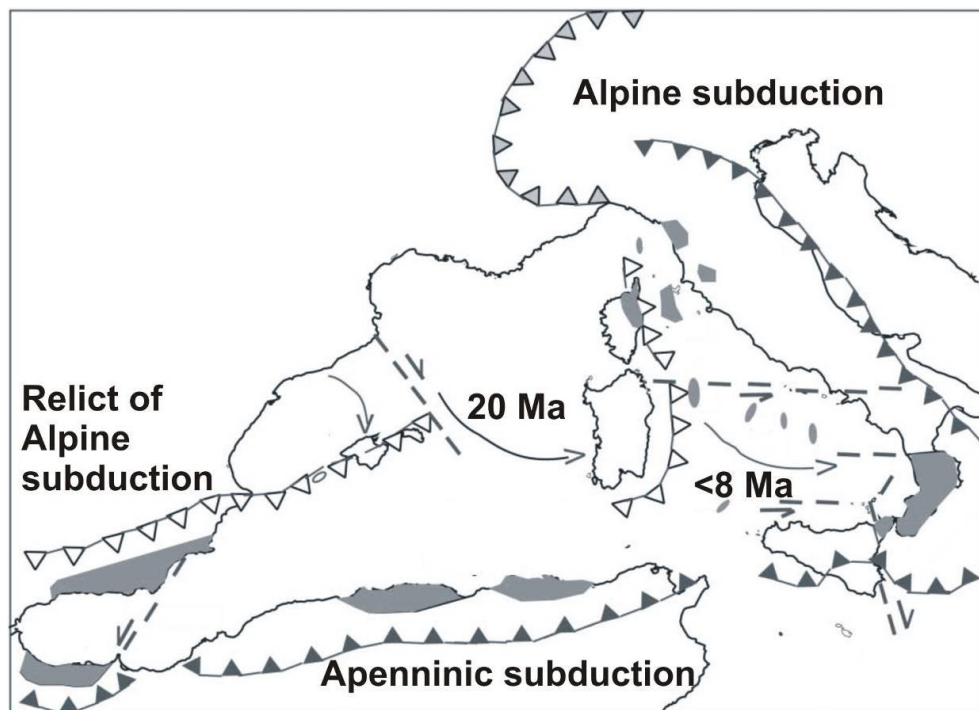
Fig. 2.1: *Sketch of Mediterrean area after Sardinia-Corse block rotation (modif. from Savelli- 2002)*

After the Alpine orogenic cycle (ended around 30 Ma – Savelli, 2002) the western Mediterranean area was interested by intensive magmatic activity linked with rifting phases (Lecca et al., 1997) and the subsequent opening of Alboran, Algerian, Sardo-Balearic, Liguro-Provencal and Tyrrenian basins and the supra-subduction growth of the Apennines-Maghrebides thrust belt (Savelli, 2002).

Carmignani et al. (1995) considered the opening of the western Mediterranean basins as a post-collisional effects due to the gravity collapse of the northern Appennine orogenic wedge.

Different igneous rock associations were emplaced in the western Mediterrean area in different tectonic settings: i) convergence of collisional type, ii) convergence of non-collisional, roll-back type, iii) backarc, iv) passive margin and v) foreland.

The Oligocene-Miocene volcanic activity of Sardinia is an example of orogenic magmatism in which magmatic activity is related to subduction induced by the opening of Mediterranean sea and the rotation of the Sardinia-Corse microplate from the Iberian margin, which started 30 Ma ago and ended 16 Ma ago (Lecca et al., 1997; Savelli et al., 2002; Speranza et al., 2002).

2.1.1 Main magmatic Phases of the Mediterranean area

In the post-orogenic phase, Savelli (2002) comprises six main magmatic phases in the Mediterrean area with the following temporal intervals: 30-15 Ma (phase I), 15-9 Ma (phase II), 8-6 Ma (phase III), 5-2 Ma (phase IV), 2-1.5 Ma (phase V) and 1.5-0 (phase VI). The volcanic activity that interested the south-western sector of Sardinia occurred during the first two phases (Fig. 2.2).

Phase I: Opening and extension of Liguro-Provencal back-arc basin (Speranza et al., 2002) and counter-clockwise rotation of the Sardinia-Corsica block (approximately 25-30°) took place 19 Ma (Mountigny et al.,1981; Savelli, 2002). The main effects related to this process are testified by the formation of a N-S oriented rift system in the western sector of Sardinia (Montigny et al., 1981). During this phase basalts, basaltic andesites, high-K andesites and ignimbritic rhyolites where emplaced in the graben (Savelli, 1979; Bellon, 1981). At 20 Ma in Sardinia, the volcanic activity became predominantly

explosive, with the emplacement, in the south-western sector, of mainly rhyolitic ignimbrites (Savelli, 2002).

Phase II: The end of the first phase coincided with a widespread activity bordering the Algerian and Alboran basins (Bellon, 1981). Montigny et al. (1981) proposed that the passage between these two first phases was marked, around 19 Ma ago, by the end of the Sardinia-Corsica block rotation.

The orogenic volcanic activity in the Sardinia-Corsica block persisted until ca. 13 Ma. During this phase large volumes of ignimbrites, andesitic and rhyolitic flows, dacite domes, comendites and shoshonites were emplaced.

Lecca et al. (1997) related these two different volcanic phases with the evolution of the rifting:

- Pre-rift phase (upper Eocene - Oligocene): characterized by a transpressive regime during collisional phases into the western Mediterrean sector.

- 1° rift phase (Aquitanian - Burdigalian): passage from strike-slip to transtensive to extensional regime; some late-Hercynian faults were reactivated starting the proto-rift phases. In this phase the volcanic activity showed an increase of explosivity with the emplacing of the pre-Aquitanian andesite sequence (28 -24 Ma).

- 2° rift phase (Upper Burdigalian - Langhian): the collapse of the main tectonic structures was linked with the eastward migration of the Appennine frontal thrusts and the following drift of the Sardinia- Corsica microplate. The volcanic products changed drastically their chemical characters with emplacement of primitive basalts (eg. 18 Ma Monte Arcuentu dykes – Assorgia et al., 1984) and peralkaline rhyolites in the Sulcis area (15 Ma – Beccaluva et al., 1987; Lecca et al., 1997).
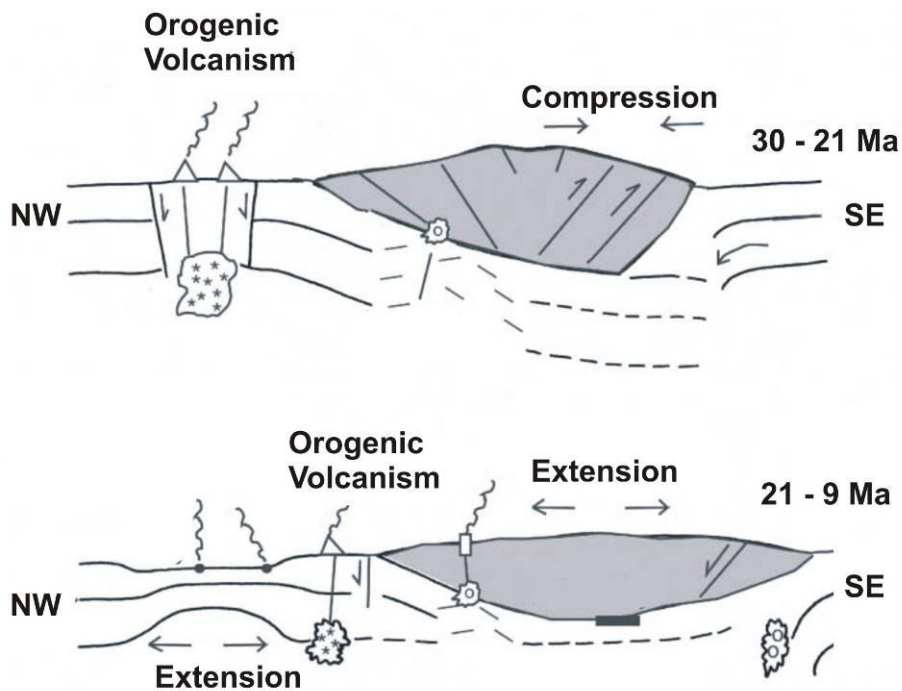
Fig. 2.2: Sketch of volcanic activity in the area comprise between Provencal and Corsica-Sardinia Margin (NW) and Adria (SE) between 30 and 9 Ma (modified from Savelli, 2002)

2.2 The Sulcis Volcanic District

The Sulcis Volcanic District, south-western Sardinia (Italy), represents the southern portion of a magmatic arc extending on the west side of the Sardinian Rift, and active between $38,28 \pm 0,26$ (Lustrino et al., 2009) and 13.8 Ma (Beccaluva et al., 1987; Lecca et al., 1997). It is the result of subduction of oceanic lithosphere under the European plate (NNW according to Savelli et al., 2002; NO-NNO oriented according to Carmignani et al., 1994). Deposits from this activity crop out extensively along the main branches of Sardinia rift system and in the Sulcis area.

The Oligocene-Miocene volcanic activity in Sulcis Volcanic district was principally sub-aerial and it reached its volumetric climax around 20 Ma ago (Carminati et al., 2012) (Fig. 2.3), before the end of Sardinia-Corse block rotation (Gattacceca et al., 2007).
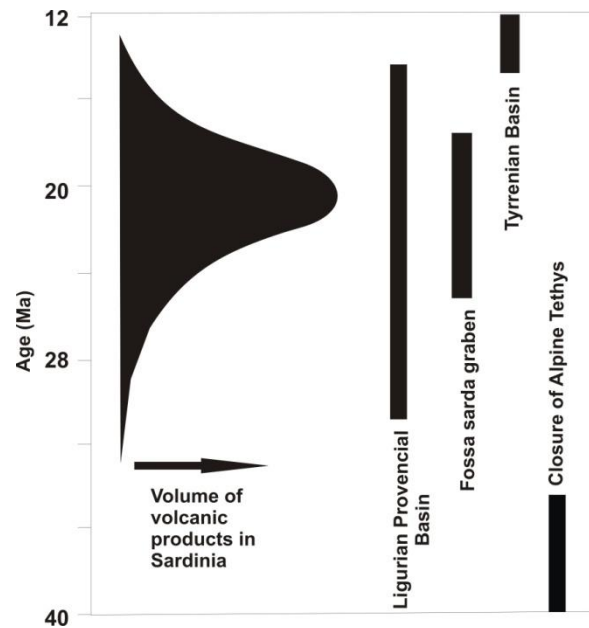
Fig. 2.3: *Main Mediterranean events coeval with Sardinian volcanic activity (modif. from Carminati et al,. 2012)*

Its products are subdivided into two main sequences: Lower Sequence and Upper Sequence (Morra et al., 1994; Assorgia et al., 1990). The end of the microplate rotation coincides approximatly with the passage between the Phase I and Phase II of the Oligocene - Miocene activity (Savelli et al., 1979 and 2002), and to the passage between the Lower and Upper sequences in the Sulcis area.

The Lower Sequence (28.4 to 17.7 Ma) is mainly represented by calc-alkaline andesitic to basaltic lava flows, domes and minor pyroclastic products emplaced in the southern sector of the basement. Morra et al. (1994) estimated the total thickness of this volcanic succession around 500 meters. Vents are mainly located in the area of Sant'Antioco Island and in the Sulcis mainland. Their products are characterized by glomero-porphyritic textures and contain phenocrysts (~30%) of Plagioclase, Orthopiroxene and Clinopiroxene in a rhyolitic glass (Assorgia et al., 1992).

The Upper Sequence (17.6 to 13.8 Ma) was characterized by a very intense explosive activity that emplaced 12 main and at least 4 minor ignimbritic units, interbedded with several comenditic lava flows and 2 volcanoclastic deposits (Mundula et al., 2009). All the ignimbritic units are divided/separated by paleosoils (Pasci, 2001). The ash-flow tuff units are generally high-grade ignimbrites which mainly crop out in the area of San Pietro Island and Sant'Antioco Island. These products are calc-alkaline to peralkaline,

dacitic to rhyolitic in composition. The mineral assemblage generally consists of plagioclase + augite + hyperstene + biotite + fayalite in dacitic magmas and plagioclase + sanidine + hyperstene + augite + biotite + horneblende in rhyolitic magmas (Pioli, 2002). Peralkaline comendites are mainly represented by highly porphyritic, sanidine and quartz-bearing, products, with only rare Na-amphibole. The silica and alkali content increases with decreasing age. Average agpaitic index ranges from 0.65 to 0.86 for sub-alkaline rock and from 0.98 to 1.15 for peralkaline rocks.

2.2.1 The Upper Sequence

The general stratigraphy of all these units was recently revised during the geological survey for the new 1:50,000 geological map of Italy (Sheet 564 - Carbonia and Sheet 563 - Isola di San Pietro), and it schematically shown in the table of Fig. 2.4.

	Geniò	Low-grade ignimbrite	Rhyolite
	Colonne	Volcaniclastic deposits	Rhyolite
	Punta Mingosa	High-grade ignimbrite	Rhyolite
15.5±0.2 My	Serra di Paringianu	High-grade ignimbrite	Rhyolite
	Paringianu	Low-grade ignimbrite	Rhyolite
	Monte Tortoriso	Lava flows	Comendite
	Monte Ulmus	High-grade ignimbrite	Rhyolite
15.5±0.5My	Ventrischio	High-grade ignimbrite	Comendite
	Punta Senoglio	High-grade ignimbrite	Comendite
	Genarbì	Volcaniclastic deposits	Comendite
	BeccoNasca	Lava flows	Comendite
	Cala Vinagra	Lava flows	Comendite
	Matzaccara	High-grade ignimbrite	Dacite
	Punta dei Cannoni	High-grade ignimbrite	Rhyolite
	Montagna di Capo Rosso	High-grade ignimbrite	Rhyolite
15.8±0.2 My	Nuraxi	High-grade ignimbrite	Rhyolite
	Monte Crobu	High-grade ignimbrite	Rhyolite
	Seruci	High-grade ignimbrite	Rhyolite
16.6±0.8 My	Acqua sa Canna	Low-grade ignimbrite	Dacite
	Lenzu	High-grade ignimbrite	Rhyolite
	Corona Maria	High-grade ignimbrite	Dacite

Fig. 2.4: *Stratigraphic sequence of the Sulcis volcanic successions (mod. Mundula et al. 2009)*

The Upper Sequence deposits (Fig. 2.4), mainly crop out in the San Pietro and Sant'Antioco Islands and in the Sulcis-Iglesiente area. The first pyroclastic units emplaced (from Corona Maria Unit to Matzaccara Unit) have a composition variable from dacite to rhyolite. At 15.5 Ma (Morra et al., 1994) peralkaline products started to be erupted in the San Pietro Island. This "comenditic phase" started with a first lava flow followed by two ignimbrite units (the Lower, "Punta Senoglio" Unit, and the Upper "Ventrischio" Unit). Two comenditic lava flows (Nasca and Borrona) were successively emplaced on top of the Ventrischio Unit in the north-western sector of San Pietro Island. Interbedded within this extended peralkaline effusive activity, another mildly peralkaline, rhyolitic ignimbrite was erupted (the Monte Ulmus Ignimbrite), followed by the last comenditic lava flow (Monte Tortoriso unit). The Upper Sequence ends with other 4 rhyolitic ignimbritic units (Paringianu Unit, Serra di Paringianu Unit, Punta Mingosa Unit and Geniò Unit) and one epiclastitic unit (Colonne Unit).

2.2.2 Main stratigraphic units of the Upper Sequence

2.2.2.1 Corona Maria Unit

This unit (18.6 ± 0.4 Ma; *Assorgia et al., 1992, Morra et al., 1994*) crops out in the area comprised between the northern sector of Portoscuso area and Carbonia. It is a single cooling unit, few to 40 m thicks, formed by a basal fall-out deposit overlain by a crystal-rich, dacitic to rhyolitic, densely welded ignimbrite. The ignimbrite has eutaxitic texture with dm-sized scoriaceus fragments and two different types of lithic fragments (Ronga, 2010). Typical petrographic association is Pl+Aug+Fay+Hyp+Fe-ox (Pioli, 2002).

2.2.2.2 Lenzu Unit

The Lenzu Unit (Rb/Sr 16.5±0.9 Ma – Morra et al., 1994) crops out only in the northern sector of Portoscuso. It is formed by a single cooling unit, 2 to 30 m thick, constituted by a basal pumice fall-out followed by a dacitic to rhyolitic, porphiritic, incipiently to densely welded ignimbrite. The large thickness variations observed in the ignimbrite are mainly related to a strongly irregular substrate (Pioli, 2002). Lithic fragments

percentage is generally lower than 10%. Typical petrographic association is Pl+Kfs+Opx+Cpx±Ol (Assorgia et al., 1992).

2.2.2.3 Acqua Sa Canna Unit

The Acqua sa Canna Unit (K/Ar 16.6±0.8 Ma – Morra et al., 1994) is exposed near Portoscuso and Carbonia villages. It is a compound cooling unit, 10 to 35 m thick, composed by three fall-out deposits interbedded with two low-grade, dacitic, massive pyroclastic flow units deposits. Sandstone and siltstone layers, 2 to 17 m thick, and epiclastic deposits separate this unit from the underlying Lenzu unit. Locally, between the fall-out deposits and the dacitic low-grade massive ignimbrites, dm-scale surge deposits are interbedded (Pioli, 2002).

Typical petrographic association is Pl + Bt + Aug + Hyp ± Mag (Assorgia et al., 1992).

2.2.2.4 Seruci Unit

The Seruci unit crops out in the area comprised between the Carbonia village and the northern sector of Sulcis area. It is a compound cooling unit, 9 to 40 m thick, made by the deposits of several flow units. The different medium-grade, dacitic to rhyolitic units are divided by sharp contacts. The crystal content (5 to 10% vol) is compounds by Pl+Sd+Hy+Aug±Ol (Assorgia et al., 1992).

2.2.2.5 Monte Crobu Unit

The best outcrops of the Monte Crobu Unit are located in the eastern sector of Sulcis, near the Narcao and Carbonia villages. It is a compound cooling unit, 15 to 100 m thick, composed by two reddish, massive to roughly stratified, eutaxitic, high-grade ignimbrites and by one grey, matrix-supported, no-welded breccia deposits. The ignimbrite has a high crystal content and variable lithic fragments. Petrographically, the two ignimbrites are characterized by the same paragenetic association: Sd ± Pl ± Fa ± Mag (Assorgia et al., 1992).

2.2.2.6 Nuraxi Unit

The Nuraxi unit (15.79±0.16 Ma - Pasci et al., 2001; Pioli, 2003) represents the basal ignimbrite in the volcanic stratigraphic sequence of San Pietro Island (Assorgia et al.,

1992) and it crops out in the Sant'Antioco Island and in the Sulcis area. It is a single cooling unit, 10 to 158 m thick, composed by two rhyolitic, low-aspect ratio ignimbrites, named by Pioli and Rosi (2005) "Lower Ignimbrite" and "Upper Ignimbrite". The Lower Ignimbrite, 2 m thick, is a no-welded to incipiently welded deposit with glassy matrix, passing upward gradually to a devitrified lapilli tuff. The contact with the Upper Ignimbrite is planar to slightly ondulatory, with a contact from gradational to sharp. The Upper Ignimbrite is the most voluminous portion of the Nuraxi Unit. It is a brownish to dark grey, crystal rich (Pl + Sd + Anort + Opx + Cpx + Bt; Morra et al.,1994), densely welded to lava-like ignimbrite. The ignimbrite reaches a maximum run-out of 80 km.

2.2.2.7 *Matzaccara Unit*

The Matzaccara Unit crops out in the entire Sulcis district. It is a rhyolitic, highly porphyritic, no-welded to moderately welded ignimbrite. The field appearance is highly variable (from a reddish, massive tuff, a light-gray tuff to a whitish ash deposits) but the presence of biotite crystals with a typical metallic luster and the stratigraphic relations with the other ignimbrites permit to easily recognize this unit. Typical mineral association is composed by Pl + Bt ± Sd (Morra et al.,1994).

2.2.2.8 *"Comenditic phase" units*

The products of this phase crop out mainly in San Pietro Island (explosive and effusive products) and in Sant'Antioco Island (only the explosive products). Petrographycal association of the ignimbrites is: Sd + Qtz + Cpx ± Amph ± Bt. The two ignimbritic units are summarily described in the following and will be discussed in detail in Chapter 3.

2.2.2.8.1 *Punta Senoglio Unit (Lower Comendite Ignimbrite)*

The Punta Senoglio Unit (K-Ar, a 15,5 ± 0,5 Ma - Morra et al., 1994) extensively crops out in the northern sector of San Pietro Island and in the western sector of Sant'Antioco Island. In the San Pietro Island, this unit was emplaced on top of a pile of comenditic lava flows, while in the Sant'Antioco Island the emplacement of the ignimbrite was mainly controlled by a preexisting valley cut inside ancient epiclastic deposits. It is a 6

to 30 m thick, comenditic, no-rheomorphic, low-aspect ratio, highly porphyritic (until 38% vol.) ignimbrite.

2.2.2.8.2 Ventrischio Unit (Upper Comendite Ignimbrite)

The Ventrischio Unit, crops out on the San Pietro Island, where it shows a strong topographic control, being mainly channelized by the preexisting comenditic lava flows (Borrona and Nasca Units), and along the western sector of Sant'Antioco Island. It sparsely crops out also in the Sulcis mainland. It is a single cooling unit, 2 to 57 meters thick, comenditic, low-aspect ratio, moderately to densely welded ignimbrite.

2.2.2.9 Monte Ulmus Ignimbrite Unit

The Monte Ulmus Ignimbrite Unit (MUI) (15.5 ± 0.5 Ma; Morra et alii 1994) widely crops out on San Pietro and Sant'Antioco Islands, and locally in the Sulcis mainland. It generally overlays a comenditic ignimbrite (Ventrischio Unit), while in the northern sector of the San Pietro Island, it directly rests on some comenditic lava flows and coulees (Nasca and Vinagra units, Fig. 2.4). The MUI is overlain by the final products of the Sardinia Miocene activity, represented by the Paringianu and Serra di Paringianu ignimbritic units, and locally by a comenditic lava flow (Monte Tortoriso Unit, San Pietro Island, Fig. 2.4). It is a single cooling unit, 7 to 98m thick, rhyolitic, locally rheomorphic, high-grade ignimbrite composed by a basal fall out deposits followed by 4 flow units.

Monte Ulmus Ignimbrite Unit is the focus of this thesis and it will be describe and discussed in large detail in the following chapters.

2.2.2.10 Paringianu Unit

The Paringianu Unit crops out mainly in the San Pietro Island and Sulcis area. It is a 10 meters thick, low-grade, rhyolitic tuff. On the San Pietro e Sant'Antioco islands, the base of the unit is composed by six fall-out and surge deposits. Generally it is a no-welded ignimbrite, but in the northern sector of the San Pietro Island and near the Paringianu village it is incipiently welded with m-spaced columnar joints and degassing pipe structures. Typical paragenesis is: Sd+Pl±Bt (Morra et al.,1994)

2.2.2.11 Serra di Paringianu Unit

The Serra di Paringianu Unit widely crops out on San Pietro and Sant'Antioco islands, while scattered outcrops are present in the Sulcis mainland. This unit represents the youngest major ignimbrite of the SW Sardinia volcanic succession. It is a single cooling unit subdivided into 4 different eruptive rhyolitic sub-units, reddish to brownish, high grade ignimbrite. The typical paragenesis is: Sd + Pl ± Opx ± Cpx (Morra et al.,1994)

2.2.2.12 Punta Mingosa Unit

This unit crops out in the south-western sector of San Pietro Island. It is a, 15 meter thick, reddish, massive to faintly foliated, no-welded to incipiently welded, fine-ash ignimbrite. The phenocryst assemblage is constituted by mm-sized Pl + Sd, with subordinate amounts of Cpx + Mag.

2.2.2.13 Colonne Unit

This unit crops out only in the southern sector of San Pietro Island. It is a 10 meters thick, greyish to brownish, lithified ignimbrite, with flattened pumices set in a steeply argillified matrix, suggesting an originally partial welding degree. Lithic fragments are angular to sub-rounded, with maximum size of 6 cm. Free crystals (<5%) are mainly represented by mm-sized Sd.

2.2.2.14 Punta Geniò Unit

This unit records the last explosive event of the Sulcis Volcanic district. It crops out only in the southern sector of San Pietro Island and is composed by two different light grey, massive, fine ash matrix, no welded to moderately welded ignimbrites, separated by a cross bedded layer. The phenocryst assemblage is constituted by mm-sized Pl + Sd.

CHAPTER 3

COMENDITIC IGNIMBRITES

During the "comenditic phase", 4 peralkaline lava flow units (Basal lava flows, Nasca, Borrona and Tortoriso) and two comenditic ignimbrites (Punta Senoglio and Ventrischio Unit) were emplaced. The general occurrence of lava coulees testifies small-scale eruptive episodes intercalated with larger, more voluminous and intense eruptions recorded by the ignimbrites. Each lava flow has an areal extension smaller than 1 km^2 and maximum thickness up to 60-70 meters (Assorgia et al., 1992; Cioni et al., 2001). A stratigraphic study was performed on the two comenditic ignimbrites, in order to compare data from these crystal-rich ignimbrite, with the texture and sedimentological features of the Monte Ulmus Ignimbrite, the main object of this study.

3.1 Paleotopographic variations before and during emplacement of comenditic units

Before the "Comenditic phase", the paleo-topography of the area was generally flat. The well dispersed and large volume Nuraxi ignimbrite, in fact, formed a plateau filling of the main pre-existing topographic irregularities.

The two comenditic ignimbrite units (Punta Senoglio and Ventrischio Units) were emplaced into small paleovalleys mainly present between the first comenditic lava flows. On the northern sector of San Pietro Island, the Punta Senoglio Unit shows its maximum thickness (~40 meters) at Cala Senoglio, while at Punta Senoglio (<1 km E) it is 6 meters thick. On the NW sector of the San Pietro Island, the Ventrischio Unit is strongly channelized between the Nasca and Borrona lava flows, as testified by the

rapid E-W oriented thickness variations (from few meters to ~30 meters) and by the rapid lateral lithofacies transitions.

3.2 The Lower Comenditic Ignimbrite: The Punta Senoglio Unit

3.2.1 Stratigraphy

The Punta Senoglio unit crops out in San Pietro Island and San Antioco Island. On the basis of the vertical lithological variations and of the presence of sharp and erosive contacts, it is divided into 5 main sub-units: a basal lapilli deposit, covered by a first ignimbritic bed (L1), followed by a thin sequence of surge and fall deposits (L2) and finally by other two welded ignimbritic sub-unit (L3 and L4).

a) *Basal fall deposit*

The fall deposit, 0.2 to 1 meter thick, directly overlies a reddish paleosoil. It is constituted by deeply argillified pumice lapilli and by a high percentage of loose quartz crystals.

b) *Sub-unit L1*

Sub-unit L1, 1.5 m thick, crops out in the San Pietro and San Antioco islands. It is a blackish, crystal poor, moderately to densely welded fine ash tuff. Fiammae and sanidine crystals (<5 vol.%) are mm-sized. Lithic fragments (mainly fragments of older ignimbrites) are less than 5 vol.%.

c) *Sub-unit L2*

Sub-unit L2, 20 to 90 cm thick, is a blackish to whitish compound subunit composed by blackish partially welded deposits interbedded with non-welded cross-stratified beds. Two fallout beds,1 to 5 cm thick, with cm-sized pumice lapilli are present at the base of this subunit.

d) *Sub-Unit L3*

Sub-unit L3 (maximum thickness 20 meters on San Pietro Island) is a greenish, fine-grained, moderately welded ignimbrite. At the base a lithic-rich, normally graded layer

with sub-rounded fragments up to 20 cm in diameter is present. Blackish and reddish, Sd-bearing, highly porphyritic (25 vol.%) eutaxitic fiammae are up to 90 cm in size. The free crystals (Qtz + Sd) percentage is about 11 vol.% in the outcrops of the San Pietro Island, increasing until 32 vol.% in the Sant'Antioco Island.

e) *Sub-unit L4*

Sub-unit L*4* (3 to 10 meters thick) is a brownish, partially to moderately welded, coarse ash-bearing ignimbrite. Eutaxitic fiammae have an AR between 2:1 and 4:1, average size of 4 cm and maximum size of 50 cm. The very high crystal content (~38%) is mainly represented by euedral Qtz and Sd crystals with maximum size of 4 mm. Lithic fragments are whitish, angular to sub-rounded lava fragments, with maximum size of 3 mm. In the Sant'Antioco Island this sub-unit is a moderately welded, coarse-ash ignimbrite. Eutaxitic blackish vitreous fiammae (maximum size 30 cm) have upward variation in AR from 30:1 (in the inner core) to 3:1 in the topmost portion of the ignimbrite.
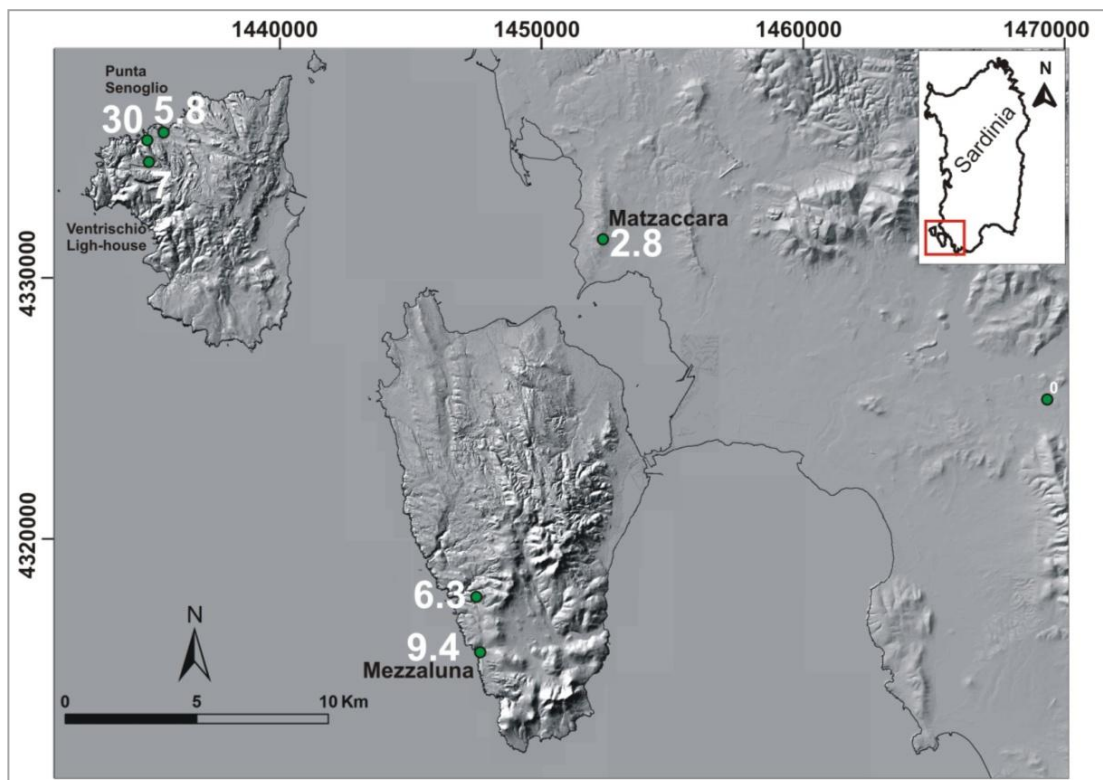
Fig. 3.1: *Total thickness of the main outcrops of the Punta Senoglio Unit (in meters)*
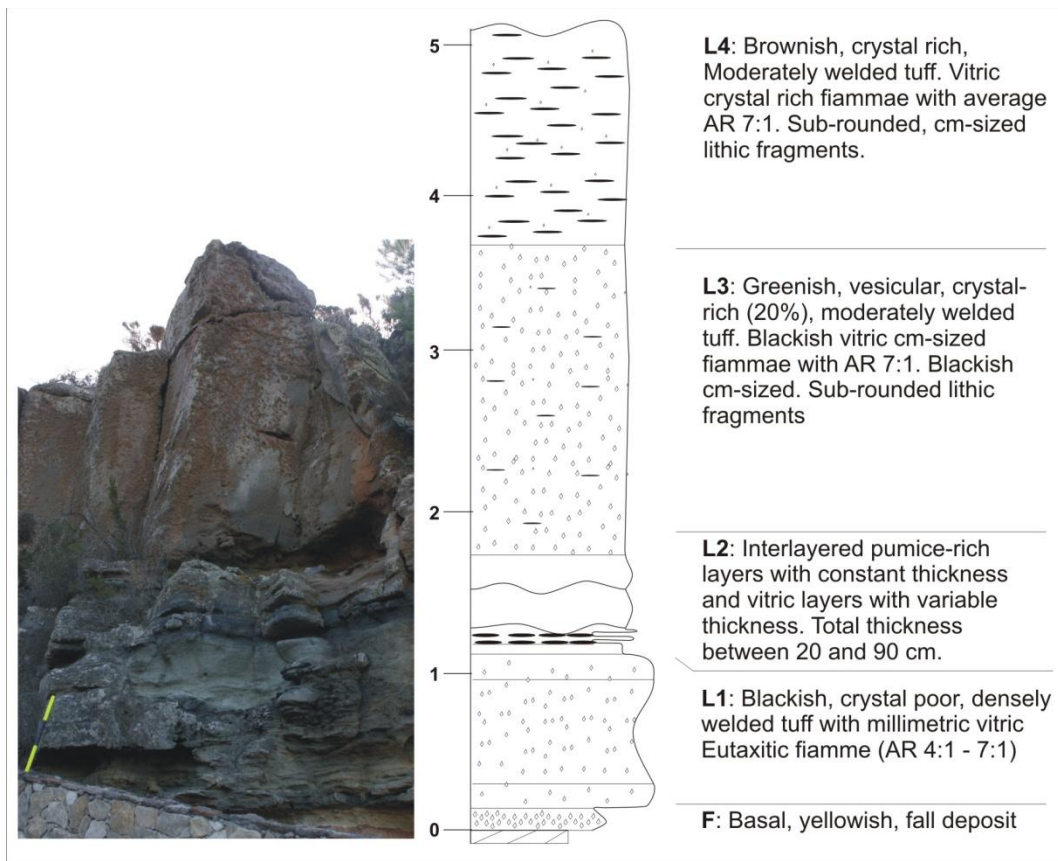
Fig. 3.2: *Complete stratigraphic section of the Punta Senoglio Unit, at Cala Senoglio (San Pietro Island)*

3.3 The Upper Comenditic Ignimbrite: The Ventrischio Unit

3.3.1 Stratigraphy

The Ventrischio Unit, 60 to 3 m-thick (Fig. 3.3), crops out locally in the San Pietro and Sant' Antioco islands and in the Matzaccara area. The unit is subdivided into 4 main sub-units on the presence of sharp and erosive contacts and strong changes in the sedimentological features. A basal fall-out deposit is covered by three ignimbritic sub-units (here named U1, U2 e U3) (Fig. 3.4).

 a) Basal Fall deposit (F)

The basal fall deposit (maximum thickness 20 cm) crops out until the Giba town (25 km from the San Pietro Island). It is a well sorted deposit of whitish pumice lapilli and cm-

sized lithic fragments, with an inverse-direct grading. It is rich in mm-sized Qtz crystals bearing well-preserved melt inclusions.

b) *Sub-unit U1*

Sub-unit U1 reaches its maximum thickness in the NW sector of the San Pietro Island, where it is 35 meters thick. It is a brownish, fine-ash matrix, moderately to densely welded ignimbrite, made up by 7 main beds. The different beds are characterized by a coarse tail reverse grading of fiammae in the upper portion. The ignimbrite is a vitric tuff with up to 20% vol. of loose crystals (mainly quartz and sanidine and only minor aegerine and arfvedsonite). Reddish to blackish, crystal-rich fiammae reach a maximum size of 1 m at the top of each single beds, while are generally only cm-sized (1-2 cm) inside the beds. Angular, cm-sized lithics fragments of lava and older ignimbrites are also present (around 5 % vol.).

c) *Sub-unit U2*

Sub-unit U2, 20 meters thick, reaches the maximum thickness in the north-western sector of the San Pietro Island. It is a greenish, moderately to densely welded ignimbrite, constituted by 4 beds and divided by the underlying sub-unit by a sharp contact. Eutaxitic fiammae are similar to those of sub-unit U1, and have a maximum size of 67 cm and AR between 6:1 and 10:1. Free-crystals, mainly Quartz and Sanidine, are coarse (maximum size 5 mm) and very abundant (up to 40 vol .%).

On the western sector of the Sant'Antioco Island, sub-unit U2 is represented by a massive, greenish, fine-ash matrix, densely welded ignimbrite, with 25 vol.% of mm-sized quartz and sanidine free-crystals. Sub-angular, mm-sized, lithic fragments are less than 5%. by volume (Fig. 3.4).

In the Sulcis area the sub-unit U2 is 2.4 meters thick. It is a massive, greenish, fine-ash, moderately welded ignimbrite. Mm- sized fiamme, rare lithic fragments and mm-sized quartz and sanidine loose crystals (10 vol.%) are dispersed inside the deposits.

d) *Sub-unit U3*

The sub-unit U3 (maximum thickness 7 meters) is divided by sub-unit U2 by a sharp contact. The most complete outcrops are located at Punta Senoglio, near the Ventrischio

lighthouse (NW San Pietro Island) and along the cliffs of the Mezzaluna gulf (Sant' Antioco Island). It is a reddish to greenish, moderately welded ignimbrite with mm-sized phenocrysts of quartz and sanidine. Flattened mm- to cm-sized fiammae are dispersed inside the ignimbritic body. At Punta Senoglio, U3 is 2.5 meters thick and is represented by a brownish, fine ash matrix, moderately welded ignimbrite deposit. Eutaxitic, low-porphyritic fiammae reach a maximum size of 7 cm and AR of 5:1. On the Sant'Antioco Island, sub-unit U3 is closed by a 20 cm-thick vitric layer.
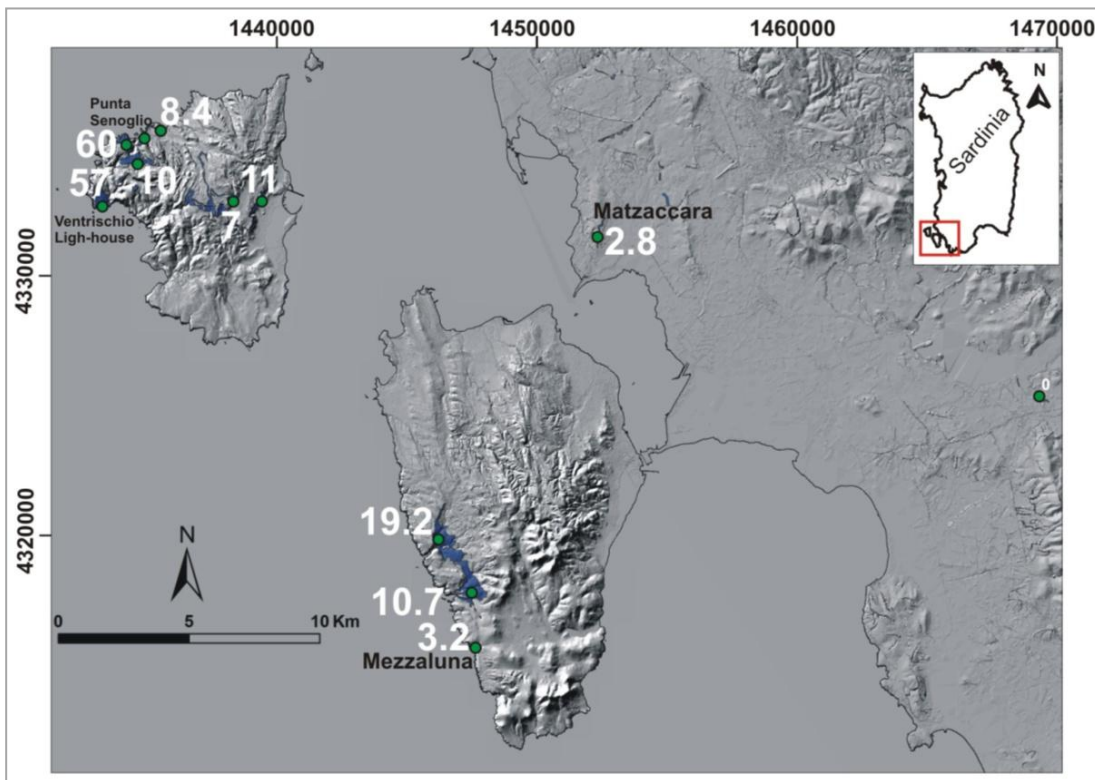
Fig. 3.3: *Total thickness of the main outcrops of the Ventrischio Unit (in meters)*
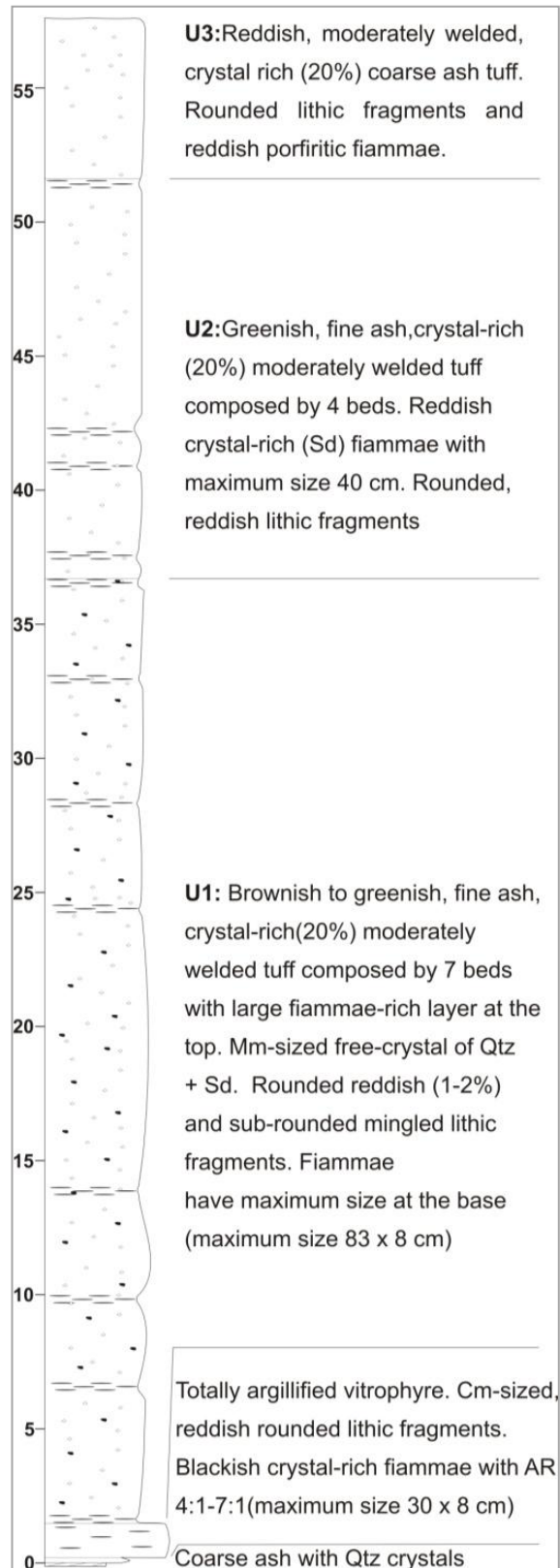
Fig. 3.4: *Stratigraphic section of the Ventrischio Unit at the Ventriscio Lighthouse (NW San Pietro Island)*

The sedimentological features of the deposit allowed to recognize and define main lithofacies, present in sub-unit U1 to U3.

I) Massive lapilli spatter, inversely grading tuff (MLS$_{(ig)}$) lithofacies*: 1 to 10 meters thick, this facies consists of brownish to greenish, graded, crystal-rich, vitric, partially to moderately welded deposits. It is presents both in sub-unit U1 and in sub-unit U2. Cm- to meter sized, brownish to reddish, platy vitric fiammae have eutaxitic structures and average AR of about 7:1 in the San Pietro island and 3:1 in the Sant'Antioco Island deposits. Fiammae are inversely graded (Fig. 3.5) and reach maximum size of 100 cm x 10 cm. Mm-sized crystal (~20 vol.%) of quartz and sanidine are present, loose in the matrix.

Interpretation

The inverse grading of the spatter blocks indicates the occurrence of kinetic sieving or high dispersive pressure in flow-boundary zones dominated by granular flow regime (Sulpizio et al., 2007). A granular flow regime is suggested also by the large amount in free-crystals present inside the deposits, suggesting a mechanism of fine ash-depletion.

Fig. 3.5: *Inverse grading of spatter blocks inside the MLS$_{(ig)}$ lithofacies*

II) Massive crystal-rich tuff (McrT) lithofacies: 1 to 7 meter thick, it is a brownish to greenish, massive, crystal-rich, vitric, partially to moderately welded deposits. It is presents both in sub-unit U1 and in sub-unit U2. Mm- to cm- sized vitric, crystal rich, fiammae have eutaxitic to slightly parataxitic textures and average AR 3:1. Angular to sub-rounded lithic fragments (5 vol.%) are dispersed into the deposit (Fig. 3.6).

Interpretation

The massive aspect of this lithofacies, the eutaxitic textures of fiammae and the relative position respect to the _MLS$_{(ig)}$_ can be interpreted as a spatter-depleted portion of the deposit.

Fig. 3.6: Lithic fragments dispersed in crystal-rich matrix of the McrT lithofacies

III) Eutaxitic well sorted tuff (EwsT) lithofacies: 1 to 3 m-thick, it is a brownish to greenish, spatter and crystal rich, moderately welded deposit. This lithofacies is presents only in sub-unit U1. Cm- to dm-sized, brownish to blackish, crystal rich, eutaxitic spatter fragments have average AR of 7:1 (Fig. 3.7). Cm-sized sub-rounded lithic fragments (3-4%) are present. This lithofacies is well developed on topographic reliefs in the north-western sector of the San Pietro Island.

Interpretation

This lithofacies is present only on the topographic highs of the San Pietro Island, in the basal portion of the deposit. As to the $MLS_{(ig)}$, the texture can be related to high energy currents able to overpass topographic reliefs, possibly depleted of the coarsest fragments, they could represent a sort of veneer deposits.

Fig. 3.7: *Eutaxitic spatter fragments in the EwsT lithofacies*

IV) Isotropic vitric tuff (IVT) lithofacies: 0.1 to 1 meter thick, it is a blackish vitric to silicized, crystal depleted, moderately welded deposit (Fig. 3.8). It is present at top of sub-unit U2 in the stratigraphic sections of the San Antioco Island. Mm-sized free-crystals of quartz and K-feldspar are dispersed in the matrix. No fiammae are recognizable inside the deposits. Micrometric no-deformed glass shards (X and Y-shape) are dispersed inside the deposits.

Interpretation

The absence of fiammae and structures related with shear stress and the massive aspect can be interpreted like a welded fall deposit possibly related with the emplacement of co-ignimbritic ash on still hot deposits.

Fig. 3.8: Blackish vitric to silicized matrix of the IVT lithofacies

3.3.3 Vertical and lateral facies variation

The Ventrischio unit, in the north-western sector of San Pietro Island shows important vertical and lateral lithofacies variations. Deposits appear strongly channelized inside the paleovalley, passing from 60 m (in the topographic low) to 10 meter (on the topographic high) (Fig. 3.9). The well exposed paleovalley allowed to study these lithofacies changes inside a small (~300 meters large), U-shaped, gently dipping slopes, valley (Fig. 3.10).

In the topographic low a multiple upward alternation of McrT and MLS$_{(ig)}$ lithofacies is well preserved, with a change in average grain-size of spatters and sharp contact up to the MLS$_{(ig)}$ lithofacies . The upper portion of the stratigraphic sequence is characterized only by the McrT. On the topographic highs, the basal 3 meters are composed only by the EwsT lithofacies, while upward an alternation of the McrT and MLS$_{(ig)}$ lithofacies is present. No-lateral changes in grain size of the spatter fragments were observed.

The IVT lithofacies is well preserved only in the Sant'Antioco island while is not exposed in the San Pietro Island, and it does not allow any evident lateral passage to other facies.

Interpretation

The multiple successions of McrT and MLS$_{(ig)}$ lithofacies with the sharp contact up to the MLS$_{(ig)}$ lithofacies are in accord with the Branney and Kokelaar (1992) step-wise aggradation model under an unsteady flow regime. The presence of the spatter-rich layer on the top of each bed, togheter with the high amount of free-crystals can be interpreted as due to a kinetic sieving process inside a each particulate flow that permitted to segregate upward and laterally the larger spatter fragments. The eutaxitic structures of these spatter fragments can be justified with the lithostatic load of the successive emplaced flows. The McrT lithofacies, on the top, can be interpreted as the results of a cloud depleted in large spatter fragments that testifies the last stage of emplacement probably due to a gradual aggradation. The IVT lithofacies is probably a distal lithofacies related with the proximal McrT lithofacies. It testifies the emplacement of an ash fall-out derived by the co-ignimbritic cloud.
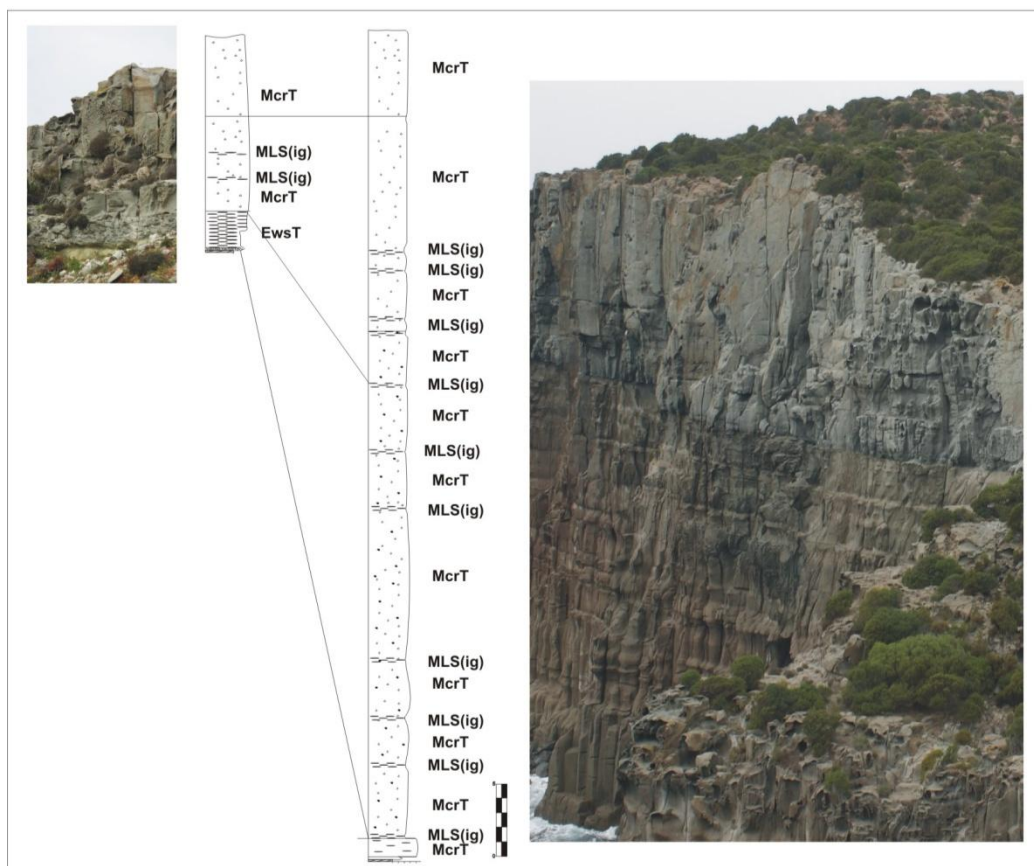
Fig. 3.9: *Lateral correlations of stratigraphic sections located on topographic high (left) and in topographic low (right) of the Ventrischio Unit.*
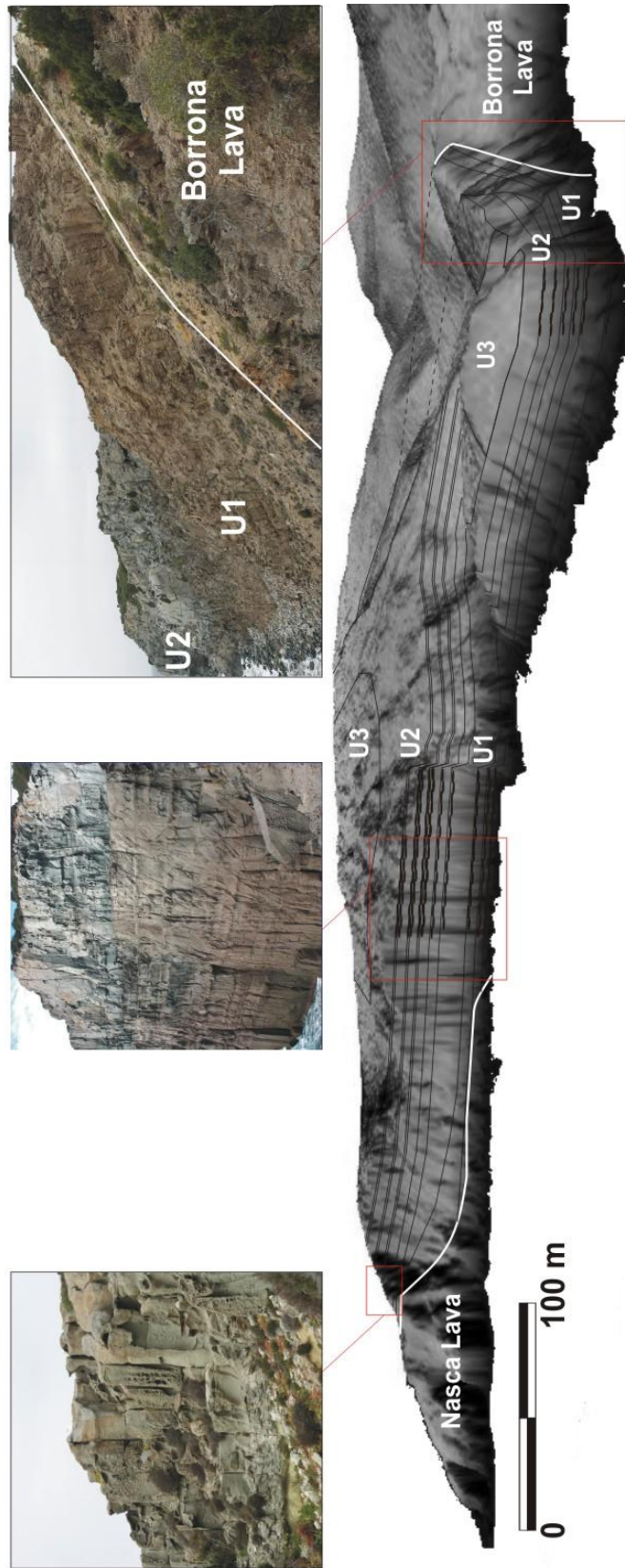
Fig. 3.10: Ventrischio Lighhouse cliff (NW San Pietro Island) with a topographic low in the central part and a topographic high on Nasca lava unit.

3.3.4 Flow direction

Flow directions were estimated and measured in the field with a magnetic compass mainly focusing on the direction of the major axis of parataxitic fiammae (Fig. 3.11). The high percentage of solid particles and their reciprocal interactions do not permit to record the flow sense, as in the case of MUI (see Chapter 4). Field data showed a SW-NE trend of major axis directions in the San Pietro Island, directions varying on average between N10° and N70°. In the Sant' Antioco area, the major axis direction is N80°. Finally, in the Sulcis area general trends of transport directions were N170°.

The only feature that permits to speculate an eastward flow versus is the lower percentage of lithic fragments is Matzaccara area, possibly related with a higher run-out of the pyroclastic flow.
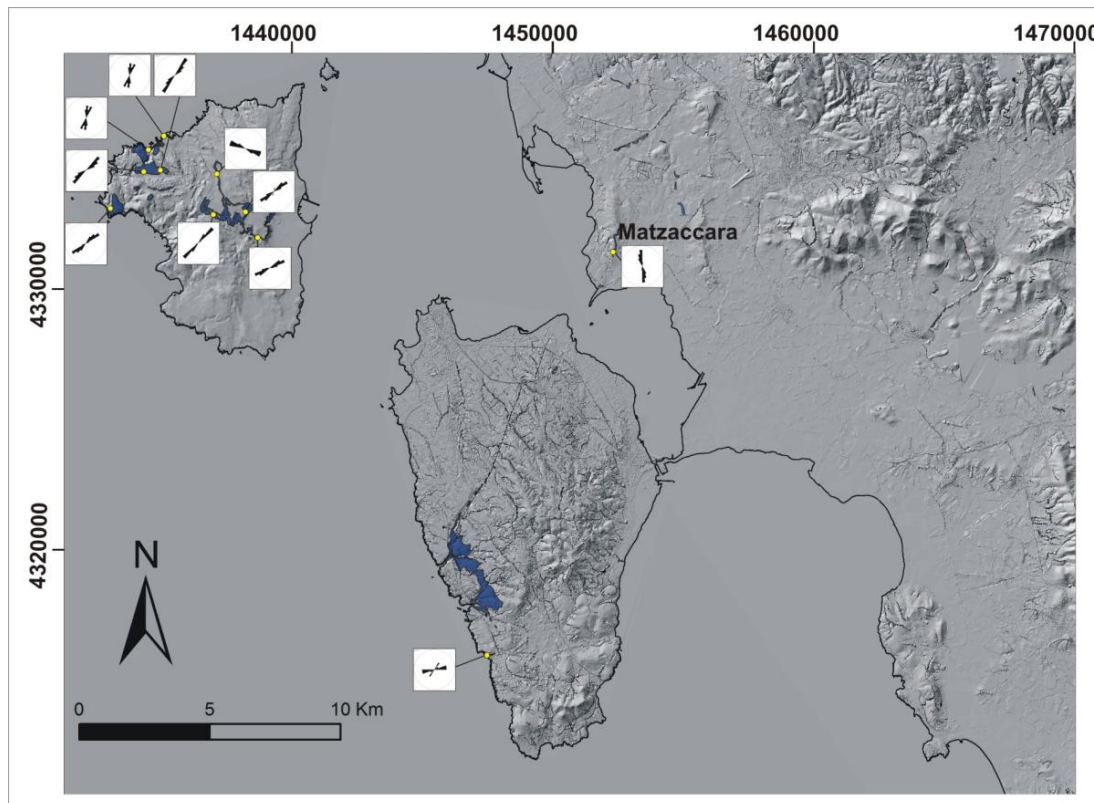
***Fig. 3.11:** Fiammae major axis directions in the Ventrischio Unit*

CHAPTER 4

MAIN STRUCTURES OF MONTE ULMUS IGNIMBRITE

Several macroscale structures occur in the different sub-units of the MUI. Each of these structures can be related with processes occurring at different stages of the complex transport – deposition – emplacement process, or during the final degassing – deformation stage of the deposit.

4.1 Structures related with primary rheomorphism

4.1.1 Ropy structures

Dm- to mm-sized prolate gas cavities, named ropy structures (Pioli and Rosi, 2005), are mainly observed in the matrix-rich ignimbrites cropping out on the Sant'Antioco Island and in the Sulcis area. Like in those observed in the Nuraxi Tuff (Pioli and Rosi, 2005), the inner surfaces of the cavity are characterized by thin, curved ridges in relief of 1-2 mm. These structures are both present in the inner body of lineated lithofacies (cm- to mm-sized) or on the detachment planes characterized by fine-ash matrix (dm- to cm-sized) (Fig. 4.1). Only in some cases, the tips of the structure are observable. The ropy structures present between parting planes have bullet shape while ropy structures present inside lineated lithofacies have surfboard shape.

4.1.1.1 Interpretation

In agreement with Pioli and Rosi (2005), ropy structures represent very good shear-sense indicators for primary flows, especially when developed inside the body of

lineated lithofacies. In the lower half, crest concavity is opposite to the shear sense (and concordant with the flow direction) while in the upper portion concavity is concordant with the shear sense (Pioli and Rosi, 2005). In addition, the presence of these structures on fine-ash-rich detachment planes can be used to understand the sense of movement of secondary flow.

Fig. 4.1:*Ropy structure on a fine-ash-rich detachment plane. The versus of movement is left-ward*

4.1.2 Parting Planes

These structures are well developed especially inside the EPpT facies. Parting planes are generally slightly undulated with metric wavelengths, and spacing between parting planes may rapidly vary both vertically and laterally. Generally, spacing is decimetric to metric in correspondence of topographic lows, while on topographic highs it varies from decimetric to centimetric. Lineations and stretched gas cavities are well visible on the plane view of parting planes (Fig. 4.2). Locally, between different parting planes cm-thick breccia layers are present. Strongly foliated facies often gradually pass to facies characterized by massive beds; breccia beds located on parting planes grade upwards into boudinated layers, weakly folded layers and finally in massive cores.

Interpretation

The association of parting planes with well-developed lineations and stretched gas cavities suggests the occurrence of high shear stresses concentrated along gas-rich layers. The breccia layers between parting planes and the gradual passage up to massive beds are interpreted as related to the focusing of shearing stress along the parting surfaces and gradually decreasing upwards. In addition the presence of breccia layers suggests local development of a fragile behavior caused the high shear stress rate. The formation of parting planes is a clear indication of incremental (possibly stepwise) deposition from the ignimbritic cloud, during which shear stress progressively migrates upward with deposition. The large spacing of parting planes in correspondence of topographic lows is in agreement with this interpretation, suggesting also that it is possibly directly related to the sedimentation rate.

Fig. 4.2: *Stretched gas cavities associated with parting planes (hammer is 33 cm long)*

4.2 Structures related with secondary rheomorphism

4.2.1 Blisters

Blisters have been only rarely described in welded ignimbrites (eg. Fantale volcano in Ethiopia - Gibson, 1974), while their presence has been largely described in lava flows. Recently, blisters structures have been described in another ignimbrite units, the Serra di Paringianu Ignimbrite, of the Sulcis area (Cioni et al., 2001; Mundula et al., submitted). In MUI they are characterized by a metric to decametric diameter and circular-shapes on the horizontal plane views (Fig. 4.3-a). In vertical plane views, blisters are cupola-shaped with slightly planar bases (Fig. 4.3-c). Foliation of the hosting deposit tends to accommodate the blisters (Fig. 4.3-b). Blisters are present in thick sections (>10 m), inside the LPpT facies into sub-unit A2. Only in the area of Sant'Antioco Island, along the cliffs between Cala Sapone and Cala Lunga, 11 decametric-wide blister cavities were counted.

Interpretation

These structures can be interpreted as the result of intrafolial gas migrations, tending to move and to accumulate during deflation or secondary rheomorphic movements, as clearly testified by the reorientation of the foliation planes. The upward growth of blisters is generally stopped at the level of the upper, more rigid (due to the effect of differential cooling) units (in Sant'Antioco area at the contact with unit B). The unusual dimensions of blisters in the MUI (blister are usually described as metric sized), testifies for the very high amount of gas trapped inside the deposits.
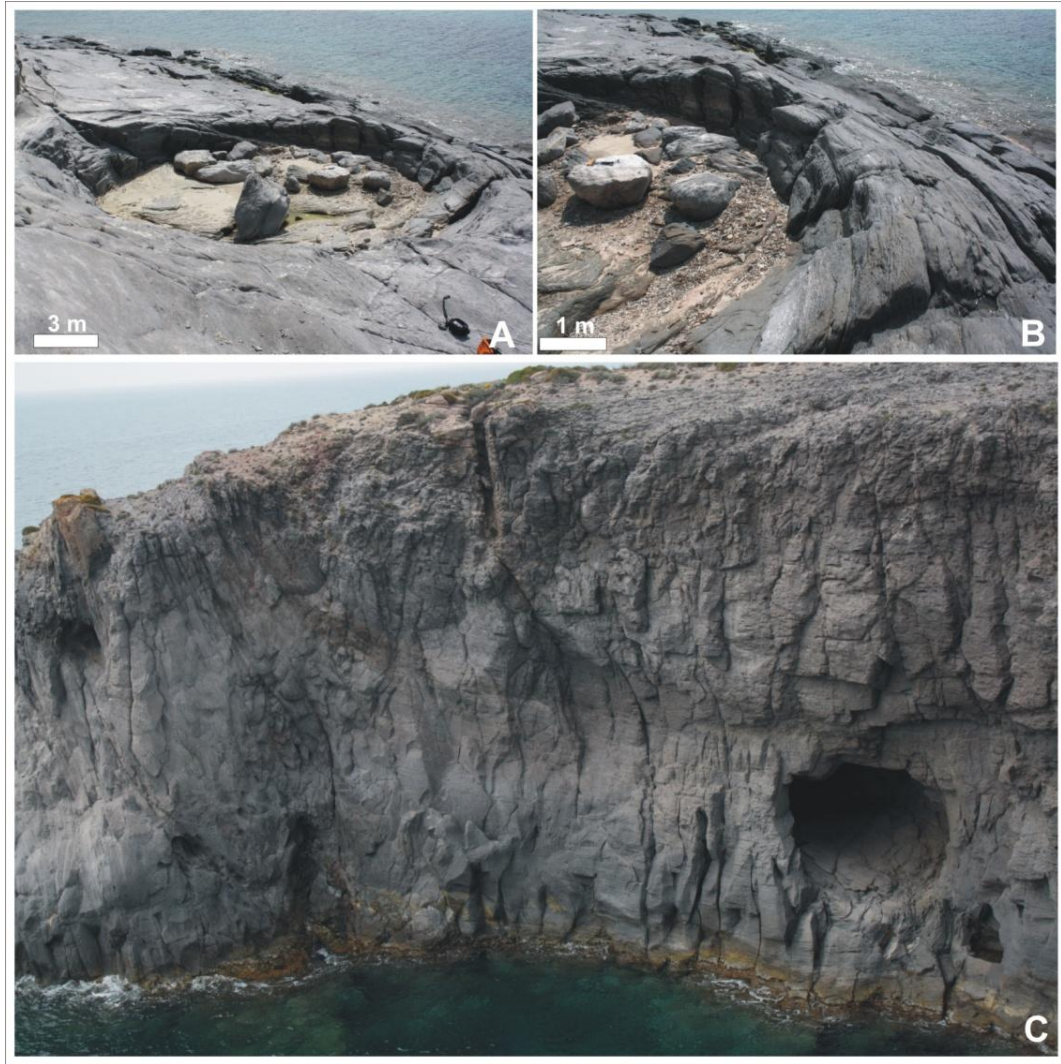
Fig. 4.3: *a) Plane view of decametric blister in Sant'Antioco Island; b) Detail on foliation deformed around blister; c) vertical view of blister in the upper portion of unit A2*

4.2.2 Anticlinal structures and diapir like structures

These structures are observed and described in the western sectors of Sant'Antioco Island. Diapir like structures developed in the presence of a vertical inversion in the average deposit density, and have been also described by Mundula et al. (submitted) for the Serra di Paringianu Ignimbrite. In a few cases, similar structures are also locally observed in the MUI. "Anticlinal structures" are represented, in the case of MUI, by top portions of sub-unit A2 that rise up inside the sub-unit B, here 6 meter thick; in this case, the two sub-units forming these structures have similar bulk rock density (Sub-unit A2 density = 2080 kgm^{-3}; sub-unit B density = 2014 kgm^{-3}). These structures are well

evidenced by the pattern of foliation trends (Fig. 4.4-a). In plane view, they have circular to lobate shapes with diameter around 10 meters. The foliation which envelops the inner body and its core are covered by an orange, argillified halo, 3 to 6 m thick (Fig. 4.4-b). The host rock has a roughly plane parallel foliations. The anticlinal structures observed in Sant'Antioco Island show elongation lineations radially distributed respect to the core. Foliation planes slope radially outward, with angles comprised between 20° (in southern portion) and 50° (in the northern portion).

Interpretation

The limited density difference between sub-units A2 and B exclude the possibility of a "buoyancy-driven" diapiric ascent of sub-unit A2 through sub-unit B. As the area of the Sant'Antioco island is interested by intense post-emplacement rheomorphic processes, one possible interpretation is that the still plastic sub-unit A2 was pushed up inside the stiffer sub-unit B during secondary rheomorphism, probably related with a fracture-open processes (a process similar to bending a candy with a liquid core). The fracture opening and the following pushing-out of lower sub-unit can be confirmed by the asymmetric structures of the inner body, that rose laterally rather than vertically.
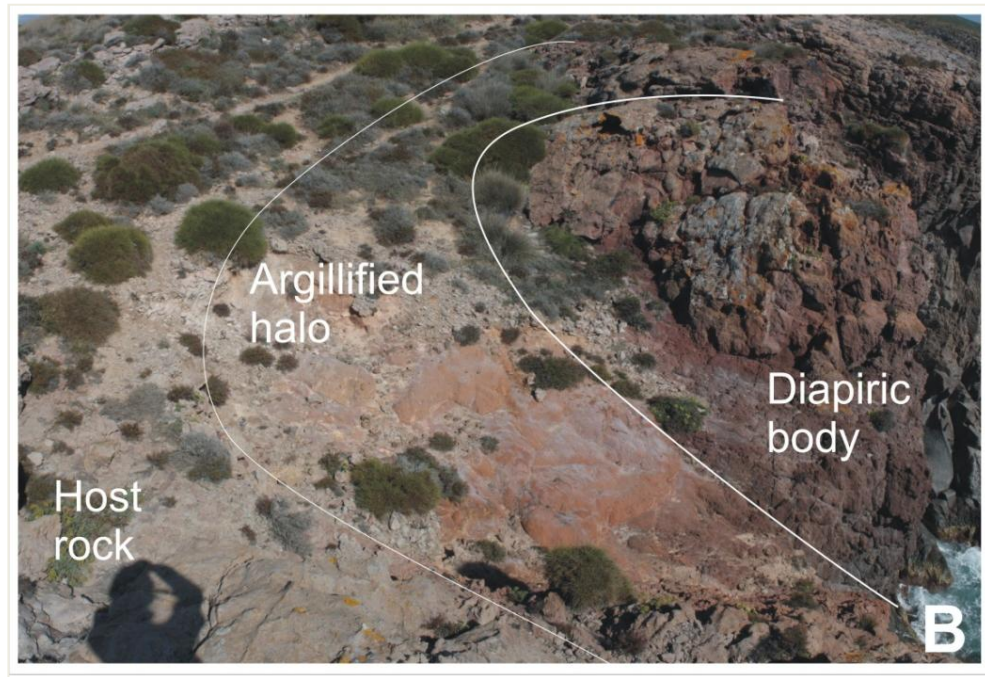
Fig. 4.4: *a) Vertical section view of anticlinal structure in Sant'Antioco Island; B)Plane view of the same structure in which is well exposed the inner body and the argillified halo.*

4.2.3 Ramp-structures

Large ramp-structures are mainly located in the western sector of Sant'Antioco Island and in San Pietro Island, in the upper portion of sub-unit A2 and into the sub-unit B. In the Sant'Antioco Island they are generally west-verging (at a 10° angle), decametric and are characterized by a lower dm-thick breccia layer gradually passing upward into undisturbed layers. In the central area of San Pietro Island they are developed inside sub-unit B, in correspondence of an irregular paleotopography. Basal breccia layers are dm-thick and made by angular to slightly rounded fragments. The upward passage into the undisturbed beds is generally sharp.

In the Matzaccara area, the observed ramp-structures are smaller than those in San Pietro, and show different features. Ramp structures are developed on preexisting parting planes like detachment planes (Fig. 4.5) and they are multiple and have spacing smaller than 1 m. Breccia lenses, 1-2 cm-thick and few decimeters long, are locally present in the ramping body, and not associated with the detachment surface. These

lenses gradually pass into boudinated, revesiculated beds, and finally into undisturbed lithofacies. Ropy structures are locally present on detachment planes.

Interpretation

The formation of ramps might be related to secondary remobilization of the entire deposit after emplacement, or to syn-depositional, rapid re-adjustment of the deposits on gently dipping slopes.

In Sant'Antioco, the deposition on a gently dipping paleosurface possibly caused remobilization of the entire, still plastic, deposit after the end of the emplacement. The same process can explain the formation of the ramp structures observed in the San Pietro Island. The main difference is the fragile behavior of deposits, probably related with the higher viscosity (lower temperature) of deposits.

In the Matzaccara area, the smaller spacing between different ramp structures and the plastic behavior of the deposits are probably related with an immediate re-adjustment on a gently dipping paleosurface (~10° - 15°) of hot deposits during the emplacement phases. The immediate re-adjustment of the still plastic deposits was possibly favored by the abundance of trapped gases, as suggested by the development of the ropy structures.

Fig. 4.5: *Ramp structures in Matzaccara*

4.2.4 Degassing pipes

They are observed exclusively inside sub-unit B in the San Pietro Island. These structure are characterized by 1 meter long and 20 cm large (Fig. 4.6-a), nearly vertical, pillar-like structures enriched in partially loose clasts, matrix-depleted, showing an intense crystallization of vapor-phase minerals around clasts (Fig. 4.6-b). They are stratigraphically sited in the middle portion of unit B; a sharp contact is present on the top of these structures.

Interpretation

Degassing pipes form in the presence of a large amount of coarse juvenile fragments (which favored the easy development of an important permeability in the deposit) and of a low lithostatic load (which favored gas migration in a poorly welded deposit). In analogy to degassing pipes commonly present in loose pyroclastic flow deposits and in sillars, the clast-supported textures can be interpreted as the result of fine ash elutriation during gas loss.

No vertical evidence of lithologic changes is observed in the deposits hosting the degassing pipes. This factor can be interpreted as related to a depositional break during the passage of the same pyroclastic flow, that permitted a rapid gas release from deposits followed by an erosional phase related to renewed passage of the pyroclastic cloud.
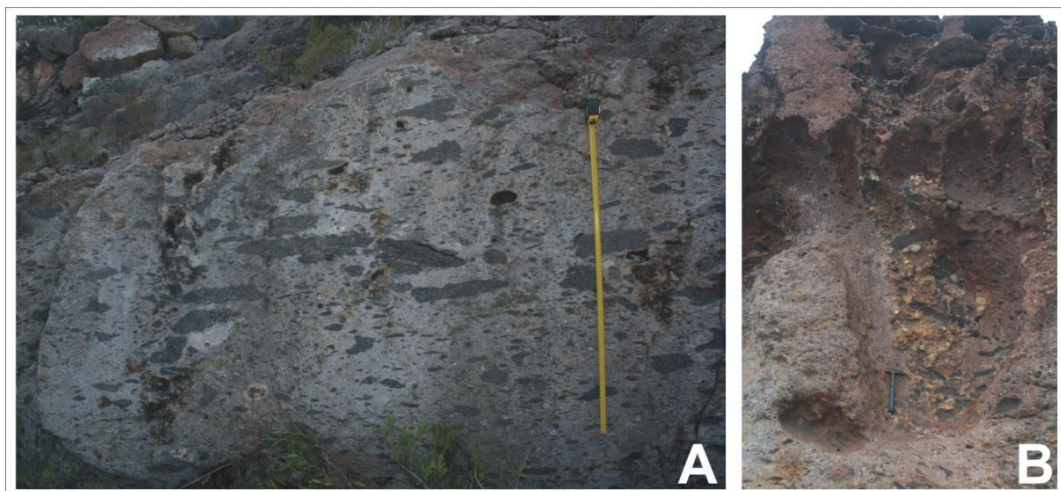
Fig. 4.6: *a) Degassing structure inside the unit B (Loc. Piramide - San Pietro Island); b) Degassing structure inside unit B with intense recrystallization of vapor-phase minerals (Loc. Canale Guidi)*

4.2.5 Megafold

These structure are well exposed on the western sector of Sant'Antioco Island, were MUI outcrops are continuous. These megafolds deform the <1m folds present in the deposit, and are typically open. Megafolds are characterized by a gentle dip of layers (10°-15°), and decametric wave-length ($\lambda \geq 50$ m) affecting the entire deposits thickness (Fig. 4.7). Axes of the megafolds are characteristically perpendicular to the underlying paleoslope, and inclined at different angles to the lineation trends (N110°). They mainly affect the deposits portions located in correspondence of the topographic highs.

Interpretation

This kind of structures is typically related with post-emplacement phases because they involve large portions of the deposit. Megafolds development is suggestive of movement of the stratigraphically and topographically higher portions of deposits, moving towards the valley axis due to gravity. They mark the onset of compressional regime on the deposits.
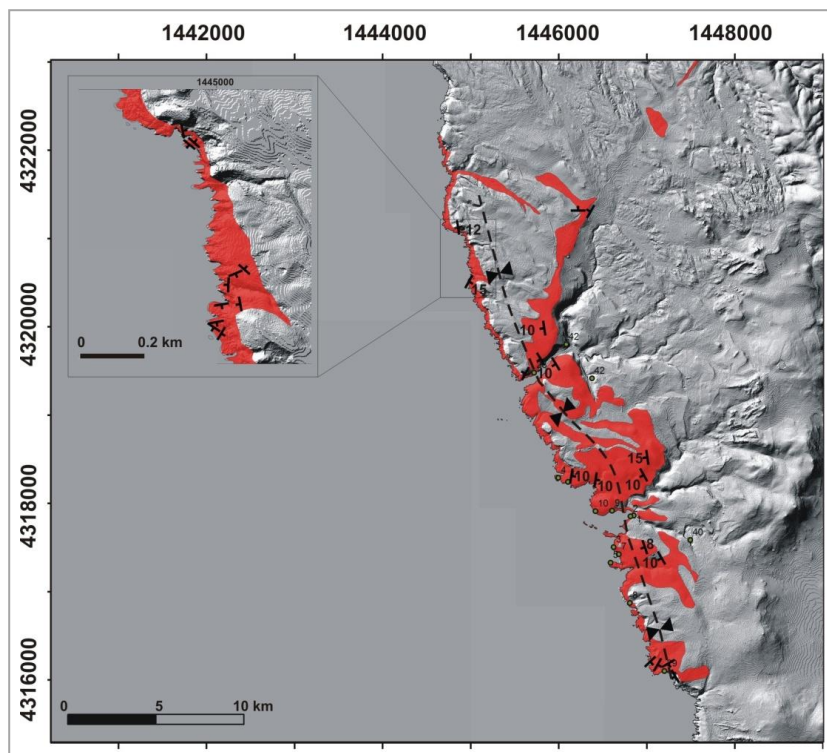
Fig. 4.7: *Decametric-sized folds affecting the western sector of Sant'Antioco Island. On the sketch there are the deep of <1m folds.*

4.3 Micro-scale structures

The study of about 50 thin sections representative of the main lithofacies revealed the presence of several types of microstructures which can help in the interpretation of syn- and post-depositional deformation processes acting on the ignimbrite: rotated fragments (mainly crystals), broken crystals, well oriented and flattened glass shards, Riedel fractures, parting planes, oblate vesicles. These microstructures can be in many cases used as shear-sense indicators, and they can be discussed in terms of the temporal evolution of the physical properties of the deposits, from emplacement to post-depositional phases (degassing and remobilization phases). Rotated crystals (Fig. 4.8-a and b) are generally mm-sized, and are sometimes associated to pressure shadows (Fig. 4.8-c and d). In some cases, crystals have been clearly broken during rotation, and they record the rotation angles. Large, mm-sized glass shards are generally well oriented into the vitrophyric facies (Fig. 4.8-e). In the upper part of the MVT facies, glass shards are still oriented despite an overall decrease in the average size. The effects of lithostatic load at the microscale are recorded in some cases by conjugate fractures on feldspar crystals (Fig. 4.8-f). Crystals oriented parallel to the bedding planes have fractures at 30° respect to the directions of the vertical applied forces.

The detailed study of glass shards orientations allowed also to recognize the (microscale) physical state of the deposits at the moment of deformation, which varied from ductile to rigid with formation of Riedel fractures (Fig. 4.8-h). These fractures, micrometer spaced, show an approximately angle of 15° respect to the main fracture and testify dextral movement of the main fracture. Sharp contacts and embricated layers are well maintained in sub-units A0 and A1 (Fig. 4.8-i). Mm-sized oblate vesicles are well constrained within the foliation planes, and they have their main axis oriented parallel to the bedding plane. Micrometric-spaced parting planes are extensively filled by vapour phase crystallizations (Fig. 4.8-g). The parting planes vary from linear to folded, mainly when in the presence of rotational movements of the clasts. In general, parting planes are parallel to the bedding planes, and can present local reorientation (up to vertical).

Interpretation

All the described microstructures can be interpreted in terms of the passage, during emplacement, compaction and cooling of the deposits, from ductile to plastic to rigid behavior. Ductile behavior during emplacement phases is testified by the occurrence of rotated crystals inducing deformations on the nearest glass shards, and recording in some cases the sense of rotation. Partial rotation and crystal breakage can be due to a different degree of coupling between the crystal and the matrix. The well developed orientation of glass shards can be interpreted in terms of the progressive aggradation of single, large, glass shards and pumices from the rapidly thickening ignimbrite, and of their subsequent pure shear deformation mainly related to the lithostatic load. This process possibly began in the lower vitrophyre, where rapid quenching is testified by the vitrophyric aspect and by the very closely-spaced columnar jointing. The high depositional rate allowed to record the effect of the lithostatic load in very short time, before cooling below the glass transition temperature. The presence of deformations on the parting planes marks a crucial point in the timing of their formation. Finally, the presence of Riedel fractures suggests that the dextral deformation occurred also during the passage from the ductile to fragile deformational regimes, associated to viscosity increase.
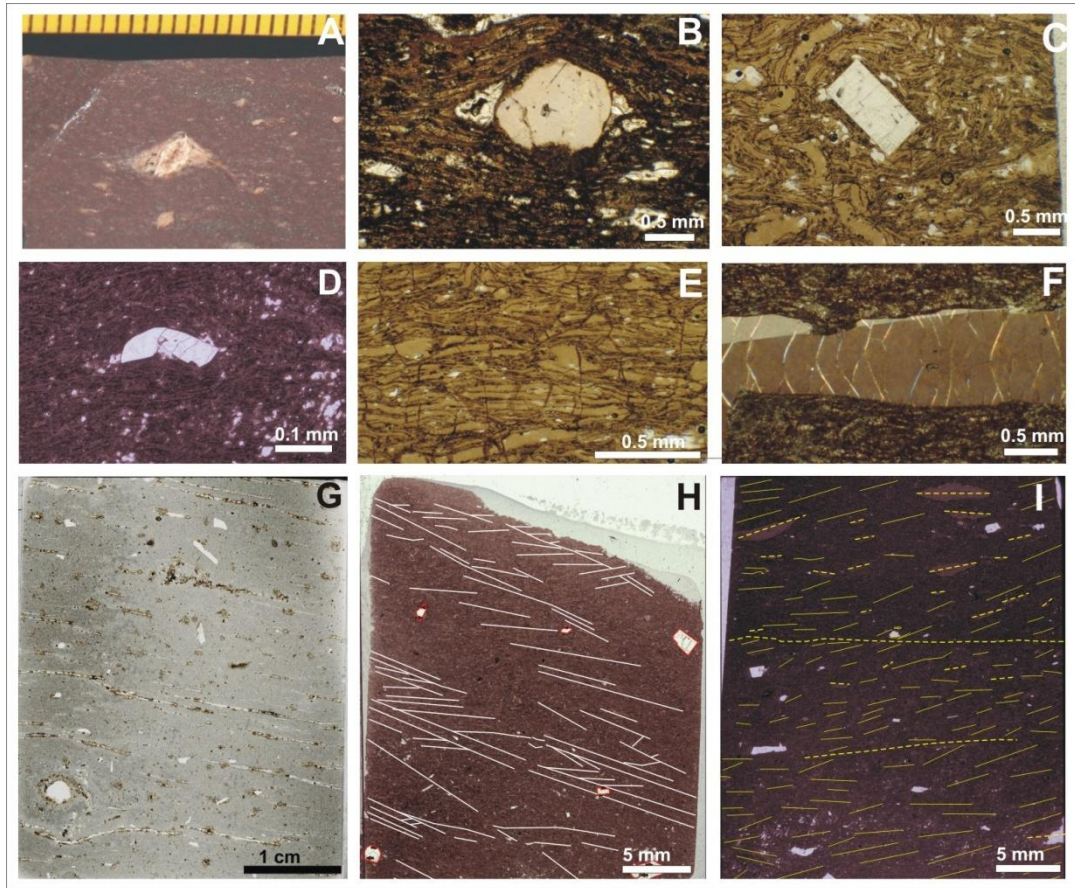
Fig. 4.8: *a - b) rotated crystal with pressure shadows; c) angular crystal clock-wise rotated; d) partially broken rotated crystal; e) well oriented glass shard in basal vitrophyre; f) conjugate fracture in a feldspar crystal; g) parting-planes in lineated lithofacies; h) Riedel's fracture highlighted by glass shards orientation; i) sharp contact and embricated layers into vitrophyre highlighted by glass shards*

4.4 Strain analyses

The analyses were focused on primary structures where they were still visible and where the interactions between rigid fragments can be considered negligible (following Pioli, 2002 method).

Different rotational structures (σ, δ and Φ types), similar to the ones in mylonites (Passchier and Trouw, 2005) were recognized testifying different typologies of shear. The analyses were focused on normal and parallel-to-shear oriented thin sections. Two main classes were considered during analyses on the base of their aspect ratios: one comprised between 1.5 and 2 and the second one comprised between 2 and 3.5.

Fragments with aspect ratio lower than 1.5 and higher than 3.5 weren't considered. More details about the methodology used are in appendix chapter.

In the "normal-to-shear" thin-sections were studied principally σ-type rotational structures. In the samples of the lower portion of stratigraphic sequence, all particles were strongly oriented with α values (angle between the mayor axis and shear direction) near to 0° (parallel to sedimentary planes). Upward, only particles with higher aspect ratios (2-3.5) shows well re-orientation degrees while the other particles have high ranges in α values (Fig. 4.9). In the basal thin-sections oriented "parallel-to-shear direction" the particles generally shows a well oriented pattern. Considering separately the two AR classes, the fragments with AR=1.5-2 have high variability in α values. In contrast the fragments with AR higher than 2 are well oriented with the shear direction. The W_k values (Tikoff and Fossen, 1998; Ventura, 2001) cover all the range from 0 (pure shear) to 1 (simple shear) but with a median values near to 1. Knows the fragments behavior with the stratigraphic height and the particles rotational angles we can understand if these particle were reoriented under pure shear or simple shear.

Interpretation

The upward variability in α values can testify a different vertical degree in shear strain recorded near the flow boundary zones. The different behavior of fragments with AR comprise between 1.5 and 2 can highlight the variable degree of shear stress taking in account that fragments with higher aspect ratio can rotate easily also with low shear stress.

Taking in account the W_k values is clear that the rotational processes are linked principally with simple shear in lineated lithofacies.
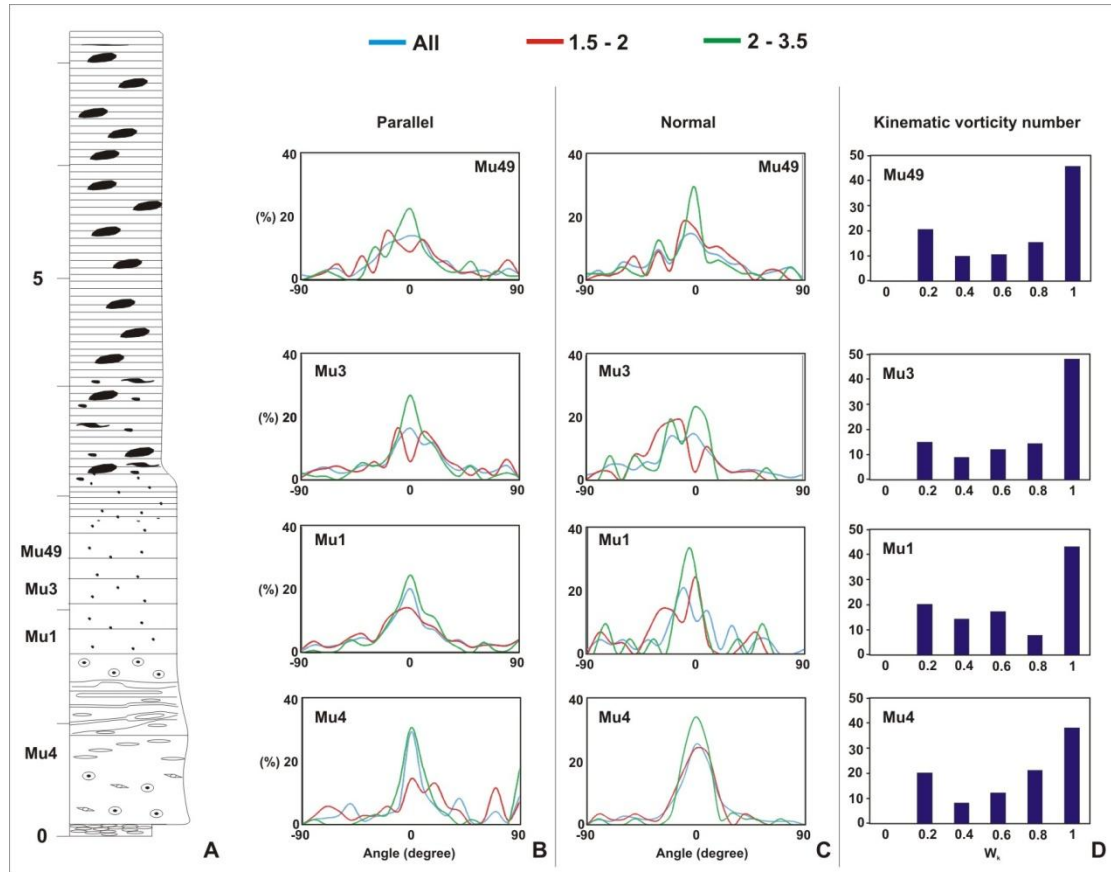
Fig. 4.9: a) Stratigraphic log of section 6 (Matzaccara); b) Distribution of crystals orientation in thin-sections cut parallel to flow directions; c) Distribution of crystals orientation in thin-sections cut normal to flow directions. d) Wk histogram (kinematic vorticity number) values show the large affinity of rotational processes with simple shear. Different color are for different AR fragment classes and angle was measured between the main axis and the shear direction..

CHAPTER 5

STRATIGRAPHY AND LITHOFACIES OF MONTE ULMUS IGNIMBRITE

5.1 Introduction

The first studies on Monte Ulmus Ignimbrite (MUI) go back to Taricco (1934), who made the first petrological characterization of the San Pietro and Sant'Antioco Islands stratigraphy, describing the MUI as part of the final rhyolitic products (lava, tuffs and ignimbrites) named "post-τ4" products. Afterwards Garbarino and Maccioni (1970) proposed a new subdivision based on volcanological, geochemical and petrographycal criteria. Assorgia et al. (1990), proposing a new stratigraphic scheme for the Sulcis Volcanic District, initially distinguished the MUI with the name of "Cala Lunga Unit", lastly changed into Monte Ulmus Unit (Assorgia et al., 1990).

The MUI crops out discontinuously over an area of 300 km^2. Considering the large areas in which MUI was eroded, covered by younger ignimbrites or presently under the sea-level, the MUI minimum estimated total volume is 2.5 km^3.

The Monte Ulmus Ignimbrite presents a roughly constant thickness of about 10 m near Giba (southern sector of Sulcis area), while on Sant'Antioco Island, where it has a thickness ranging from 3 m to 23 m, it generally rests on a gently dipping paleosurface (~10°). In contrast, on the San Pietro Island and on the northern sector of Sulcis area, the ignimbrite shows strong lateral thickness variations (7 to > 98 m) (Fig. 5.3-a).

5.2 Stratigraphy

General stratigraphy of the MUI was reconstructed and described in detail at more than 41 sites, located in all the main areas where the MUI had been mapped in the new 1:50000 geological map of the Sulcis area.

On the basis of the vertical lithological variations and of the presence of sharp and erosive contacts, angular unconformities and lithic-rich layers, the MUI has been divided into five main sub-units: a basal fall deposit (F) followed by four welded pyroclastic flow deposits named, respectively, A0, A1, A2 and B (Fig. 5.2).
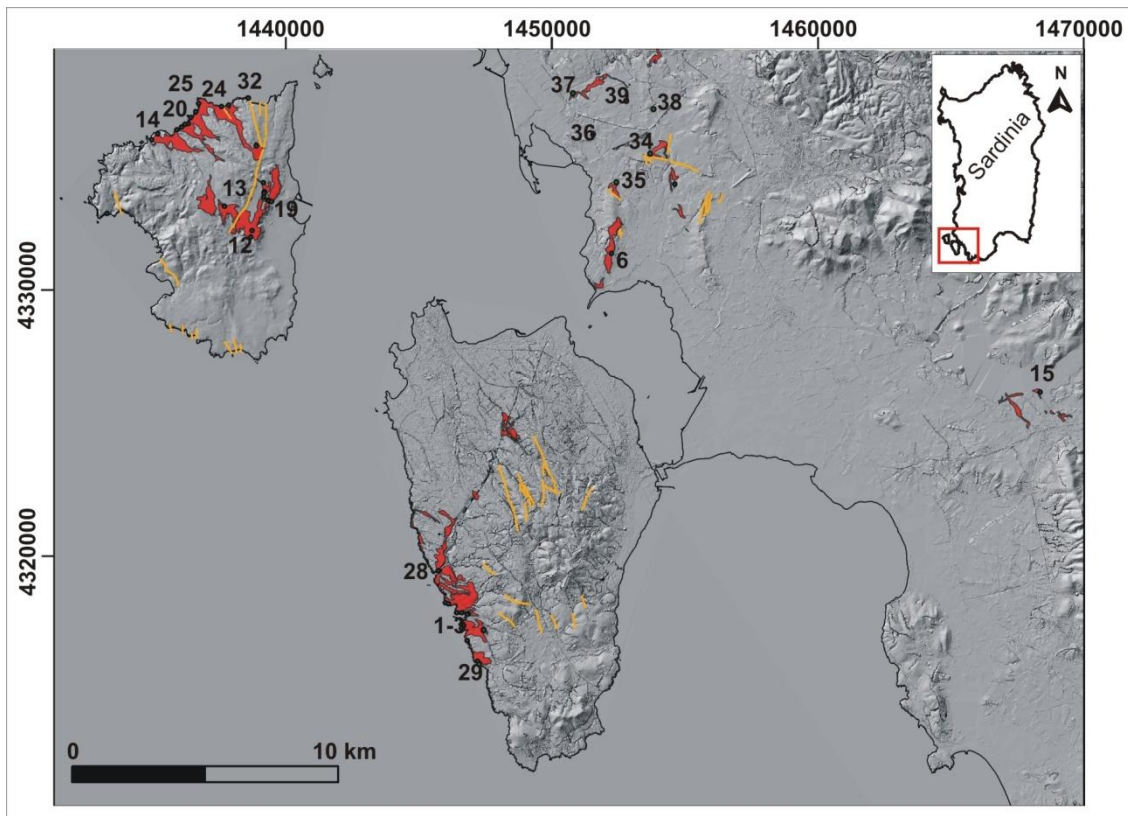
Fig. 5.1: *Main stratigraphic sections of the Monte Ulmus Ignimbrite*

5.2.1 Basal fall deposit F

A fallout deposit, 2 to 20 cm thick (Fig. 5.3-b), is present at the base of the MUI, directly overlying a reddish paleosoil. It is constituted by lapilli and coarse ash pumice, locally argillified. The fall deposit, where not completely argillified, is normally graded and presents a basal layer mainly constituted by lapilli-sized pumice clasts, grading upward to coarse ash. Few lithic fragments (mainly of older ignimbrites) and loose quartz crystals are present, with a maximum size of 1 mm.

5.2.2 Sub-unit A0

Sub-unit A0, 10 to 80 cm thick (Fig. 5.3-c), crops out extensively in the Sant'Antioco and San Pietro Islands. It is a blackish, isotropic, vitrophyric, partially welded ignimbrite deposit. In the Sulcis area (close to the Matzaccara village) it is completely argillified. The contact with the underlying fall deposit is sharp, locally erosive.

Whitish and blackish, slightly oblate (AR ≈ 3), cm-sized fiammae are well visible in the Sant'Antioco area. Angular to slightly rounded, cm to mm-size lithic fragments (~5%, mainly ignimbritic and lava fragments) are present. Angular to sub rounded alkali feldspar and quartz crystals (2-3 % by volume, finer than 1 mm) are also present.

5.2.3 Sub-unit A1

Sub-Unit A1, 1 to 30 m thick (Fig. 5.3-d), has its greater thickness in the Sant'Antioco Island. The contact with the underlaying sub-unit is sharp, locally erosive. It is a reddish, vitric, matrix supported, partially to densely welded ignimbrite. Two main different types of fiammae are present: blackish, glassy, not vesicular, eutaxitic to parataxitic fiammae (5-6 vol.%) with AR ranging from 15 (on topographic highs) to ≈ 30 (in topographic lows), and whitish, vesicular, sub-rounded fiammae (1 vol.%), with AR ≈ 2 ÷ 3. Angular to sub-rounded lithics (5-8 vol.%) are mainly represented by fragments of older ignimbrites. Quartz and alkali feldspar crystals (2-3 vol.%) are smaller than 1 mm. Well developed cm- to dm-spacing, undulating parting planes are present in this sub-unit.

5.2.4 Sub-unit A2

Sub-unit A2, 0.2 to 2 meters thick (Fig. 5.3-e) , widely crops out in Sant' Antioco Island and Sulcis area, where it shows its greater thickness. It is a reddish to yellowish, crystal poor, partially to moderately welded ignimbrite. The contact with the underlying deposit is sharp. It is characterized by dm-sized, eutaxitic to slightly parataxitic blackish fiammae (AR ≈ 13). Mm-sized feldspar crystals and mm-sized angular lithic fragments are presents, with a volume abundance around 5%.

5.2.5 Sub-unit B

Sub-unit B (Fig. 5.3-f), 4 to 52 m thick, crops out extensively on the entire studied area. The contact with the underlaying sub-unit is sharp and in few cases cross-cuts the rheomorphic foliation of sub-unit A2. In the Sant'Antioco Island this contact is marked by a 5 cm thick, blackish, glassy layer. Generally, sub-unit B is a crystal-poor (~3 vol.%), spatter rich, partially to densely welded ignimbrite. In the San Pietro Island it shows evident grain size and textural variations; it is reversely graded in the first 20 cm, followed by a massive sedimentary organization in the central portion and passing to normally graded in the upper portion. The lower portion of sub-unit B is a reddish, eutaxitic, fine to coarse grained, partially to densely welded tuff. The central portion, rich in lithic blocks, is a grey, isotropic, moderately welded ignimbrite. The upper portion of sub-unit B is a light-gray, eutaxitic partially welded tuff.

This sub-unit is characterized by abundant cm- to dm-sized (~16 vol.%) juvenile fragments. Three main types of juvenile fragments are recognizable: i) blackish, highly porphyritic (Sd-bearing), plastically deformed, dense fiammae, ii) reddish, crystal-poor, fine grained, plastically deformed fiammae, and iii) whitish, vesicular, rigid-like scoriae. Angular to sub-rounded lithic fragments are well represented (2-3 vol.%), generally showing normal grading (from boulders to fine lapilli upward). In the San Pietro Island, sub-unit B bears lithic and pumice boulders up to 70 cm in size. Free crystals (10 vol.%) reach maximum size of 2 mm.

B: 4 to 52 m thick, crystal-poor, spatter rich (max dimensions 70X40 cm), partially to densely welded eutaxitic ignimbrite.

A2: 0.2 to 2 m thick reddish to yellowish, crystal poor, partially to moderately welded ignimbrite.

A1: 1 to 30 m thick, reddish, vitric, matrix supported, partially to densely welded ignimbrite.

A0: 10 to 80 cm thick, blackish, isotropic, vitrophyric, partially welded ignimbrite.

F: 2 to 20 cm thick, partially to totally argillified, fall deposit.

Fig. 5.2: *Stratigraphy and main features of the Monte Ulmus Ignimbrite; reconstructed section*
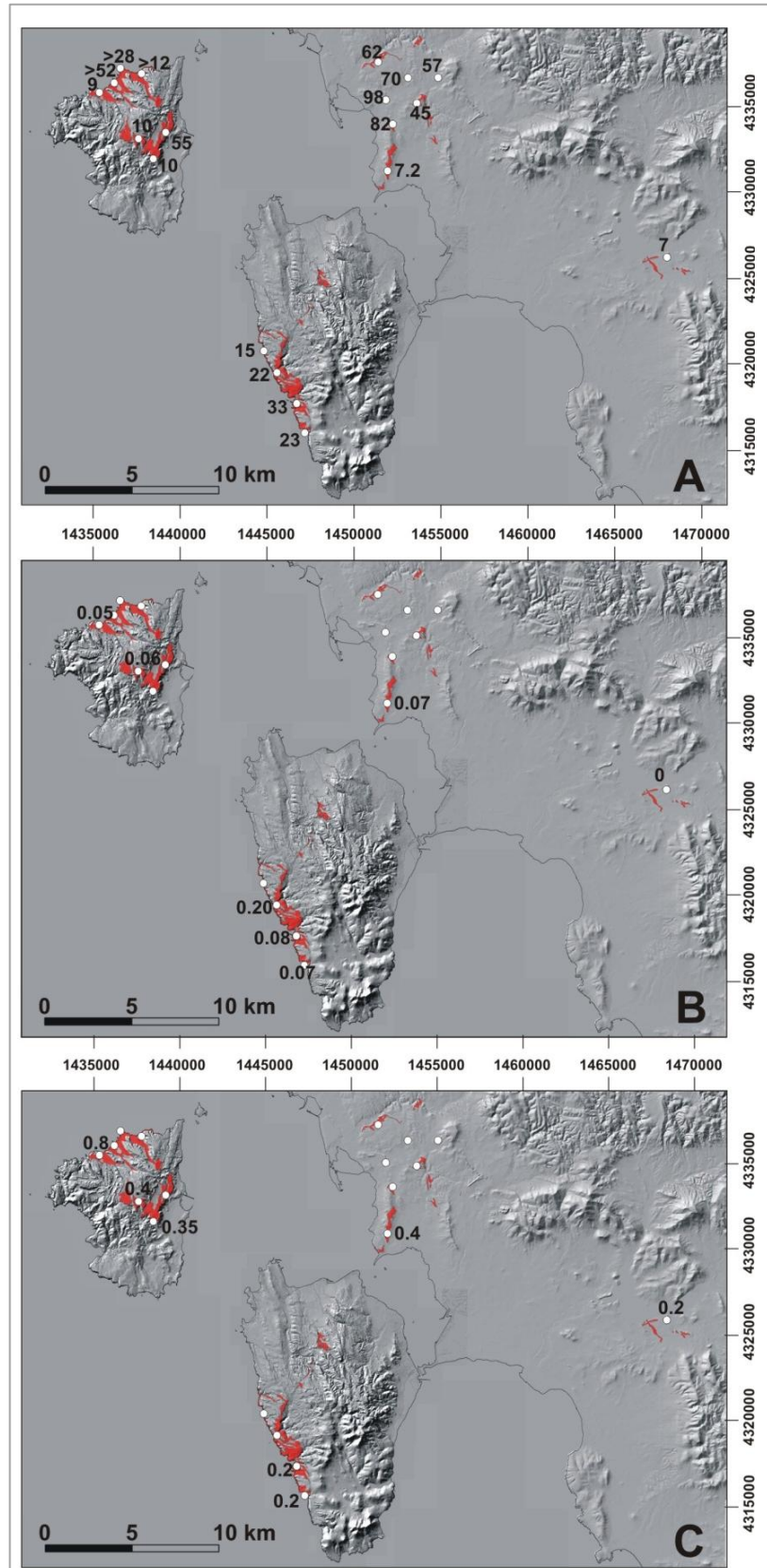
Fig. 5.3: *Thickness of the Monte Ulmus Ignimbrite: a)Total; b) Basal fall deposit; c) Sub-unit A0*
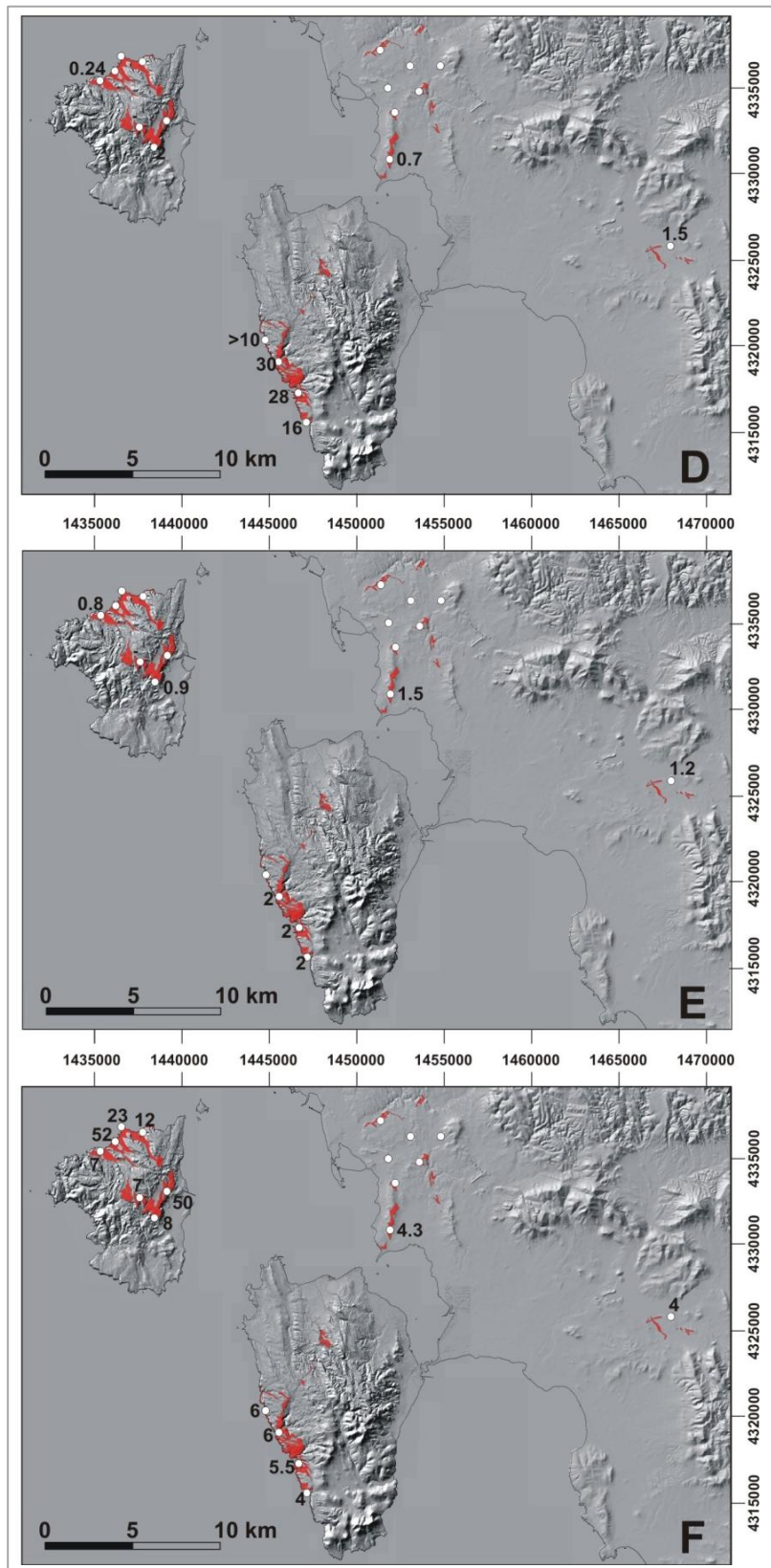
Fig. 5.3: Thickness maps of Monte Ulmus Ignimbrite: d) Sub-unit A1; e) Sub-unit A2; f) Unit B

5.3 Lithofacies

According to the definition given by Branney and Kokelaar (2002), the term lithofacies defines "a no-genetic and no-stratigraphic set of shared characteristics of deposits, such as grain size, sedimentary and rheomorphic structures, welding intensities, crystallization styles and local deposits geometries". Vertical and lateral lithofacies changes inside an ignimbrite deposit can testify different conditions and processes during emplacement in the flow-boundary zone (Branney and Kokelaar, 1992). A pyroclastic flow unit can be composed by one or more lithofacies and conversely more pyroclastic flow units can share the same lithofacies. The identification of some main lithofacies and the definition of their lateral and vertical variations is important to understand the emplacement processes and the main events that influenced the deposits during and after the emplacement. In addition, lithofacies characteristics and vertical and lateral variations can help in understanding the possible position of the source area.

5.3.1 Main lithofacies of Monte Ulmus Ignimbrite

In the study of MUI stratigraphy, the choice of the reference sections was mainly made on the basis of their paleotopographic conditions and variable occurrence of the different lithofacies. In this work, the detailed study of some reference sections, is so used to recognize and discuss the main features of the deposits. The main goal is to relate each lithofacies to its stratigraphic position (base, central or upper portion of deposit) and to the paleotopographic conditions at emplacement.

Basing on the main features described in the different paleotopographic conditions, we recognized 7 main primary lithofacies, each corresponding to different flow regimes and depositional and, eventually, remobilization processes. The general scheme of Branney and Kokelaar was followed in order to define the main lithofacies. The main lithofacies are the following: I) massive vitric tuff; II) massive with vesicles tuff; III) massive isotropic with breccia tuff; IV) lineated tuff with parting planes; V) eutaxitic poorly sorted tuff; VI) eutaxitic with degassing pipes tuff; VII) eutaxitic xenolithic blocks-bearing tuff (Tab. 5.1).

I) **M***assive vitric tuff (MVT) lithofacies*: generally 0.1 to 1 m thick, this facies consists of blackish to reddish, massive, vitric to partially argillified, partially to densely welded deposits. Cm spaced columnar joints cross cut this lithofacies.

Mm- to cm-sized, blackish and whitish platy vitric fiammae have an average aspect ratio (AR) of about 3:1 in the Sant'Antioco Island deposits, and 30:1 in the San Pietro Island deposits (Fig. 5.4). Dispersed, broken to intact, free crystals (Qtz + Sd) represent about 5 vol.% of the total. Cm-sized lithic clasts are angular to sub-rounded. Symmetric pressure shadows are present, disposed around free crystals and lithic fragments. Oblate, cm-sized lithophysal cavities are ubiquitous.

At the microscale, mm-sized glass shards generally display a well developed parallel bedding, locally folded with a cm-wavelenght. Glass shards in the MVT lithofacies are generally in direct contact, without interstitial matrix in the outcrops of the San Pietro Island, while matrix is present between glass shards of the outcrops on the San Antioco Island.

All glass shards types (Y-shape, X-shape and cuspate) are well oriented along a parallel bedding. In some layers, glass shards are embricated with angles of 30° respect to the sedimentation plane. Matrix is cross cut by a well developed perlitic fractures, and locally presents cm-long, µm to mm-space Riedel fractures. Pressure shadows around Φ-structures are also sporadically present.

Interpretation

The glassy matrix at the base of the lithofacies and the centimetric-spaced columnar jointing suggest a high cooling rate for the first centimeters of this lithofacies. The perlitic fractures cross cutting the glass shards are a consequence of the high cooling rate and following hydration of the basal portion of the deposits (Davis and McPhie, 1996; Andrews and Branney, 2010). The strong orientation of glass shards and the presence of symmetric pressure shadows are well explained with a welding process driven by lithostatic load (pure shear), more developed on the basal portions of those deposits filling paleovalleys, where thickness reaches the maximum values (Streck and Grunder, 1995; Sumner and Branney, 2002). The increase in matrix, and the decrease in sorting and in grain size of the glass shards from San Pietro to Sant'Antioco sections can be interpreted as the result of a passage from a laminar, high density, possibly no-

particulate basal flow to a particulate, more dilute flow with distance. The Riedel fractures, together with the mm-size folds, are interpreted as the result of rheomorphic deformation in fragile-ductile conditions (Passchier and Trouw, 2005), probably at temperatures close to the Tg. The flattening of fiammae varies, according with the inferred distance from the source area and with the paleotopographic conditions. Lithophysal cavities are commonly related to the syn- and post-emplacement processes of volatile loss from the base of the deposit, possibly favored by on the presence of a wet substrate.

Fig. 5.4: *The high AR fiammae inside the MVT lithofacies in the Sant'Antioco Island*

II) *Massive with vesicles tuff (MvesT) lithofacies*: this facies, 1-2 meter thick, is a reddish, massive with vesicles, partially to moderately welded tuff. Cm-sized blackish vitric fiammae are platy, with size varying from ash to lapilli, and they have eutaxitic textures. Mm-sized feldspar crystals are less than 5 vol.%; angular to slightly rounded lithic clasts, mainly represented by fragments of ignimbritic rocks, are present.

Bladed, mm- to dm- sized, vesicles have their main axis on the foliation planes; in the San Pietro Island (Fig. 5.5) they reach the maximum length, while in the Sulcis mainland (Matzaccara area) they are generally mm-sized. σ and Φ-type structures are

well developed around crystals and lithic fragments, sometimes with well developed pressure shadows. Micrometric glass shards are still visible and well oriented, parallel to the depositional planes. Locally this lithofacies is affected by secondary rheomorphic processes, with formation of detachment planes.

Interpretation

The sedimentological features of the lithofacies are suggestive of deposition from the body of a PDC. The presence of oblate vesicle can be related to an early degassing stage of the deposits, possibly immediately following emplacement and preceding deformation related to lithostatic load. In addition, the presence of ϕ structures confirm a dominance of pure shear (related to lithostatic load) respect to simple shear.

Fig. 5.5: *the MvesT lithofacies*

III) *Massive isotropic with breccia (MIbrT) lithofacies***:** this lithofacies is 1-2 meters thick. It is a massive, isotropic, very poorly sorted, lithic and juvenile blocks rich, matrix-supported, partially to moderately welded tuff. It is mainly present in the San Pietro Island (Fig. 5.6).

Whitish, angular to sub-rounded pumice fragments are up to 50 cm in diameter; blackish, platy, crystal-rich, sometimes deformed vitric spatters reach diameters up to 30 cm. Dm-sized, sub-rounded to angular lithic boulders are mixed together with large pumices and platy spatters. Two types of lithic boulders are recognizable: decimetric to

metric sized (until 110cm – Fig X), rounded, reddish, low-porphyritic ignimbritic fragments, and cm-sized, angular, blackish, crystal-rich lava fragments. Sparse cm-sized lithophysal cavities are present.

Interpretation

The coarse grain size (boulders) of lithic fragments and the poor sorting of this lithofacies in the different paleotopographic condition suggest proximity to the source area. The rapid upward enrichment in lithic blocks can be related with a waxing phase of the eruption. These features can be interpreted as related to an increasing erosive potential during flow emplacement (Pioli, 2002).

Fig. 5.6: dm-size lithic blocks of the MIbrT above the MVT lithofacies in the San Pietro Island

IV) *Lineated tuff with parting planes (LPpT) lithofacies***:** this lithofacies is generally represented by a 0.4 to 2 m thick, lineated, partially to densely welded, fine ash tuff. Pervasive foliations marked by parting planes locally characterize the lithofacies and are variably spaced along the whole thickness (Fig. 5.7). Mm- to cm-sized, well oriented fiammae have rod-like shape, high aspect ratio (until 20:1) and size ranging from ash to lapilli. Millimeter-sized lithic fragments are mainly formed by older ignimbritic rocks. Loose, mm-sized, generally unbroken crystals of feldspar are present. This lithofacies shows a large number of structures at different scales. Millimetric to decimetric sized

structures are: rotated fragments (σ and Φ structures), ropy structures (both inside parting planes and within single beds), mm-sized tension gashes, embricated fiammae, sheet joints, sheet folds, pervasive parting planes and, locally, breccia or boudinated layers. Metric to decametric structures are instead represented by mega folds (>10m), anticlinal structures, blisters and ramps.

Interpretation

The presence of σ rotational structures, prolate vesicles and pervasive flow banding testify to syn-depositional rheomorphism, related to the presence of a shear stress gradient at the interface between the deposit and the transport system above. Similar facies have been described in other high-grade rheomorphic ignimbrites, as the Grey's Landing ignimbrite - Idaho (Andrews, 2006) or the D Ignimbrite - Gran Canaria (Kobberger and Schmincke, 1999). The presence of pervasive parting planes and blisters is related with large amount of gas inside the deposits. Parting planes are interpreted like zones of preferential gas concentration during emplacement. The development of blisters suggests remobilization and migration of the trapped gas mainly along the parting planes, into a still plastic deposits. A prolonged permanence of the deposit in a plastic state is also suggested by the development of metric to decametric structures (megafolds and anticlinal structures) in correspondence of highly sloping topography.

Fig. 5.7: *mm-spaced parting planes in the area of Matzaccara (Sulcis)*

V) *Eutaxitic poorly sorted tuff (EpsT) lithofacies:* 1 to 20 m thick, it is a reddish to grey, eutaxitic, poorly sorted, fine grained, partially to moderately welded, matrix supported ignimbrite.

The lithofacies is characterized by abundant (17% vol.), cm- to dm-sized, platy fiammae, normally graded. Two main types of fiammae are recognized: dm-sized, blackish, crystal-rich, vitric, locally plastically deformed fiammae (AR between 1 and 2.25) (Fig. 5.8), and cm-sized, crystal poor, rigid, whitish scoriae with mm-sized rounded vesicles. The abundant angular to sub-rounded lithic fragments (~10 vol.%) are mainly represented by fragments of older ignimbrites. Mm-sized, broken feldspar crystals are still visible in the matrix. Sparse lithophysal cavities are present in the lower portions of this lithofacies. Other structures like rotated fragments and elongated micro-vesicles are present inside the matrix. Due to the high amount of coarse fragments, these macroscopic strain indicators are generally not well developed. The EpsT is characterized by a strong upward decrease in average grain-size of spatter fragments.

Interpretation

The great amount of large spatter clasts suggests a phase of the eruption characterized by a coarse fragmentation of a hot, low-viscosity magma (Valentine et al., 2000). This lithofacies is interpreted as the product of the deposition of pyroclastic flows in which welding was favored by pure shear related to lithostatic load (Andrews and Branney, 2010). The effect of shear stress (if present) is not well recorded or completely obliterated by the interaction between fragments. The concurrent presence of rigid pumices and plastic fiammae can be related to a different cooling history for these two components, probably due to their different chemical compositions (variable from trachyte to rhyolite) or their different cooling history (f.e. inherited from a different position in the collapsing fountain).

Fig. 5.8: *eutaxitic texture of the EdpT lithofacies*

VI) ***Eutaxitic with degassing pipes tuff (EdpT) lithofacies***: 1 to 3 meter thick, it is only developed in the presence of a high percentage of coarse components. It is a grey, eutaxitic, poorly sorted, fine grained, moderately welded ignimbrite deposit. There are two main types of juvenile fragments: dm- to mm-sized blackish vitric, crystal rich spatters, and mm-sized whitish, crystal-poor, non- vesicular fiammae. Cm-sized angular lithic fragments (5-8 vol.%) are mainly of older ignimbritic blocks. Cm-sized, sub-rounded gas-cavities are dispersed inside the deposits. Clast-supported, decimetric to metric degassing pipes are present (Fig. 5.9), characterized by a strong depletion of ashy matrix and by vapour-phase crystals between fragments. At top of the degassing structures, the lithofacies shows a sharp erosive contact with the upper EpsT lithofacies.

Interpretation

According to Branney e Kokelaar (2002), this lithofacies is interpreted to represent the upper, proximal, gas-rich portions of the ignimbrite, where lithostatic load is so low that the gas can escape. According to the same authors, this lithofacies usually forms near the boundary layer when overlays of a non-particulate flow. The vertical orientation of the degassing pipes indicates that they formed after transport had ended or simply that the deposit did not undergo secondary rhemobilization. The presence of degassing pipes and the rapid upward decrease in grain size can be interpreted as a gas-rich deposit

emplaced from a steady current characterized by a fluid escape-dominated flow boundary zone. Taking into account the ubiquitous presence of an upper erosive surface, we suggest that erosion by the following passage of ignimbritic clouds contributed to reduce the lithostatic load, favoring degassing and elutriation processes.

Fig. 5.9: degassing pipes in the Piramide section on the San Pietro Island

VII) *Eutaxitic xenolithic blocks-bearing tuff (ExbT) lithofacies***:** 2-3 meter thick, this lithofacies is only present in the San Pietro Island. It is a grey, eutaxitic, poorly sorted, moderately welded ignimbrite. Blackish, vitric, crystal-rich spatters reach maximum length of 40 cm. Whitish microcrystalline ignimbritic xenolitic blocks, up to 1 meter long, are characterised by platy shapes (0.7 oblateness values), sub-rounded edges and internal foliation concordant with the eutaxitic structure of ignimbritic body (Fig. 5.10). A mm-sized vitric rim is sometimes present around the xenolitic blocks.

Interpretation

This lithofacies is considered separately even though generally it has the same features on the EpsT mainly due to the presence of the large xenolitic blocks, suggesting proximality to the source area. In particular, the vitric rims of the coarse xenolitic blocks and the sub rounded edges suggest that blocks were possibly taken in charge by the

erupting mixture before magma fragmentation. The coarse grain size of the blocks and their fragility are suggestive of a rapid deposition, possibly within a laminar flow in which blocks travelled like a surfboard, in the absence of important chaotic movements which could have induced breakage.

Fig. 5.10: *metric-size boulder on the on the Piramide section (San Pietro Island)*

5.3 Devitrification facies

While the main lithofacies features give information about the mechanisms acting during transport and deposition of the ignimbrite, the crystallization and devitrification features of the matrix can be interpreted in terms of the post-depositional, cooling history of the deposit.

Glass is a thermodynamically unstable substance which tends to alter and to be replaced by a dense intergrowth of tiny minerals such as zeolites, phyllosilicates or palagonite. The devitrification process involves nucleation and growth of crystals at a sub-solidus temperature. It generally occurs during cooling of hot coherent glasses in densely welded pyroclastic deposits. Typical products of high temperature devitrification of silicic glasses are spherulites, lithophysae, orbicular textures and micropoikilitic textures, mainly composed of fine-grained quartz and feldspar crystals. The rate of

devitrification is dependent on temperature and on the presence and composition of aqueous solutions (Lofgren, 1970). The presence of alkali-rich solutions increases devitrification rates by four to five orders of magnitude compared to dry conditions, or if the solution is pure water at temperatures below about 300 °C (Lofgren, 1970).

Spherulites are radiating arrays of crystal fibres that make a single crystal with a slightly different crystallographic orientation from adjacent crystals. Spherulites typically have diameters of 0.1 – 2 cm but may be larger (10-20 cm) and, where they can grow isolated, they are commonly spherical. In rhyolitic glasses, morphology of spherulites changes according to the temperatures of formation. High temperatures spherulites (700 °C) are open clusters with spaced crystal fibers. At intermediate formation temperatures (400 - 650 °C) spherulites have bow-tie aspects. At low temperatures (<400 °C) spherulites comprise bundles of radiating fibers.

Lithophysae are in some cases interpreted as spherulites that have a central vug (Ross and Smith, 1961; Mcphie et alii, 1993). They are characteristic products of high-temperature devitrification of coherent silicic glasses and they begin to grow at the early stage in the cooling history. During these phases, the glass is still able to deform plastically. Central vugs vary from circular to star-shaped, and may remain empty or are subsequently filled by mineral such agate or chalcedony (Mcphie et alii, 1993). Lithophysae may reach dimensions of a few tens of decimeters.

Lofgren (1971) distinguished two textural associations among the devitrification products of silicic glasses. The first one is the glassy-stage texture, that consists in a glassy matrix and reflects a rapid cooling and low-temperature hydration of relatively dry magma. The second one is the spherulitic-stage texture, in which former glass recrystallizes to spherulites and micropoikilitic textures. Lofgren (1971) suggested that micropoikilitic textures (or snowflake texture – Anderson, 1969) develops through primary devitrification in glasses with high water content or during slow cooling.

Granophyric texture testifies a prolonged permanence of glass at high temperatures (above Tg) and relatively high load pressure, generally associated with a low cooling rate (Lofgren, 1971).

Basing on the main features described in the different sections of MUI, we recognized 3 main devitrification facies: I) glassy; II) microcrystalline; and III) granophyric.

5.3.1 Main devitrification facies of the MUI

I) Glassy devitrification facies: These textures characterize the basal (in all studied sections) and locally the upper portions of the MUI. They are characterized by well-oriented to slightly folded mm- to micrometric sized glass-shards cut by perlitic fractures (Fig. 5.11-a). In the same level, mm-sized isolated tridimite to cristobalite spherulites (Fig. 5.11-b) and lithophysae (Fig. 5.11-d) are present.

II) Microcrystalline (or micropoikilitic) devitrification facies: Micropoikilitic textures consist of small irregular crystals of quartz that enclose smaller crystals of feldspar (Fig. 5.11-c). Sometimes crystals with reabsorbed rims are present in this texture (Fig. 5.11-e). In the Monte Ulmus Ignimbrite microcrystalline devitrification is ubiquitous (Fig. 5.11-f). In sections thinner than 10-15 m, this facies is present in the central portion of deposits and it represents the greater portion of deposits. Where the deposits are thicker than 10-15 meters, this facies characterizes the gradual passage between the glassy and the granophyric facies.

III) Granophyric devitrification facies: It occurs in the central part of Monte Ulmus Ignimbrites, generally where thickness is greater than 15 meters. It is very well developed in the thick sequences of the Sant'Antioco Island. It consists in a fine, equi-granular quartz and feldspar aggregates in the groundmass associated with rounded oxides and trydimite and crystobalite crystals.
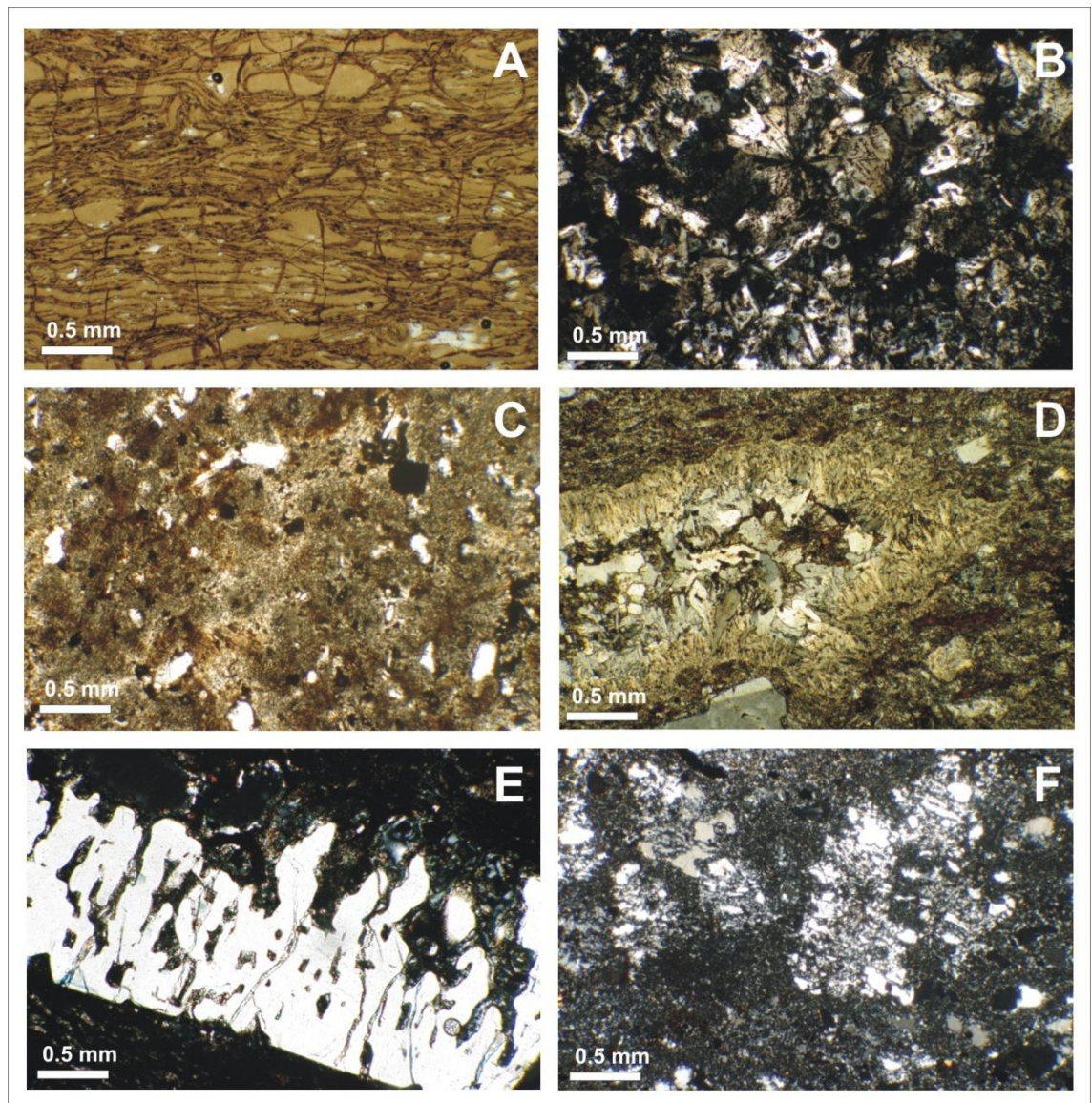
Fig. 5.11: *a) Well oriented glass shards in vitric texture with pervasive perlitic fractures; b) Spherulites in vitric lithofacies; c) Microcrystalline texture in Unit A1; d) Mm-sized axiolitic lithophysae; e) Strongly re-adsorbed crystal edges; f) Well developed micropoikilitic texture*

Facies	Massive vitric tuff (MVT)	Massive with vesicles tuff (MvesT)	Massive isotropic with breccia tuff (MIbrT)	Lineated tuff with parting planes (LPpT)	Eutaxitic poorly sorted tuff (EpsT)	Eutaxitic with degassing pipes tuff (EdpT)	Eutaxitic with xenolitic blocks tuff (ExbT)
Picture							
Internal organization	massive	massive	massive	bedded	graded	bedded	bedded
Texture	isotropic	isotropic to eutaxitic	isotropic	parataxitic lineated	eutaxitic foliated	eutaxitic foliated	eutaxitic foliated
Clast Shape	equant	platy	equant to platy	rod-like	platy	platy	platy
Devetrification facies	vitric - spherulitic	microcristalline	microcristalline	microcristalline to granophyric	microcristalline to vitric	microcristalline	microcristalline
Clast size	ash to lapilli	ash to lapilli	block	ash to lapilli	lapilli to blocks	lapilli to blocks	lapilli to blocks
Degassing structures	micro-porosity	bladed vesicles	-	parting planes / blisters	parting planes	degassing pipes	parting planes
Welding	partially to dense	partially	partially to moderately	partially to dense	partially to moderately	moderatelly	partially to moderately

Facies		Massive vitric tuff (MVT)	Massive with vesicles tuff (MvesT)	Massive isotropic with breccia tuff (MIbrT)	Lineated tuff with parting planes (LPpT)	Eutaxitic poorly sorted tuff (EpsT)	Eutaxitic with degassing pipes tuff (EdpT)	Eutaxitic with xenolitic blocks tuff (ExbT)
Other structures	Macroscale	-	detachment planes	folded spatter	prolate vesicles, blister, ramps, breccia layers, sheet folds, recumbent folds, megafolds, ropy structures, embricated fiamme, tension gashes	folded eutaxitic spatter	folded eutaxitic spatter	-
	Microscale	broken crystals, rotated crystal, well oriented shards, micro-folds, refolded folds, Riedel fractures	rotated fragments (σ, ϕ)	rotated fragments	rotated fragments (ϕ,Θ), refolded folds	rotated fragments, broken crystals, elongated microvesicles, flattened shards and fiamme	-	-

Tab.5.1: *main lithofacies features described in Monte Ulmus Unit*

5.4 Main stratigraphic sections

The different examples of vertical and lateral facies associations, and of their relationships with the main stratigraphic units, are well represented by some selected stratigraphic sections (Fig. 5.1). These sections are also representative of different paleotopographic conditions at deposition, and will be used in the following to discuss the relationships between lithofacies transitions and deformational structures with paleotopography.

5.4.1 Section 14 - Punta Senoglio

The section "Punta Senoglio" (Fig. 5.12), 9.4 meters thick, is situated in the northern sector of the San Pietro Island (Roma 1940 Gauss Boaga Ovest 4335840 N - 1435200 E) and it is interbedded between the Ventrischio Comenditic Unit and the Paringianu Unit (Fig 4.13-a). Section 14 corresponds to a paleotopographic high.

The base of the unit rests on a reddish paleosoil and it is represented by a 5 cm-thick argillified fall deposit. Sub-unit A0, 80 cm thick (Fig. 5.13-b), is a blackish massive vitric tuff (MVT). Symmetric pressure shadows and cm-sized, angular to sub-rounded lithic fragments (Fig. 5.13-c) are locally visible, where the vitric aspect of the deposit is still preserved and not argillified. At the microscale, mm-sized well sorted glass shards are well oriented in accord with the depositional plane. Y-shaped, X-shaped and cuspate glass-shards are locally folded. The deposit shows a glassy facies with a pervasive perlitic fracturing.

Sub-unit A1, divided from the lower sub-unit by a sharp erosive contact, shows two lithofacies. At the base it has a reddish, fine ash MVT lithofacies gradually passing upward to a massive MvesT lithofacies, showing cm-sized oblate vesicles. Matrix is characterized by a microcrystalline devitrification facies.

Sub-unit A2 is characterized at the base by the presence of a layer enriched in cm-sized lithic blocks, typical of the massive isotropic with breccia (MIbrT) lithofacies. A sharp passage separates MIbrT from the overlaying MvesT lithofacies, with cm-sized, slightly prolate to oblate vesicles (Fig. 5.13-d) and cm-size blackish fiammae with rod-like shapes. Sub-rounded lithic fragments and loose crystals are mm-sized. This facies gradually passes upward to an eutaxitic poorly sorted (EpsT) lithofacies with

decimetric-sized blackish platy fiammae. Also, this sub-unit shows a microcrystalline devitrification facies, both in the matrix and into the still recognizable fiammae.

Sub-unit B forms the upper 7 meters of the ignimbrite: the sub-unit is here represented by an EpsT lithofacies, in which up to centimetric juvenile and lithic fragments are normally graded (Fig. 5.13-e). Blackish spatter fragments have mainly platy shapes (Fig. 5.13-g). In the medial portion, sub-unit B passes to a MIbrT lithofacies(Fig. 5.13-f). Metric sub-rounded lithic blocks (Fig. 5.13-h) are chaotically mixed with decimetric sized pumiceous blocks and cm-sized, blackish spatter fragments. Millimeter-sized rounded cavities are present along the entire subunit. Together with the vertical lithofacies variations, this sub-unit also shows vertical variations in the devitrification facies. The lower and central portion have in fact microcrystalline devitrification facies, gradually changing into a vitric with perlitic fractures facies at top.

Unit	Lithofacies	Structures	Sedimentary organization	Texture	Clast Shape	Clast Size	Devetrification facies	Porosity type	Welding degree
B	(EpsT)	lithophysae	Graded bedded	Eutaxitic	Platy		Vitric	With lithophysae	Moderately
	(MlbrT)		Massive	Isotropic	Equant		Microcrystalline	With lithophysae	Partialy
	(EpsT)	lithophysae	Bedded	Eutaxitic	Rod-like		Microcrystalline	With lithophysae	Partialy
	(EpsT)		Bedded	Eutaxitic	Rod-like		Microcrystalline	Bladed vesicles	Partialy
A2	(MvesT)	prolate vesicles	Massive	Isotropic	Rod-like		Microcrystalline	Bladed vesicles	Dense
	(MlbrT)	lithophysae, rotated cryst, prolate vesicle, breccia symmetric pressure shadows	Bedded	Isotropic				Microporosity	Extremely Dense
A1	(MvesT)		Bedded	Eutaxitic			Vitric		
	(MVT)		Massive	Isotropic	Equant				
A0	(MVT)		Massive	Isotropic					

Ash Lapillo Block

Fig. 5.12: Stratigraphic log at section 14 (Punta Senoglio), showing the main features of the deposit
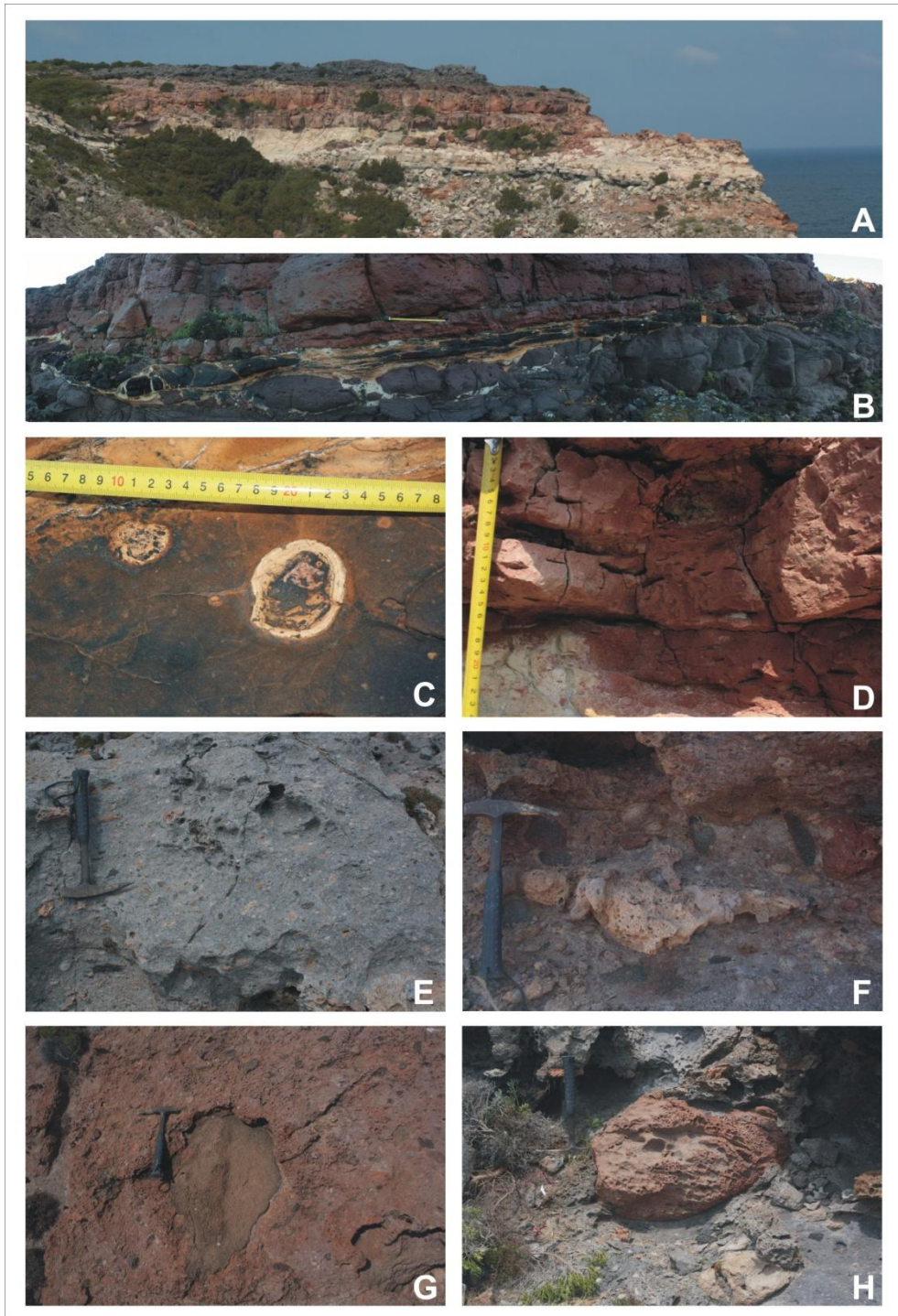
Fig. 5.13: *a)Panoramic view of the Punta Senoglio Section; b)Basal vitrophyre of the MUI; c) centimeter-sized rounded lithic fragments inside the vitrophyre; d) MvesT lithofacies; e)Eutaxitic texture in the unit B; f)Breccia layer; g) Large eutaxitic spatter in the unit B; h) Metric-sized lithic block into the ExbT lithofacies*

5.4.2 Section 12 - Piramide

Section 12 (9.20 m thick - Fig. 5.14) is located in the central area of the San Pietro Island (Roma 1940 Gauss Boaga Ovest 4331970 N - 1438690 E). The section occupies a paleotographic high, and it shows strong lateral variations related with small paleotopographic irregularities.

The basal sub-unit A0 crops out as a totally argillified MVT, present all along the cliff irrespective of paleotopography. It is divided from the upper sub-unit by a sharp contact Sub-unit (A1) overlays the vitrophyre and it is confined inside a small paleodepression, where it thins laterally (Fig. 5.15-a). The first 30 cm of the sub-unit are a reddish MVT facies, overlain by lenses, with a maximum thickness of 15 cm, of MIbr facies. These lenses are characterized by dm-sized (maximum size of 70 cm), sub-rounded lithic blocks of ancient ignimbrites. The remaining portion of the sub-unit A1, 1.5 meters thick, is a reddish, densely welded MVT, with blackish vitric cm-sized eutaxitic fiammae (around 10%) and cm-sized, sub-rounded pumice with rounded vesicles (Fig. 5.15-c). Lithic fragments are generally mm-sized, with morphology varying from angular to slightly rounded.

Sub-unit A2, 1 meter thick, is a MvesT facies, showing cm-sized, oblate vesicles mainly concentrated in the lower half of the sub-unit, gradually becoming sub-rounded to the top. The dm- to cm-sized, blackish, vitric, crystal-poor fiammae (10 - 15 vol.%) have 3:1 to 5:1 AR; cm-sized lithic fragments (around 5 vol.%) are predominantly sub-angular.

Sub-unit B shows a large lithofacies variability. In the first basal 20 centimeters it is an EpsT with a high amount (about 40 vol.%) of dm- to cm-sized blackish, crystal-poor, vitric spatters with low AR (2:1 to 4:1) (Fig. 5.15-b). Cm-sized whitish sub-rounded pumices are present inside this bed. The percentage in dm-sized blackish spatter fragments inside the deposit decreases upward. The middle portion of sub-unit B is a bedded, moderately welded, eutaxitic with xenolitic blocks tuff (ExbT), overlain by a moderately welded, eutaxitic with degassing pipes lithofacies (EdpT). The ExbT facies has platy, metric-sized , microcrystalline foliated ignimbritic blocks with a low amount of fiammae (<5 vol.%) and angular lithics fragments (<5 vol.%). Xenolitic blocks (Fig. 5.15-d) have sub-rounded edges and vitric matrix on the contact with the matrix. Above

these blocks, the EdpT facies is present, with well developed, metric spaced, 1-2 meters long degassing pipes. These vertical structures are clast-supported, with dm-sized blackish crystal-rich spatters covered by yellowish vapor-phases crystals. In the upper portion, sub-unit B passes again into an EpsT facies up to 2 meters thick. It is moderately welded with cm-size, blackish, low AR (2:1 to 4:1) crystal rich spatters, and cm-sized whitish sub-rounded crystal poor pumices.
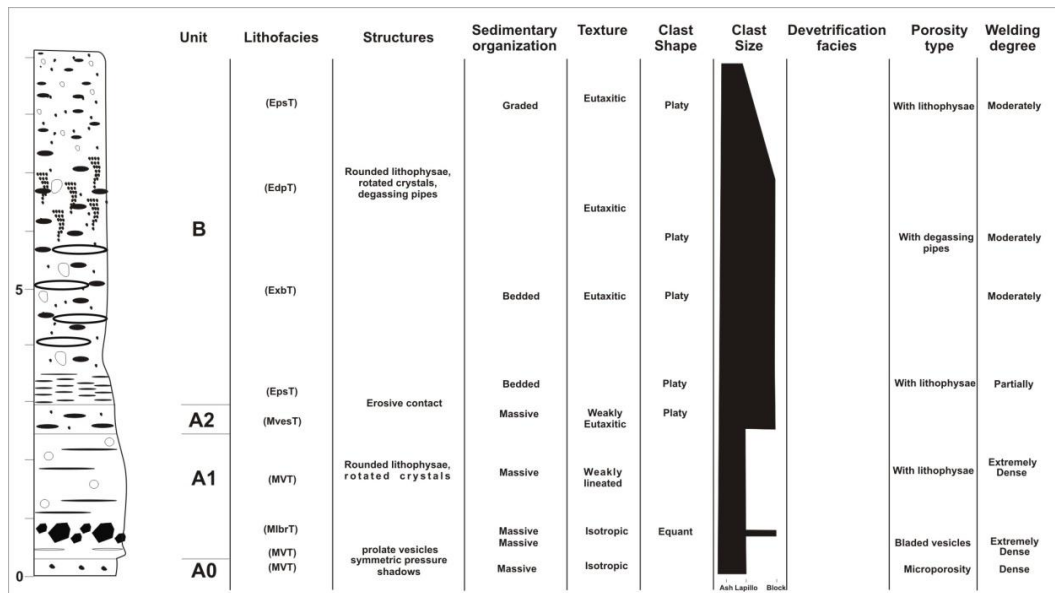
Fig. 5.14: Stratigraphic logs with the main deposits features of section 12 "Piramide"
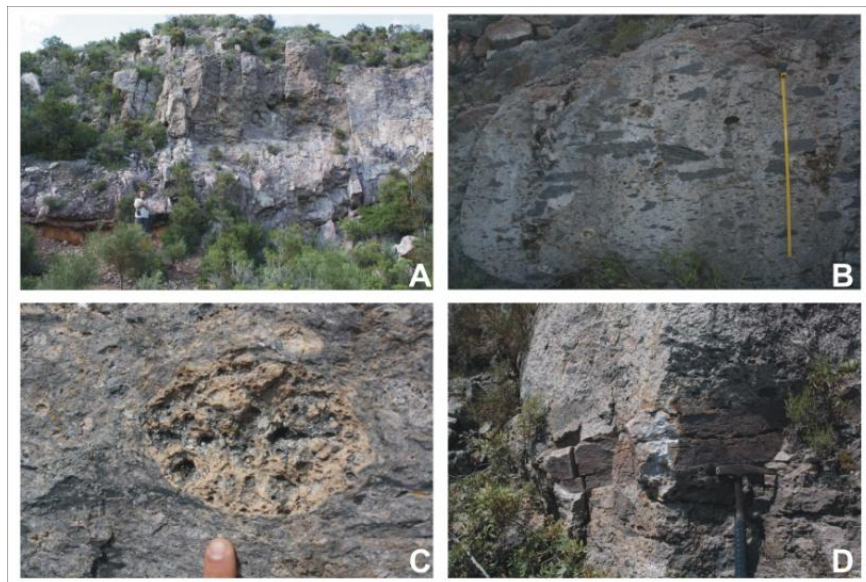
Fig. 5.15: a) lower massive portion of section 12; b) degassing pipes structures; c) Pomice-like fragments with rounded vesicles; d) m-sized enclave

5.4.3 Section 6 - Matzaccara

The Matzaccara section (Fig. 5.16), sited in the Sulcis area (Roma 1940 Gauss Boaga Ovest 4331370 N - 1452220 E), is located in correspondence of a relatively flat area with only smooth topographic slopes.

Although the base of the section is completely argillified, it still preserves a 7 cm thick coarse ash fallout bed with abundant crystals.

Sub-unit A0, 40 cm thick, shows the main features of the MVT facies, although it is nearly completely argillified, it contains vitrophyric layer sub-rounded lithic clasts without any evidence of rotational strain.

Sub-unit A1, 70 cm thick, shows a large lithofacies variability (Fig. 4.17-a) The lower 30 cm show the typical features of the MvesT facies; the deposit is a reddish, weakly lineated, lithic and crystal-poor, moderately welded ignimbrite in a granophyric devitrification facies. Fiammae are blackish, mm-sized and occur at low concentration (<5 vol.%); lithic fragments are mm-sized with angular morphologies. Centimetric vesicles have rod-like shape. The central portion of sub-unit A1 is in the LPpT facies. It is a pinkish, moderately welded ignimbrite, poor in loose crystals and lithic fragments. The top of sub-unit A1 is a 30 cm-thick, lithic poor, spherulitic-rich, moderately welded ignimbrite in the MvesT facies. Cm- to mm-sized oblate vesicles are present inside a matrix with microcrystalline devitrification.

The passage from the sub-unit A1 to sub-unit A2 is marked by a sharp contact. Sub-unit A2, 1.5 m thick, shows the MVT facies at the base, gradually passing upward to a LPpT facies characteristics of the passage from the massive to lineated beds appears to be related to the slope of the paleosurface: on a slope of about 10°, the passage is characterized by a series of detaching planes, while in the presence of flat surfaces the passage between the two lithofacies is represented by a sharp contact (Fig. 5.17-f).The MVT facies is a brownish, crystal and lithic fragments poor, densely welded ignimbrite with granophyric texture. The LPpT facies (Fig. 5.17-c) is a greyish, strongly lineated, lithic poor, partially to densely welded ignimbrite; it is characterized by the presence of ropy structures (Fig. 5.17-b) and sheet folds (Fig. 5.17-e). The spacing between parting planes decrease upward.

The sub-unit B, 4.3 m thick, does not show important vertical variations in lithofacies. From the base to the top it has the main features of the EpsT facies. It is a reddish, eutaxitic, bedded, moderately to partially welded ignimbrite, rich in blackish spatters. Decimetre to centimetre-sized blackish, crystal rich, oblate to slightly rod-like spatters (Fig. 5.17-d) are mixed with cm-sized, sub-angular lithic fragments (mainly from the shuttering of older ignimbrites).
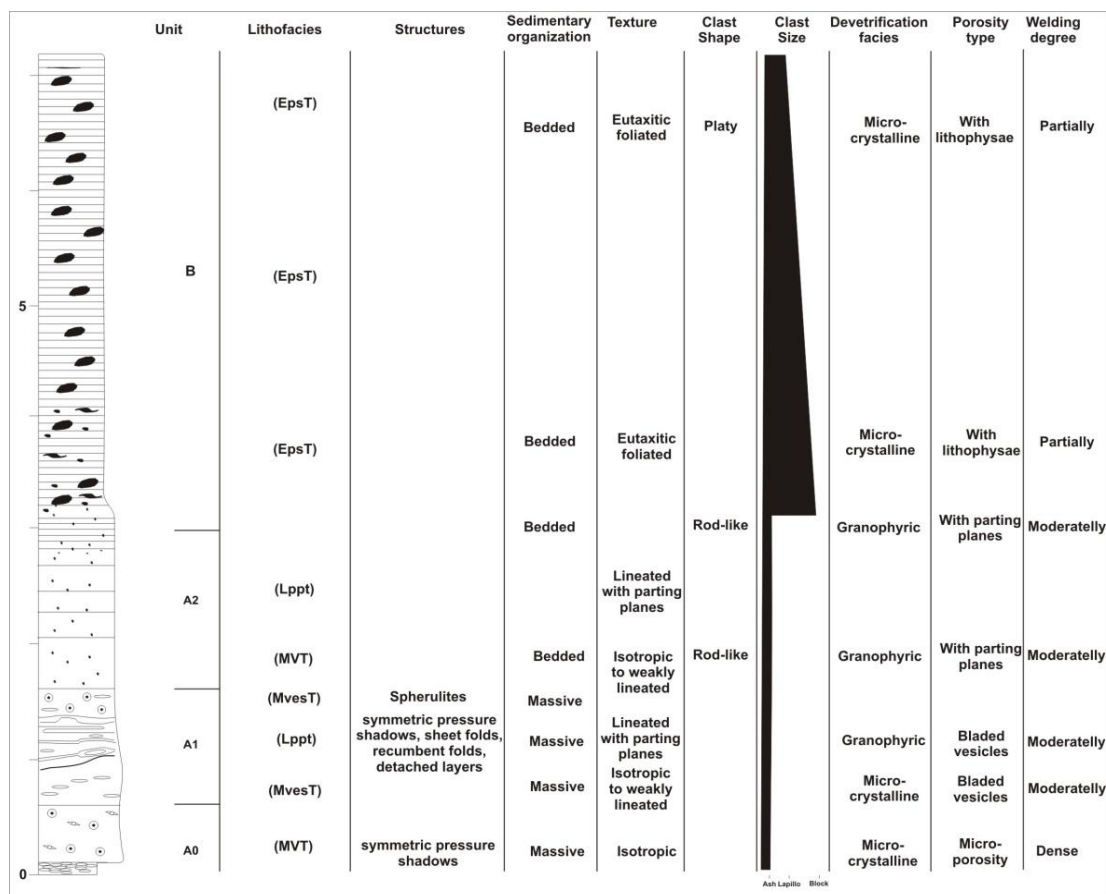
Fig. 5.16: Stratigraphic logs with the main deposits features of section 6 "Matzaccara"
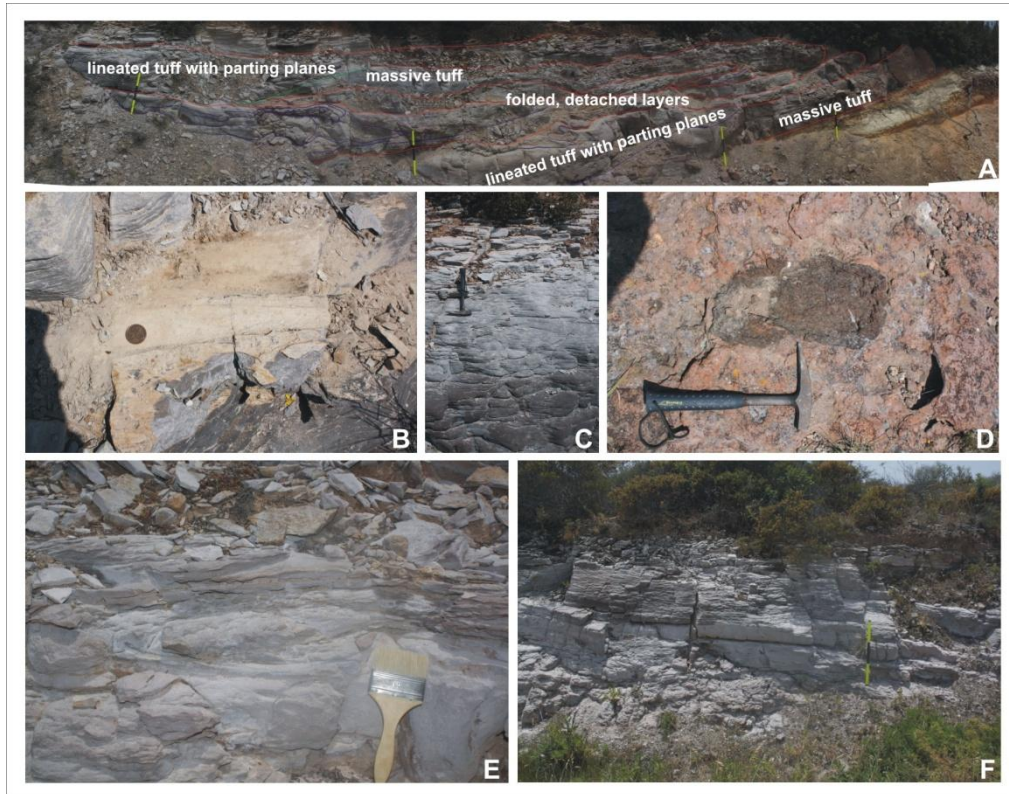
Fig. 5.17: *a) main lithofacies variation in the lower portion of section 6; b)Ropy structures (flow direction is from right to left); c)Strongly lineated portion; d)large eutaxitic spatter fragment; e) Sheet-fold (the flow sense is versus observer); f)sharp contact between massive and lineated lithofacies.*

5.4.4 Section 1-3 Cala Sapone

The Cala Sapone section (Fig. 5.18) is located in the western sector of Sant'Antioco Island (Roma 1940 Gauss Boaga Ovest 4317860 N - 1446850 E). This composite section is visible along the southern side of the bay, in correspondence of a paleo-topographic low.

Sub-unit A0, 8 cm thick, is locally argillified. Where well preserved, it is in the MVT facies, characterized by a moderately welded ash matrix with embedded blackish and whitish vitric fiammae (AR 2:1 - 3:1) and scarce cm-sized angular lithic fragments. The matrix is poorly sorted, with micrometric glass shards and interstitial fine ash. A pervasive perlitic fracturing cross cuts the glass shards.

Sub-unit A1, 7 to 20 m thick, shows a vertical lithofacies variability. It can be divided into a lower MVT facies, 1 m thick, passing gradually upward to a reddish to greyish, crystal poor, densely welded LPpT facies (Fig. 5.19-a). Cm-sized lithic fragments have

angular to slightly rounded edges. The LPpT facies gradually passes from microcrystalline to granophyric devitrification. It is characterized by the presence of a large range of deformational structures, with a gradual passage from fragile (in the lower portion) to ductile structures (into the core of the deposit). From the base to the central portion of stratigraphic sequence we observe rotated fragments (Fig. 5.19-b), embricated fiammae, tension gashes, breccia layers (Fig. 5.19-g), boudinated layers (Fig. 5.19-c), parting planes, ropy structures, sheet joints (Fig. 5.19-f), refolded and sheet-folds, blisters (Fig. 5.19-d), angular unconformities (Fig. 5.19-e), anticlinal structures (Fig. 5.19-i), metric-sized folds (Fig. 5.19-h) and ramps.

Sub-unit A2, 2 m thick, has variable (from sharp to nearly obliterated) contacts with the lower sub-unit A1. It is a brownish, crystal poor, foliated (LPpT) partially to densely welded ignimbrite. Lithic fragments are predominantly angular. Many features of this lithofacies are completely obliterated by a pervasive granophyric devitrification texture.

Sub-unit B, about 5 m thick , is divided by the lower sub-unit A2 by a sharp contact and an angular unconformity. It occurs only in the EpsT facies, as a reddish, spatter-rich, eutaxitic, bedded, moderately welded ignimbrite. Two main types of juvenile fragments are recognized: dm- to cm-sized blackish, crystal-rich, platy to rod-like spatters, and reddish, crystal-poor, platy to slightly rod-like spatters. Cm-sized lithic fragments (5-10 vol.%) are predominantly of older ignimbritic rocks. The lithofacies shows an upward variation in the devitrification facies, from granophyric to microcrystalline to vitric (on the top)
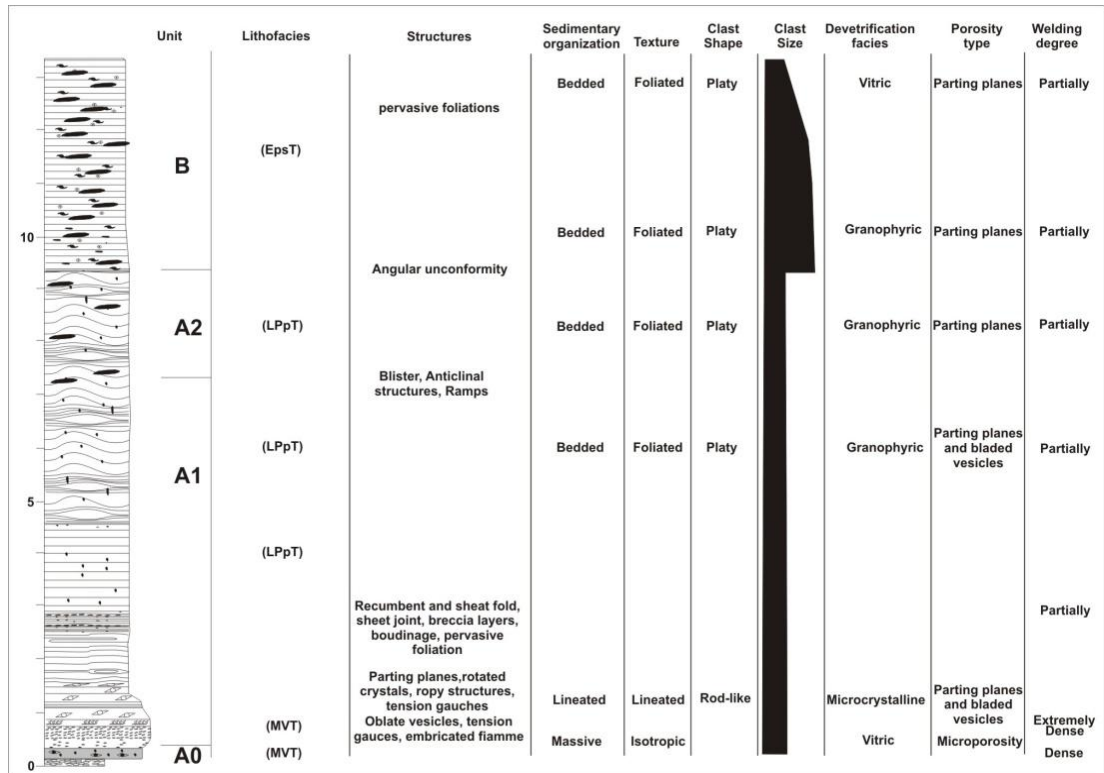
Fig. 5.18: *Stratigraphic logs with the main deposits features of Sect. 1-3 "Cala Sapone"*
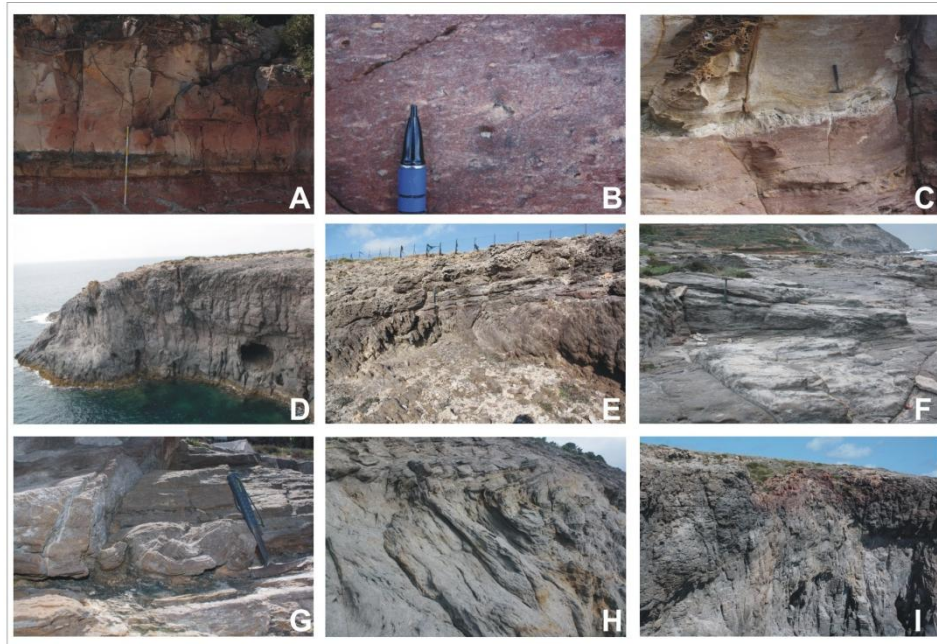
Fig. 5.19: *a)passage from massive to lineated lithofacies at the base of section 1-3 "Cala Sapone"; b)rotated lithic fragment; c) boudinage layer; d)vertical section of blister structures; e) angular unconformities between unit A2 and B; f) sheet joint with fold <1m; g) sequence of breccia layer, refolded folds and laminated layers; h)decametric-size fold; i) diapir-like structure*

5.4.5 Section 29 Mezzaluna

The Mezzaluna bay section (Fig 5.20) (Roma 1940 Gauss Boaga Ovest 4316100 N - 1447200 E) is located in the south-western sector of the Sant'Antioco Island. At this locality, the ignimbrite rests on a 10° sloping paleotopography (Fig. 5.21-a), in correspondence of a passage from a topographic high to a topographic low.

Sub-unit A0, 20 cm thick, is locally totally argillified. Where the deposit preserves the original features, it is a MVT. It is a blackish, vitric, moderately welded ignimbrite with black vitric fiammae and white oblate fiamme. Angular, cm-sized lithic fragments from older ignimbrites are present.

Sub-unit A1, 16 m thick (Fig. 5.21-b), shows a large variability in lithofacies. In the first 60 cm it is a reddish, crystal and lithic-poor, densely welded ignimbrite in the typical MVT facies. The passage from the MVT facies to the upward LPpT facies is gradual. The LPpT facies is a reddish, crystal and lithic-poor, strongly foliated, moderately to densely welded ignimbrite. At the base, the spacing between parting planes is 10-15 cm, while it decreases upward up to 1-2 cm. Deformational structures gradually varies from the base to the top, passing upward, in order, from rotated fragments to embricated fiammae, to tension gashes, to step faults (Fig. 5.21-d), to parting planes interbedded with refolded "plastic" breccia layers (Fig. 5.21-e) and sheet-folds (Fig. 5.21-c) and ramps to finish at the top with angular unconformities. Locally, inside the LPpT facies, massive beds are present, separated from folded layers and brecciated beds by detachments planes (Fig. 5.21-f). The central and upper portions of sub-unit A1, 14 m thick, occur as LPpT facies, but the pervasive granophyric devitrification makes the original textural features only partially recognizable.

Sub-unit A2, 2 m thick, is still present as a gray, blackish, spatter-rich, partially to densely welded ignimbrite in the LPpT facies. The whole sub-unit shows granophyric devitrification.

The top of the stratigraphic sequence is represented by the sub-unit B. It is a EpsT, pervasively foliated tuff, with large, normally graded, platy to rod-like blackish spatters. Devitrification facies varies from microcrystalline to vitric at top.

Unit	Lithofacies	Structures	Sedimentary organization	Texture	Clast Shape	Clast Size	Devetrification facies	Porosity type	Welding degree
B	(EpsT)	Meter-sized fold, pervasive foliation	Graded	Foliated	Platy		Granophyric	Parting planes	Partially
							Granophyric	Parting planes	Partially
A2	(LPpT)		Bedded	Foliated	Platy		Granophyric	Parting planes	Partially
A1	(LPpT)		Bedded	Foliated	Platy		Granophyric	Parting planes	Partially
		Meter-sized fold, pervasive foliation							
	(LPpT)	Pervasive lineation and foliation, sheet-folds, prolate vesicles, parting planes, folds lineation, rod-like docollement, step fault, symmetric pressure shadows	Lineated	Lineated	Rod-like				
			Lineated	Lineated	Rod-like		Granophyric	Bladed vesicles	Dense
	(MVT)		Massive	Isotropic			Vitric	Microporosity	Dense
A0	(MVT)		Massive	Massive			Vitric	Microporosity	Extremely Dense

Fig. 5.20: Stratigraphic logs with the main deposits features of Sect. 29 "Mezzaluna"
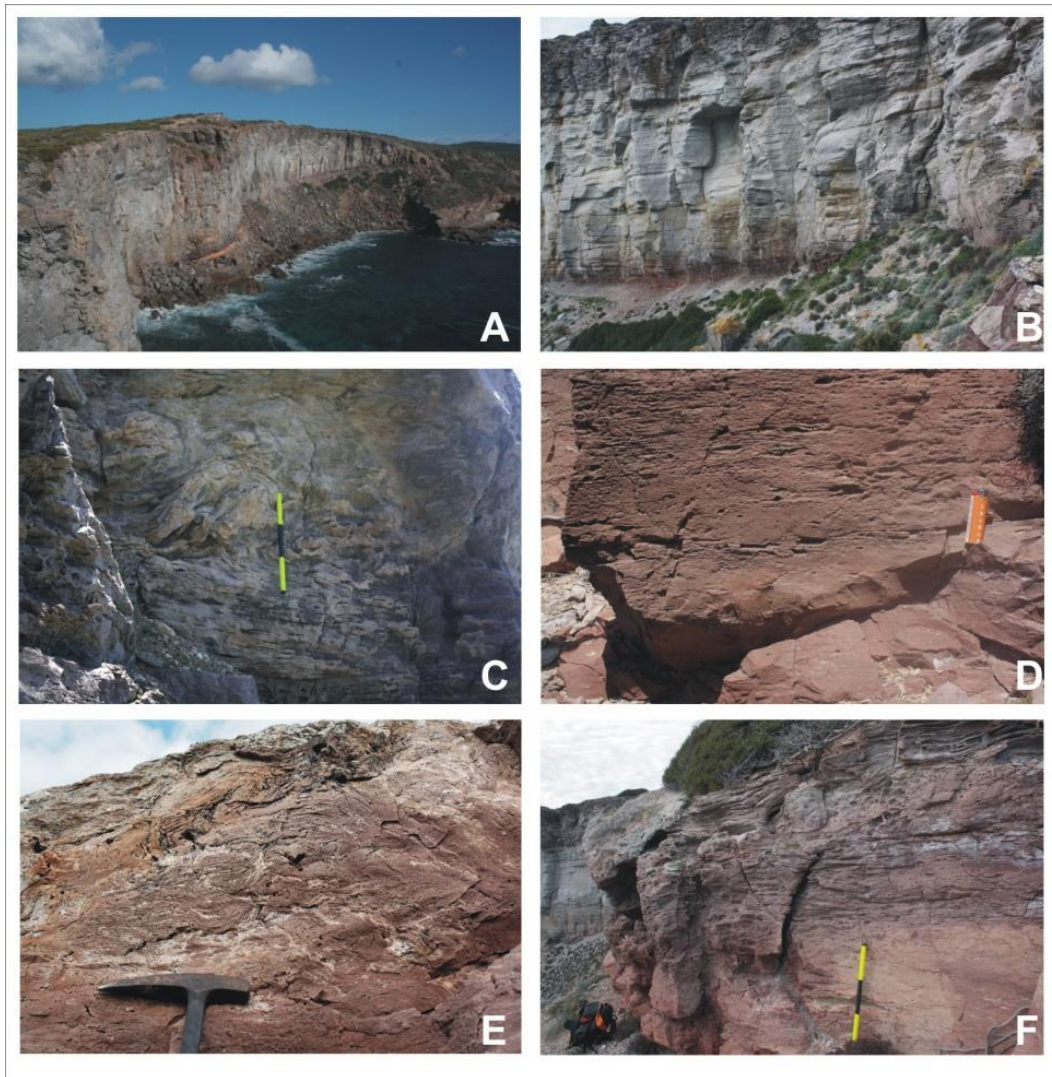
Fig. 5.21: *a) general view of Mezzaluna gulf; b) general view of section 29; c) sheet-fold into lineated lithofacies; d) detachment fractures marked left-ward movement; e) recumbent folds with brecciated layers; f) passage from MvesT to LPpT lithofacies*

5.5 Discussion

5.5.1 Vertical and lateral variations between lithofacies

I) Massive vitric tuff (MVT): This lithofacies generally characterizes the lower portion of the stratigraphic sequence (Fig. 5.22). The dispersal of this lithofacies is not influenced by paleotopography, although it may present lateral thickness variations. MVT varies between 20 cm on topographic highs, to 1 m in topographic lows, while it

shows a quite constant thickness with (inferred) distance from the eruptive area. Vertically, this lithofacies passes gradually both in LPpT facies, mainly in correspondence of topographic lows, and in MvesT facies on topographic highs or in the presence of generally flat conditions. Average dimension of glass shards shows a relationship with distance: from San Pietro to Sant'Antioco, glass shards decrease in size (from millimetric to sub-millimetric) while matrix becomes progressively more abundant respect to glass shards (from glass shards sustained to matrix sustained textures).

Interpretation

The glass shards features and the observed changes in the matrix can be interpreted like a passage from a fine-depleted, rapidly agglutinating basal flow in proximal areas, to a progressively less turbulent cloud more enriched in ashy fraction.

The perlitic fracturing which always affects this lithofacies is possibly be related to processes of glass hydration over a rapidly quenched deposit.

II) Massive with vesicles tuff (MvesT): This lithofacies is present both on paleotopographic highs and in paleotopographic lows. Lateral correlations also evidence an important change in thickness between the two paleotopographic situations (1-2 m-thick on topographic highs and flat conditions and 30 cm thick in topographic lows). In addition, on topographic highs and flat conditions vesicles oblateness is lower than in topographic lows. Average size of vesicles increases upward in the stratigraphic sequence, and it is greater in San Pietro area respect to the Sant'Antioco area.

Interpretation

The presence of vesicles can be interpreted as the result of gas trapping during the emplacement of the deposit, in the presence of syn-eruptive welding processes. The upward increase in vesicles size can be related to the decreasing upward of lithostatic load, on a still plastic layer. In addition the higher percentage of vesicles observed in the San Pietro sections can be interpreted in terms of deposition from a highly inflated cloud and, possibly, of longer times for welding, which allowed a more efficient degassing for the prolonged conditions of high permeability of the deposits. The larger

vesicle oblateness observed in the thinner MvesT facies on the topographic lows suggest a larger welding rate inside the valleys, where vesicle deformation was mainly related to the loading effect of the overlaying, much thicker units. This could also be an indirect indication for the rapid emplacement of the whole ignimbrite.

III) Massive isotropic with breccia tuff (MIbrT): This lithofacies is present in different flow units, generally with thickness of 1-2 meters. The lithofacies is present both in paleotopographic highs and paleotopographic lows, but exclusively in the San Pietro Island. Contacts with the lower and upper lithofacies are gradational. In Sant'Antioco Island and Matzaccara this lithofacies is not present.

Interpretation

The main feature of this lithofacies suggest the proximality respect to the source area (as suggested by the coarseness of the maximum blocks). The sharp contact with the underlying deposits contrasts with the gradual passage to the upper facies, a feature that can be interpreted in terms of a sharp waxing phase followed by a gradual waning phase of the eruption.

IV) Lineated tuff with parting planes tuff(LPpT): This lithofacies shows the greater thickness in topographic lows (up then 14 meters) decreasing to 1-2 m on topographic highs. In topographic lows, the parting planes have a metric spacing, while on topographic highs spacing becomes much more thin, up to centimetric. The passage from the underlying MVT lithofacies is generally gradual.

Interpretation

The gradual passage from the underlying MVT facies suggests continuous sedimentation from a sustained current that gradually becomes more dilute and turbulent. Moreover, the upward change in deformational structures often observed inside topographic lows and highs can be interpreted like a gradual passage from fragile deformation to ductile deformation of deposits.

V) Eutaxitic poorly sorted tuff (EpsT): This lithofacies is mainly distributed on a flat topography, both in San Pietro Island and in Sant'Antioco e Sulcis areas. It is present only at top of sections from both paleotopographic lows and paleotopographic highs. The base of the facies can be irregular, while the top tends to give a flat morphology. In San Pietro Island this facies is characterized by the presence of degassing pipes (EdpT) and large xenolitic blocks (ExbT)

Interpretation

This lithofacies do not shows strong lateral variation in its features. The only differences are the presence in the San Pietro Island of particular structures that show proximity to the source area of these deposits.
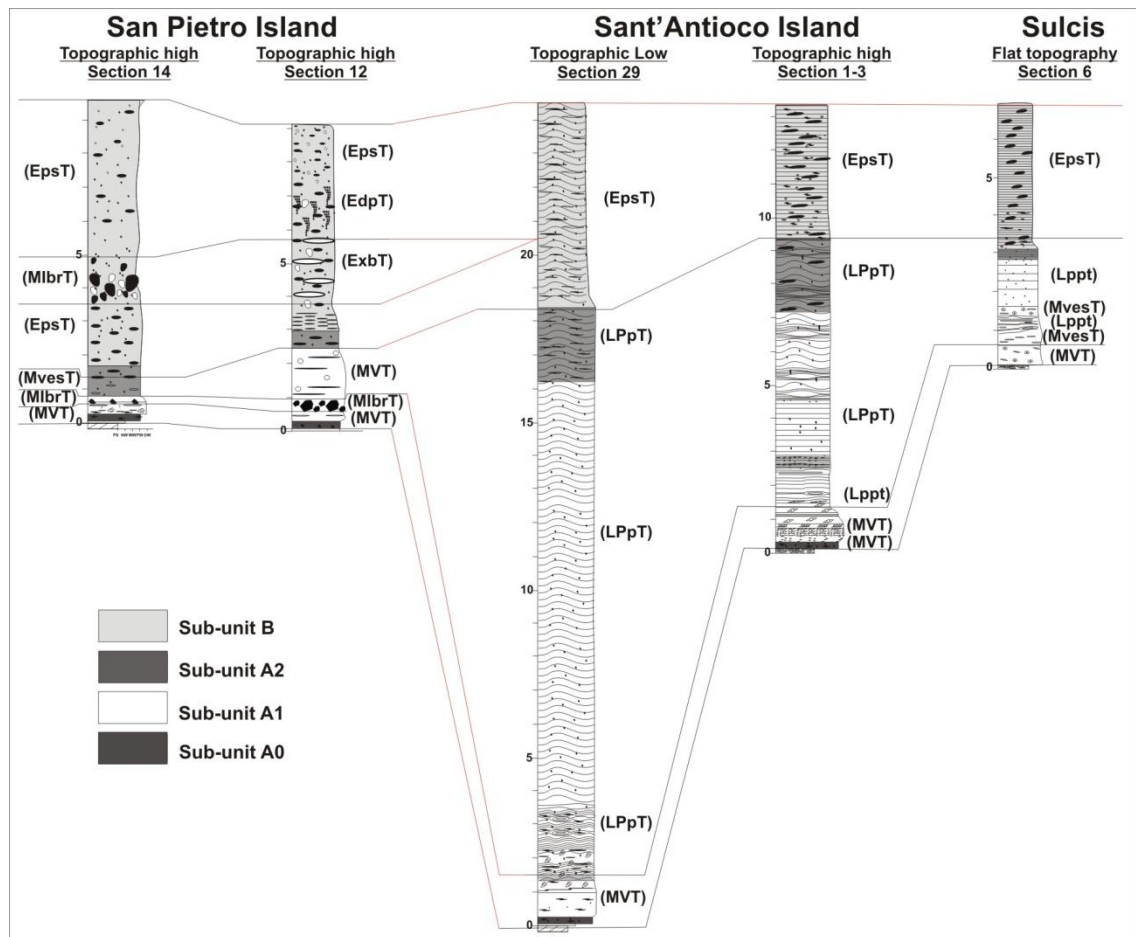
Fig. 5.22: *lateral lithofacies correlations show that LPpT facies have maximum thickness in topographic lows. EpsT facies show a large complexity in proximity of the source area.*

5.5.2 Thickness distribution and pre-emplacement paleotopographic conditions

The paleotopographic conditions were estimated in accord to deposits thickness variations and measured dips of the basal beds of MUI (Fig. 5.23).

MUI on San Pietro Island shows thicknesses lower than 10 m in the area of Punta Senoglio and in the central area of the island. Instead, in the area from the Carloforte village to Punta delle Oche (northern sector of the island) thickness reaches 55 m.

MUI outcrops in the western part of the San Pietro Island were interpreted like high paleotopographic in accord with their low thickness and the absence of rheomorphic facies. The base of unit A0 usually thins, eastward, part from the Punta Senoglio area where MUI was filled between two ancient lava flows. Close to the NW sector of the Carloforte village, the dips of MUI are convergent toward an area where the thickness increases up to 55 m. In addition here MUI had prevalently rheomorphic lithofacies with fold axis coherent with layers dipping. These data suggest the possible presence of an ancient valley, NW-SE oriented, extending from Punta delle Oche toward the Carloforte village.

On the Sant'Antioco Island, MUI generally rests on a gently dipping paleosurface (~10°) and has a thickness ranging from 3 m to 23 m. Most ancient products of the volcanic activity in the Sant'Antioco Island, as the Nuraxi ignimbrite (Pioli et al., 2005) and the previous volcanic deposits, make a relief occupying mainly the eastern-south-eastern sector of the island together with Mesozoic limestone (Lecca et al., 1997). For this reason MUI crops out extensively in the western sector of the island together with the other youngest volcanic products and shows a progressive westward thickening.

The general basal dips of the MUI on Sant'Antioco Island suggest the presence of a westward merging flank of a relief on which the different pyroclastic flow deposited. Here paleotopography was characterized by SW-oriented, gently deeping flanks (~ 10°), with deposits thickness that gradually increase seawards. The morphological features of the western side of Sant'Antioco Island before MUI emplacement were probably similar to the present ones.

In the Sulcis area, MUI shows a roughly constant thickness of about 10 m from Matzaccara to Giba villages (southern sector of Sulcis area), while in the northern sector (eastward respect to the Portoscuso village), ignimbrite has thickness ranges between 45

and 98 m. These data suggest the presence of a wide topographic low, while Matzaccara and Giba areas, where the thickness does not exceed 12 meters, represented a generally flat areas.

After the emplacement of the MUI, the paleotopography in Sulcis and Sant'Antioco e San Pietro islands was generally flat. As a consequence, the following last 4 ignimbrite units were characterized by an overall constant thickness and by well lineated lithofacies. Only locally, small thickness variations occur, related with the presence of poorly escavated paleovalleys.
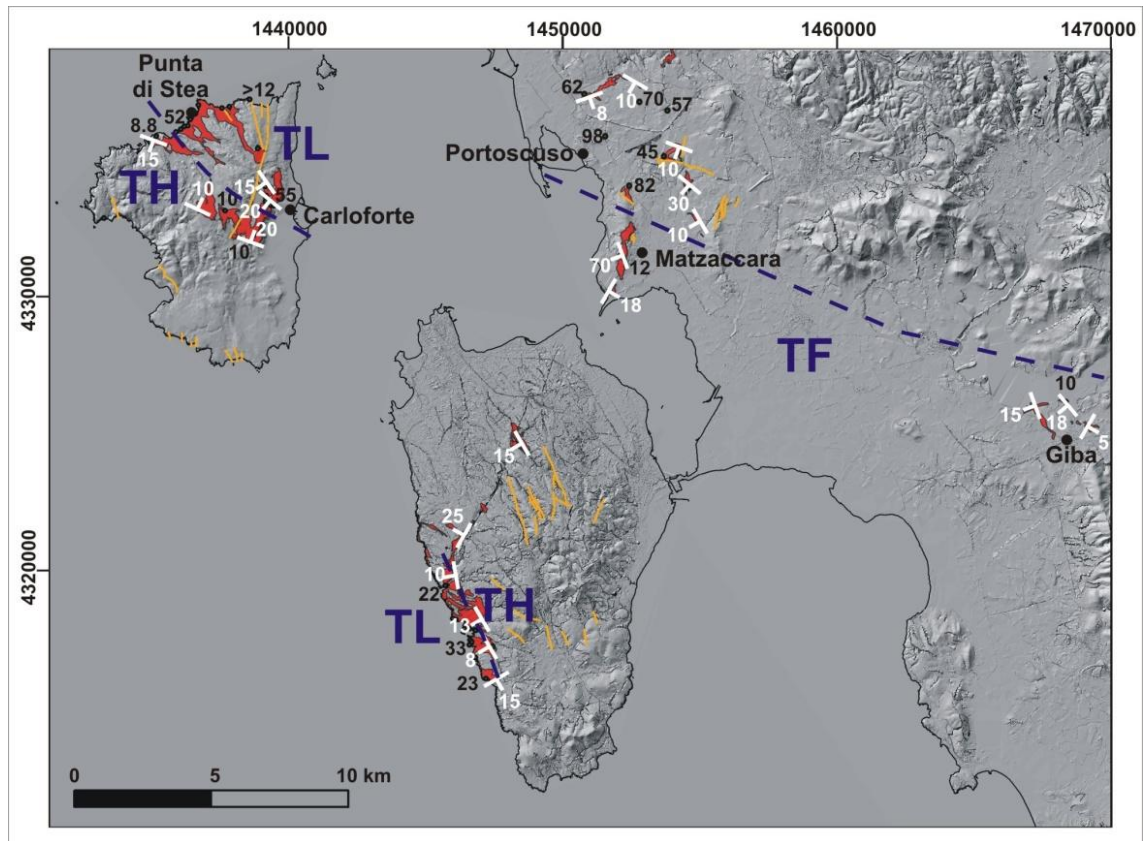
Fig. 5.23: Total thickness (black values expressed in meters) map with measured dips (white values) of the basal beds. Topographic conditions before MUI emplacement are indicated in blue: TH (topographic high), TL (topographic low) and TF (topographic flat)

5.5.3 Source area and flow directions

Source area was determined taking into account the thickness of the basal fall deposits (Fig. 5.24-a) the observed lateral variations in lithofacies and the general flow directions.

Due to the pervasive argillification of pumice and the consequent effects of lithostatic load of the upper ignimbrites reducing their original thickness, data derived from the basal fall-out deposits can be affected by errors. For this reason, data on lateral thickness variation of the fallout deposits were compared with the lithofacies lateral variations, mainly focusing on the grain size of their juvenile and lithic clasts. The coarsest deposit generally crop out in the northern part of the San Pietro Island.

The flow directions were estimated and measured in the field on lineated structures (Fig. 5.24-b), ropy structures (Fig. 5.24-c), embricated fiammae (Fig. 5.24-d) and directions of the major axis of prolate vesicles. These analyses were also performed on some oriented thin-sections, both on lineated lithofacies and on massive lithofacies. The kinematic indicators were considered separately to observe possible discrepancies of strain/flow directions. Field data showed a NW-SE trend of flow directions in the San Pietro Island, direction varying between N110° and N140°, with transport to south-west. In the Sant' Antioco area, the flow directions (N80° to N100°) have a westward oriented transport direction. Finally, in the Sulcis area general trends of transport directions were N120°, NW-oriented.

Taking into account the lateral variations of lithofacies showing proximality in San Pietro Island and the main trends of flow direction, it is possible to place tentatively the source area of the ignimbrite in the sea, in the northern sector of the studied area, in agreement with the possible source area suggested for the Nuraxi Tuff (Pioli and Rosi, 2005). The significance of the apparent opposite flow directions observed between the outcrops of the Sant'Antioco Island and of the Matzaccara area is still not clear. This is possibly due to the fact that the most clear, unequivocal flow indicators were recorded in the basal portion of the ignimbrite, that was possibly locally channelized by pre-existing topographic irregularities, so justifying the observed changes in flow direction.
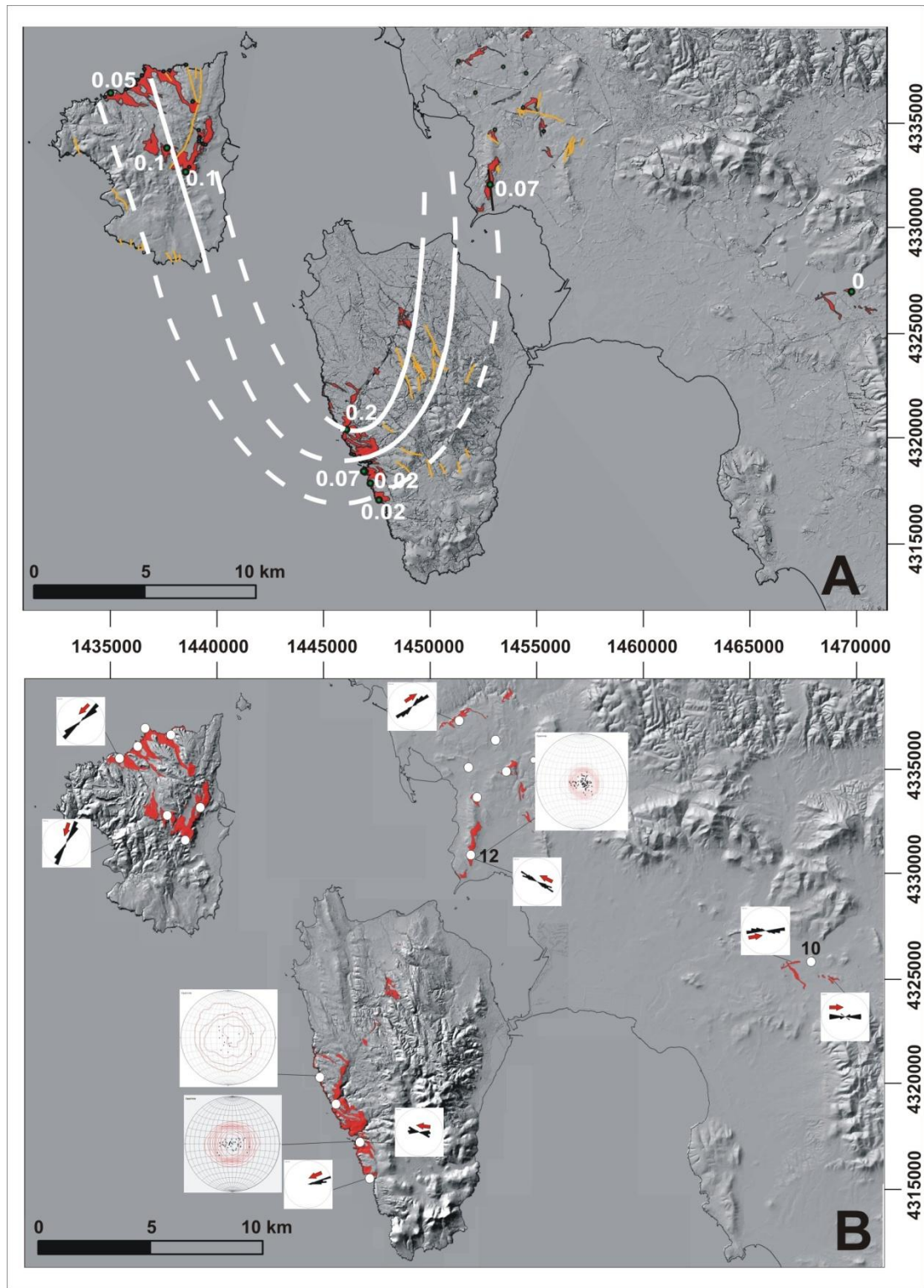
Fig. 5.24: *a)Isopach map of basal fall deposits (thickness in meters); b) Lineation rose diagrams*
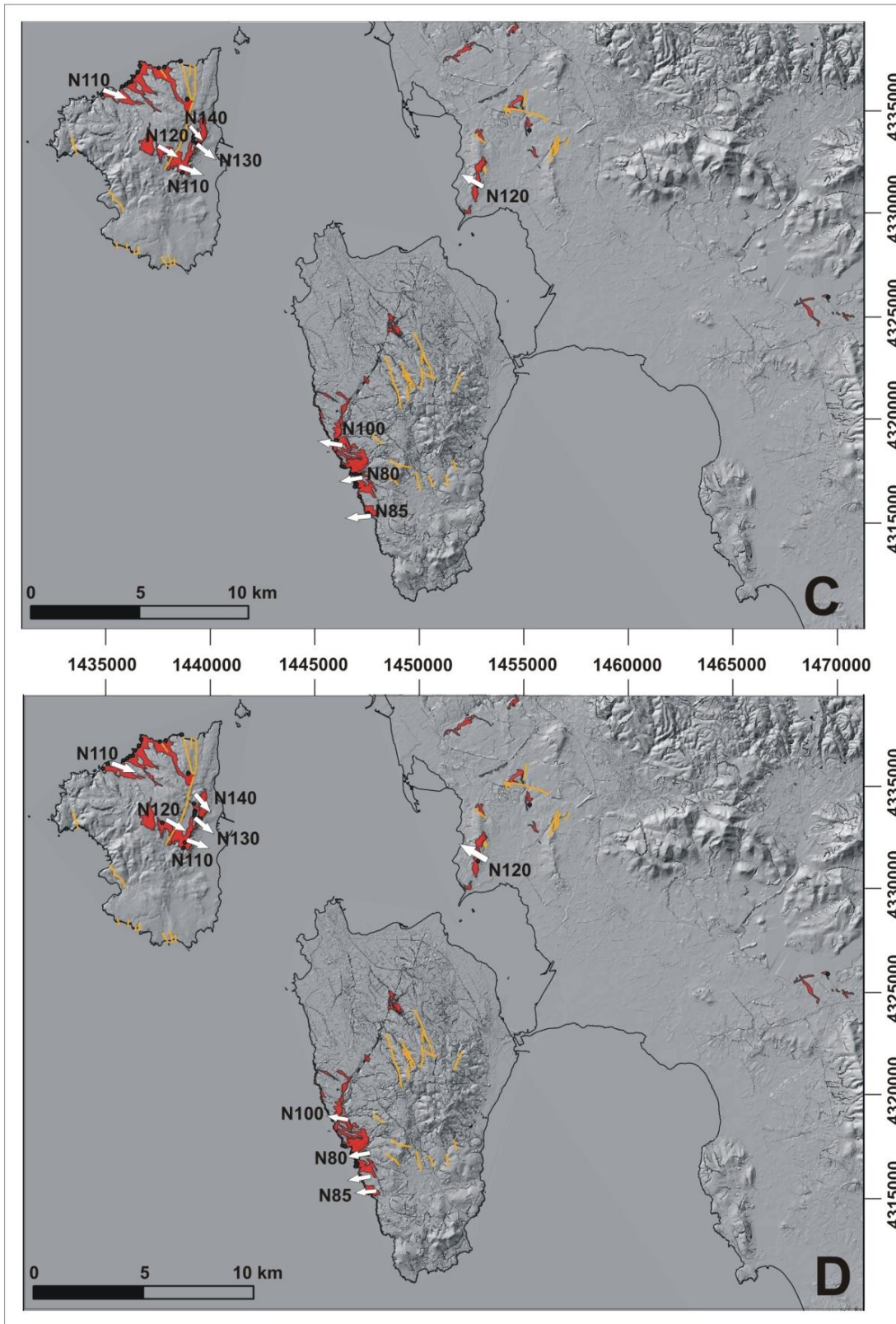
Fig. 5.24: *c) Flow directions in accord with ropy structures; d) Flow directions in accord with embricated fiamme*

5.5.4 Secondary rheomorphism

The post-emplacement, gravity controlled deformation of deposits is here interpreted as related to the re-adjustment of the deposits after the passage of the pyroclastic flows. Different kinds of rheomorphism are observed, which correlate with the affected primary lithofacies total deposits thickness and the cooling rate of the deposits (time elapsed between deposition and cooling below T_g). The main mechanisms that produce rheomorphism are: the gravitational-induced readjustment over topographic slopes, and the deflating process related with the final, post-depositional phase of gas escape from the deposits.

Two main kinds of rheomorphic movements are described: a fragile-ductile rheomorphism and a ductile rheomorphism. The first one is mainly observed on paleotopographic highs, in correspondence of deposits having thickness lower than 10 meters. Conversely, rheomorphism is observed in paleotopographic lows and affects the deposits for the whole thickness.

I) *Fragile-ductile rheomorphism*

This kind of rheomorphism affects those lithofacies located between the cold substratum and the plastic core of the deposits (in paleotopographic depressions) or in the core of the deposits in correspondence of paleotopographic highs, especially in the presence of a paleotopographic slope. Massive and lineated facies are cut by ramp structures, when subdivide the deposits into beds with thickness variable from 40 cm to 1 meter. Inside the single beds, matrix can remain undisturbed or is intensely folded.

On lineated facies, the shear stress is mainly focalized on pre-existing parting planes, with formation of ramp structures, folds <1 m and thin breccia layers. Deformation occurs under different viscosity conditions, as suggested by the alternated presence of breccia facies or of dm-size folds. This different behavior can also be related to variable rates of deformation inside the deposits.

II) *Ductile rheomorphism*

It is generally associated to the inner cores of the deposits, mainly in correspondence of the paleotopographic lows (both in proximal and medial-distal sections), having

thickness >10 meters. Deposits affected by this type of rheomorphism generally show a microcrystalline to granophyric re-crystallizations, due to a permanence at temperature greater than Tg. The main structures related with this kind of rheomorphism are: metric to decametric folds, diapir-like structures, blisters and ramps. Although deposits show ductile behaviour, breccia layers can be formed in the presence of locally high strain rates, mainly close to the basal portions of deposits.

The presence of sub-circular (in map-view and in vertical cross-section) decametric-wide blisters is possibly related to a final, intense degassing phase post dating the main rheomorphic phase

These physical conditions allow the deformation of the deposit under the effect of different forces and processes, represented mainly by gravity (steep paleotopography) and, to a lesser extent, by degassing processes. The general occurence of ductile-style deformation suggests prolonged conditions of high temperature and low viscosity after deposition.

CHAPTER 6

PHYSICAL AND COMPOSITIONAL PROPERTIES OF THE MONTE ULMUS IGNIMBRITE

6.1 Introduction

The MUI is characterized by a large vertical variability in physical, petrographic and chemical features which can give further insights into the dynamics of emplacement processes, cooling processes and the later devitrification and degassing phases, as well as into the relationships between the different conditions of deposition and paleotopography.

6.2 Bulk rock density

Vertical variations of density and porosity can be related, at a first approximation, to the welding processes (in accord with the previous studies of Riehle et al. 1995, 2010 and reference therein) and with the subsequent rheomorphic and degassing processes (Riehle et al., 2010). Vertical variations in density and open porosity were measured on 23 oriented cubic samples, 5 cm side, collected in the most complete stratigraphic sections (sections 6, 14 and 29 - Tab. 6.1; Fig. 6.1). Volume of each specimen was determined geometrically and following the Archimede's principle .

At section 14 (on a paleotopographic relief and the closest to the inferred source area) bulk rock densities values vary from 1747 to 2253 kgm^{-3} in the sub-unit A0, and from 2091 to 2161 kgm^{-3} in all the other sub-units (Tab. 6.1). The MVT facies in sub-unit A0 and A1 has the highest values; density decreases upward passing into the other lithofacies. Conversely, the density profile of sub-unit B shows a general upward increase, with a weak inversion in correspondence of the MIbrT facies (Fig. 6.1).

Componentry (for example the abundance in free crystals) and vesicles oblateness do not show any clear relation with the stratigraphic height and do not suggest the occurrence of depositional breaks (Fig. 6.3). Real densities and apparent densities have similar trends (Fig. 6.2-a). Also, open porosity trends mark the most important stratigraphic breaks (Fig 6.2-b). Open porosity (Tab. 6.1) strongly increases (from 3-4% to 15-16 vol.%) from MVT facies to the LPpT facies.

Tab. 6.1: *Main physical value of cubic samples*

Sample	Stratigraphic height (m)	Lithofacies	Unit	Dry weight (gr)	Volume (cm^3)	Density (kg m^{-3})	Wet weight (gr)	Open porosity (%)
Sect. 14 Punta Senoglio								
MU59	8.20	EpsT	B	298.12	137.92	2161.59	311.01	9.35
MU32	3.90	MlbrT	B	282.04	132.60	2127.00	292.05	7.55
MU31	3.60	EpsT	B	126.99	60.84	2087.28	131.72	7.77
MU30	2.00	EpsT	B	152.44	72.90	2091.08	158.73	8.63
MU26	1.60	MvesT	A2	287.93	135.25	2128.84	300.22	9.09
MU24	0.40	MVT	A1	332.59	154.20	2156.87	344.47	7.70
MU36a	0.25	MVT	A0	213.21	116.50	1830.00	243.65	26.13
MU36b	0.20	MVT	A0	199.53	104.62	1907.19	209.50	9.53
MU36c	0.15	MVT	A0	129.90	57.65	2253.25	136.75	11.88
MU37a	0.10	MVT	A0	91.58	47.25	1938.20	95.27	7.81
MU37b	0.05	MVT	A0	224.48	128.48	1747.20	238.11	10.61
MU37c	0.02	MVT	A0	101.24	54.51	1857.27	108.41	13.15
Sect. 29 Poggio di Mezzaluna								
MU57	22.30	EpsT	B	275.95	128.79	2142.67	293.32	13.49
MU56	19.30	LPpT	B	251.99	131.35	1918.45	273.70	16.53
MU54	9.50	LPpT	A2	262.10	126.25	2076.04	281.28	15.19
MU52	1.50	MVT	A1	309.98	139.26	2225.97	314.34	3.13
MU51	0.70	MVT	A1	316.95	139.26	2276.02	323.67	4.83
MU50	0.30	MVT	A1	320.61	136.59	2347.23	324.58	2.91
Sect. 6 Matzaccara								
MU58	9.00	EpsT	B	258.37	140.61	1837.52	283.31	17.74
MU49	3.00	LPpT	A2	289.17	137.92	2096.70	312.08	16.61
MU3	2.30	LPpT	A1	274.36	135.24	2028.70	297.30	16.96
MU1	1.80	LPpT	A1	289.41	137.90	2098.63	310.12	15.02
MU4	0.60	MvesT	A1	263.72	136.58	1930.91	283.07	14.17

Micro-porosity (porosity only detected by helium pycnometer, obtained from the difference between helium porosity and water porosity) was measured on 48 microsamples, 6 mm side (Tab. 6.2). In total 6 samples were considered and for each samples were prepared 6 cubic specimens. The analyses were made with an accepted standard deviation of 0.005 % (details about the analytical methods are in Appendix).

Micro-porosity varyes from 0.45 vol.% (MVT facies) to 3.46 vol.% in the upper EpsT lithofacies.

The bulk rock density vertical profile of Section 6 (corresponding to a flat area - Fig. 6.1) shows an overall convex shape. Density shows a weak decreasing-increasing trend (from 2028 to 2098 kgm^{-3}) passing from sub-units A2 to B.

At section 29 (corresponding to a paleotopographic low on the Sant'Antioco Island - Fig. 6.1) the density profile shows a simple trend, dominated by a general decrease of density along sub-unit A1 and through A2 (from 2347 to 1918 kgm^{-3}), followed by a density increase on top of sub-unit B (2142 kgm^{-3}, sub-unit B2).

Tab. 6.2: Physical propriety of Section 14 cubic micro-samples

Section 14 : Punta Senoglio

Sample	Stratigraphic height (m)	Unit	Litho-facies	Dry weight (g)	dev.st ±	Wet weight (g)	dev.st ±	Idrostatic weight (g)	dev.st ±	Apparent volume (cm³)	dev.st ±	Real volume (cm³)	dev.st ±
MU59	8.2	B	EpsT	6.55	0.54	6.91	0.48	3.89	0.33	3.08	0.18	2.62	0.33
MU32	3.9	B	MlbrT	8.38	0.79	8.81	0.68	4.95	0.44	3.86	0.25	3.39	0.34
MU31	3.6	B	EpsT	7.43	0.32	7.72	0.33	4.36	0.19	3.36	0.15	2.99	0.13
MU30	2	B	EpsT	9.00	0.76	9.43	0.75	5.37	0.48	4.05	0.28	3.52	0.29
MU26	1.6	A2	MvesT	7.60	0.79	8.01	0.85	4.52	0.49	3.48	0.36	2.97	0.29
MU24	0.4	A1	MVT	6.56	0.80	6.87	0.79	3.92	0.47	2.95	0.32	2.61	0.33
MU36	0.2	A0	MVT	8.44	1.34	8.71	1.36	4.79	0.77	3.92	0.60	3.57	0.58
MU37	0.05	A0	MVT	7.83	0.51	8.25	0.53	4.43	0.31	3.79	0.25	3.37	0.25

Sample	Stratigraphic height (m)	Apparent - Real volume (cm³)	dev.st ±	Real density (kg/m³)	dev.st ±	Apparent density (kg/m³)	dev.st ±	Open porosity (Helium) (%)	dev.st ±	Open porosity (Water) (%)	dev.st ±	Micro-porosity (%)	dev.st ±
MU59	8.2	0.51	0.23	2527	196	2167	110	16.2	8.0	14.2	3.1	3.5	4.9
MU32	3.9	0.50	0.13	2492	29	2164	87	12.8	4.3	11.1	4.3	1.7	0.5
MU31	3.6	0.37	0.03	2510	16	2223	17	11.0	0.5	9.1	0.4	1.9	0.7
MU30	2	0.56	0.05	2547	124	2194	45	13.7	1.5	11.7	1.2	2.5	0.8
MU26	1.6	0.52	0.08	2548	19	2181	25	14.9	1.1	11.5	1.2	2.8	1.0
MU24	0.4	0.36	0.03	2531	14	2226	47	11.8	2.2	10.9	2.5	0.8	0.5
MU36	0.2	0.30	0.05	2366	15	2180	25	8.2	1.2	6.5	0.7	1.5	0.8
MU37	0.05	0.47	0.16	2323	27	2095	72	12.7	3.8	8.6	2.8	0.5	2.4
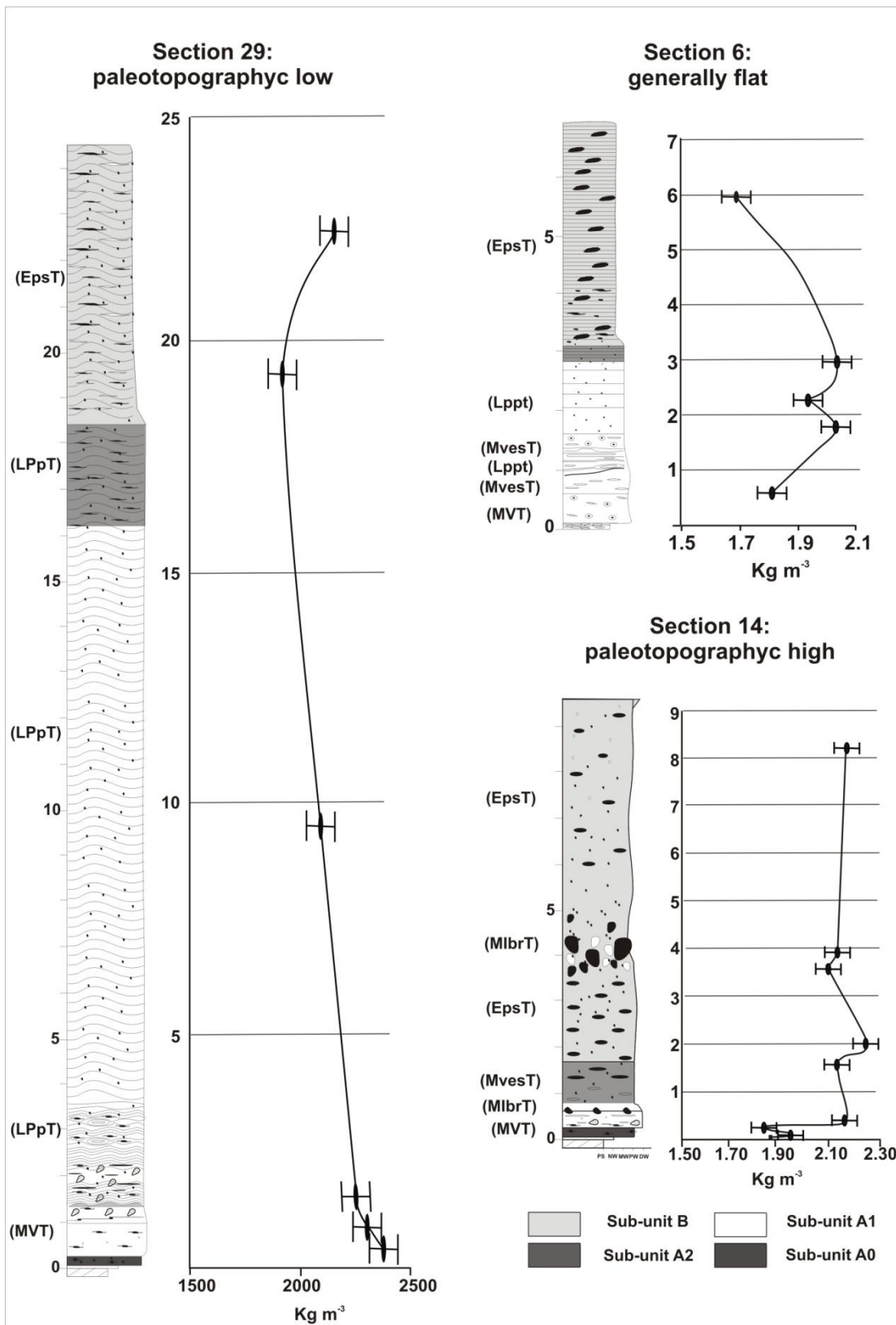
Fig. 6.1: *Bulk rock density values in the three reference sections (mod. Mulas et al., 2011*

Interpretation

According to Riehle et al. (2010), welding processes, rheomorphic structures, secondary vesiculation and thickness can influence the values of bulk rock densities in different ways:

- On paleotopographic highs (sect. 14), the density profile well marks the stratigraphic units recognized in the field. The section appears to be characterized by the lack of rheomorphic structures and by a low welding degree (varying from incipiently to moderately welded, except for the first centimeters of the basal MVT facies). The vertical variation of bulk rock density can be easily correlated with the welding profile.

- On generally flat paleotopographic conditions (in the absence of large depressions; section 6) the density profile shows the classical convex, increasing-decreasing upward trend related with the welding process of a simple flow unit. Only where the deposit is marked by pervasive parting planes, bulk density values have a larger variability (although remaining on high values), related to the local increasing of voids.

- In large paleo-valleys (es. sect. 29) the density profile has a decreasing to increasing upward trend (Mulas et al., 2011). In these paleotopographic conditions, the ignimbrite is characterized by rheomorphic structures and devitrification facies that testify a prolonged permanence above the Tg temperature of the very thick body of the deposit. This trend, according with Schmincke (1974) and Branney and Kokelaar (1992), could suggest the occurrence of vesiculation after emplacement, driven by deformation associated with local decompression of the still hot tuff. In this case density does not mirror welding intensity. Rheomorphism and the related secondary vesiculation process affected mainly the LPpT lithofacies, more prone to deform along the thinly spaced parting planes, resulting in an increase in open porosity respect to the basal non-rheomorphic and densely welded lithofacies.
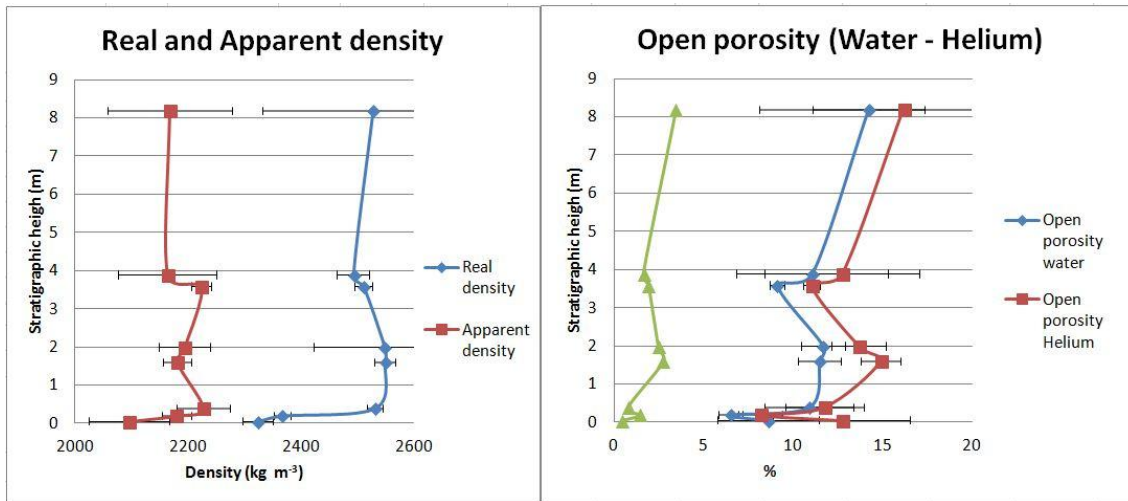
Fig. 6.2: *Vertical trend of the main physical features at section 14*
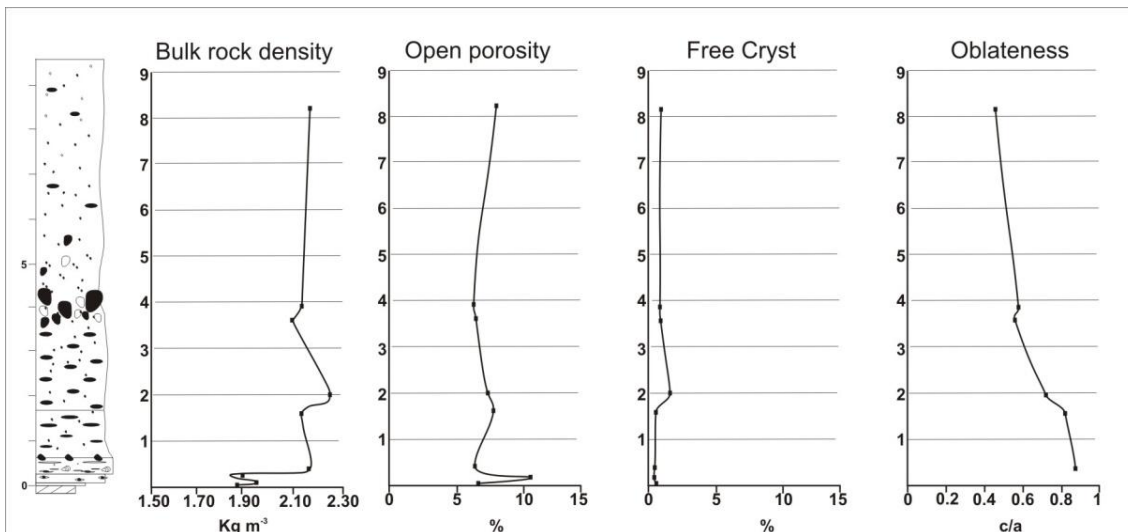
Fig. 6.3: *main vertical physical features variations in section 14 - Punta Senoglio. Oblateness is the major/minor fiammae axis length ratio*

6.3 Ultrasonic velocity

The ultrasonic pulse velocity analysis permits to evaluate the presence of cracks or other planar to local anisotropies (Naik et al., 2002) in a rock specimen. The ultrasonic velocity values can be influenced by different factors: crystal and clast abundance, porosity, permeability.

Only few authors have used this technique on welded ignimbrites. Rodriguez-Losada et al. (2007) made a geotechnical characterization using this technique on trachytic to phonolitic samples from Arico Area (Tenerife Island) and Arucas (Gran Canaria Island). Velocity was measured parallel to the eutaxitic textures (values between 3.182 and 4.342 kms^{-1}) and perpendicular to the eutaxitic textures (2.900 - 4.148 kms^{-1}). Binal (2009) made a geotechnical characterization of Cappadocian moderately welded ignimbrite (average apparent porosity 25%) using ultrasonic waves. In his work, the rock velocity values range between 1.970 and 3.560 kms^{-1}.

The MUI rock specimens were cut into 5 cm side oriented cubes, with two sides parallel to the foliation planes and one side parallel to the flow direction, mainly reconstructed by the direction of elongation of fiammae and vesicles. The analyses were made by direct transmission geometry (transducers on opposite sample faces) using a 150 KHz pulse generator. Samples were put inside a home-made support to standardize measurements, taking note of the time of the first wave arrival (details are in Appendix). Direction X was taken parallel to the flow direction and to the foliation planes; direction Y normal to the flow directions and parallel to the foliations planes; "Z" is the direction normal to the foliation planes and the flow direction (Fig. 6.4).
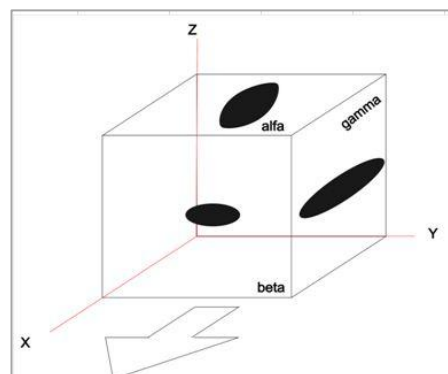
Fig. 6.4: *Main direction on cubic samples used for analyses*

Ultrasonic velocity on MUI samples ranges between 1.797 and 4.337 kms^{-1}. Higher velocity were measured along the direction X: 4.3 kms^{-1} for MVT facies and 3.5 - 3.6 kms^{-1} in MvesT, EpsT and LPpT facies. Conversely, normally to the foliation planes (z-direction), values generally decrease with lower values of 1.79 kms^{-1} on LPpT lithofacies, where ultrasonic waves usually intercept well developed parting planes.

MVT lithofacies shows velocity along z-direction of 3.8 kms^{-1} while MvesT have maximum value of 3.2 kms^{-1}. Velocity ratios between the main directions have values ranging from 0.6 to 1.1. In MvesT, Z/X and Y/X ratios is 0.8 while Y/Z ratios is ~1.

In EpsT and LPpT lithofacies ranging between 2.2 and 3.2 kms^{-1}. The Z/X and Z/Y ratios range from 0.6 to 0.8 while Y/X ratio is ~1.

The elastic modulus (Young's modulus - see Appendix) is the ratio between the uniaxial stress over the uniaxial strain and it is used to make mechanical characterization of materials. It was calculated through the following relation:

$$E = V^2 \rho \ 1 + \mu(1-2\mu)(1-\mu)$$

where:

      V = Velocity

      ρ = Density

      μ = Poisson ratio (0.15 for welded ignimbrite; Rodriguez-Lasada et al., 2009)

This modulus is not equal in all directions if the material is anisotropic, as welded ignimbrites, and it permits to recognize the presence of anisotropies inside the materials. MUI ultrasonic data show a good correlation between Young's modulus and the velocity along different directions, taking in account the different lithofacies (Fig. 6.5). The lithofacies characterized by pervasive planar anisotropies (LPpT and EpsT) showed the lowest values, while MVT lithofacies have the greater ones.

6.3.1 Vertical variations

In Sez.14 (Fig. 6.6) the vertical variation of velocity along the three main directions well marks all the stratigraphic breaks and the lithofacies changes (from MvesT to EpsT). In Sect. 6 (Fig. 6.7) a quick decrease in ultrasonic velocity marks the onset of the lithofacies characterized by largely spaced parting planes; velocity values in this lithofacies are also characterized by the wider variability. In this section, also the Z/X

velocity ratio has a large variability. Where parting planes are cm-spaced, this ratio is 0.8 while where parting planes are mm-spaced this ratio decreases until 0.6. Conversely, in sections where rheomorphic processes are well developed (Sect. 29 - Fig. 6.8), the general trends of ultrasonic velocity follow the bulk rock density trends. The velocity along the main directions and Young's modulus ratios were compared with the open porosity values. Generally, X/Y velocity ratios show the lower values respect the other two ratios (Tab. 6.5). Taking into account the three main lithofacies (MVT, LPpT and EpsT), three main groups of porosity values were recognized (Fig. 6.9). EPST and MVT are present into the first one (7 to 11 %). All samples of LPpT and the part of the EPST (14 - 17%) fall in the second group. Finally, one MVT sample lays in the range with open porosity higher than 20%. Velocity ratios data show two main trends. X/Y velocity ratio are constant with the change of porosity, while the X/Z and Z/Y velocity ratios increase with increasing open posorisity (Fig 6.9).

Interpretation

The ultrasonic velocity method can locate planar or local anisotropies inside the rock samples. The slower velocity along Z-direction and the velocity ratio in LPpt (X/Y~1 and Z/X<<1) confirmed this hypothesis. In the case of foliated lithofacies, the first ultrasonic wave along X- and Y-direction do not intercept the planar anisotropies but it pass into the massive matrix portions between parting planes. Obviously for the same reason in MVT the ultrasonic velocity are highest (and nearly isotropic) in all directions. The similar trend of the velocities along the three main directions in MVT lithofacies can be related to the fine and poorly variable grain size of the matrix, nad to the isotropic distribution of voids and components along the three main directions.

In the analyses, the frequency chosen is in fact not able to mark anisotropy smaller than about 2 cm (like isolated small vesicles). Only where porosity is higher than 10%, the presence and spatial and shape distribution of vesicles and their shape become influential. This feature permits to distinguish MVT lithofacies from MvesT to EpsT and LPpt lithofacies. In the case of sect. 14 (Fig. 6.6) in the portion between 2 and 4 meters from the base, the sharp decrease in ultrasonic velocity trends along the three directions records the passage from MTV to MvesT lithofacies, due to an increase of voids inside the sample. The slightly-oblate vesicle shapes (X≈Y>Z) could justify the

small difference of velocities between the X and Y-directions. The X/Y ratio ~1 confirmed that the void distribution along the two directions is quite similar. Conversely, where the X/Y ratio is greater than 1, we suggest that this is related to the slightly prolate shape of vesicles. It is interesting to note that the lower velocities are not along the major axis (X) but in the normal directions. Taking into account a random distribution of prolate vesicles on the sedimentation plane, this feature can be interpreted like due to the statistically higher probability of long, uninterrupted wave paths along the elongation direction. Conversely, along the Y-direction, ultrasonic wave paths statistically intercept a larger number of elongated, transversally oriented voids. The anomalous value of sample MU51 (MVT lithofacies) is possibly due to the presence of altered lithic fragments inside the cubic specimen.

Tab. 6.3: *General and material features and Average velocity of ultrasonic waves*

Sample	Unit	Stratigraphic Height (m)	Sedimentological features			Physical features			Ultrasonic velocity			
			Fiamme structure	Crystallization Facies	Lithofacies	Apparent density	Open porosity	Picnometer density	Z	X	Y	Average velocity
						(kg m^{-3})	(%)	(kg m^{-3})	(km/sec)	(km/sec)	(km/sec)	(km/sec)
Section 14												
MU59	B	8.2	Eutaxitic	Microcrystalline	EpsT	2161.6	9.35	2456.6	2.436	2.836	2.770	2.681
MU32	B	3.9	Eutaxitic	Microcrystalline	MlbrT	2127.0	7.55	2530.9	3.109	3.521	3.350	3.327
MU31	B	3.6	Eutaxitic	Microcrystalline	EpsT	2087.3	7.77	2513.2	3.127	3.409	3.112	3.216
MU30	B	2	Parataxitic	Microcrystalline	EpsT	2091.1	8.63	2569.0	2.275	2.260	2.502	2.346
MU26	A2	1.6	Parataxitic	Microcrystalline	MvesT	2128.8	9.09	2581.1	3.200	3.559	3.182	3.314
MU24	A1	0.4	Parataxitic	Microcrystalline	MVT	2156.9	7.70	2563.1	3.748	3.719	3.777	3.748
MU36a	A0	0.25	Eutaxitic	Vitric	MVT	1830.0	26.13	2345.9	3.844	4.337	3.753	3.978
MU37b	A0	0.05	Eutaxitic	Vitric	MVT	1747.2	10.61	2345.9	3.638	4.041	3.883	3.854
Section 29												
MU57	B	22.3	Parataxitic	Microcrystalline	EpsT	2142.7	13.49	-	3.394	3.477	3.576	3.482
MU56	B	19.3	Eutaxitic	Granophyric	EpsT	1918.5	16.53	-	2.695	3.055	2.871	2.874
MU54	A2	9.5	Eutaxitic	Granophyric	LPpT	2076.0	15.19	-	2.719	3.382	3.148	3.083
MU52	A1	1.5	Parataxitic	Microcrystalline	LPpT	2226.0	3.13	-	3.280	3.461	3.550	3.430
MU51	A1	0.7	Parataxitic	Microcrystalline	MVT	2276.0	4.83	-	2.476	4.107	4.250	3.611
MU50	A1	0.3	Parataxitic	Microcrystalline	MVT	2347.2	2.91	-	3.868	4.353	4.284	4.168
Section 6												
MU58	B	9	Eutaxitic	Microcrystalline	EpsT	1837.5	17.74	-	2.474	2.735	2.900	2.703
MU49	A2	3	Parataxitic	Granophyric	LPpT	2096.7	16.61	-	1.797	2.632	2.537	2.322
MU3	A1	2.3	Parataxitic	Granophyric	LPpT	2028.7	16.96	-	1.865	2.485	2.792	2.381
MU1	A1	1.8	Parataxitic	Granophyric	LPpT	2098.6	15.02	-	2.430	2.936	2.803	2.723
MU4	A1	0.6	Parataxitic	Microcrystalline	MvesT	1930.9	14.17	-	2.309	3.161	3.014	2.828

Tab. 6.4: *Speed ratio and Young's modulus on the three main directions*

Sample	Unit	Lithofacies	Speed ratios						Young's modulus				Young's modulus Ratio		
			X/Z	X/Y	Y/Z	Z/media	X/media	Y/media	dynamic Z	dynamic X	dynamic Y	n	X/Z	X/Y	Y/Z
Section 14															
MU59	B	EpsT	1.164	1.024	1.137	0.909	1.058	1.033	12148	16465	15708	0.15	1.36	1.05	1.29
MU32	B	MlbrT	1.133	1.051	1.078	0.935	1.058	1.007	19471	24973	22607	0.15	1.28	1.10	1.16
MU31	B	EpsT	1.090	1.095	0.995	0.972	1.060	0.968	19329	22973	19144	0.15	1.19	1.20	0.99
MU30	B	EpsT	0.993	0.903	1.100	0.970	0.963	1.067	10250	10115	12397	0.15	0.99	0.82	1.21
MU26	A2	MvesT	1.112	1.118	0.994	0.966	1.074	0.960	20645	25537	20414	0.15	1.24	1.25	0.99
MU24	A1	MVT	0.992	0.985	1.008	1.000	0.992	1.008	28695	28252	29140	0.15	0.98	0.97	1.02
MU36a	A0	MVT	1.128	1.156	0.976	0.966	1.090	0.943	25609	32599	24411	0.15	1.27	1.34	0.95
MU37b	A0	MVT	1.111	1.041	1.067	0.944	1.049	1.008	21900	27021	24949	0.15	1.23	1.08	1.14
Section 29															
MU57	B	EpsT	1.024	0.972	1.054	0.975	0.998	1.027	23375	24533	25949	0.15	1.05	0.95	1.11
MU56	B	EpsT	1.134	1.064	1.065	0.938	1.063	0.999	13196	16957	14976	0.15	1.29	1.13	1.13
MU54	A2	LPpT	1.244	1.074	1.158	0.882	1.097	1.021	14536	22488	19484	0.15	1.55	1.15	1.34
MU52	A1	LPpT	1.055	0.975	1.082	0.956	1.009	1.035	22680	25252	26568	0.15	1.11	0.95	1.17
MU51	A1	MVT	1.659	0.966	1.716	0.686	1.137	1.177	13215	36358	38934	0.15	2.75	0.93	2.95
MU50	A1	MVT	1.125	1.016	1.108	0.928	1.044	1.028	33259	42122	40797	0.15	1.27	1.03	1.23
Section 6															
MU58	B	EpsT	1.105	0.943	1.172	0.915	1.012	1.073	10651	13017	14635	0.15	1.22	0.89	1.37
MU49	A2	LPpT	1.465	1.037	1.412	0.774	1.134	1.093	6412	13756	12781	0.15	2.15	1.08	1.99
MU3	A1	LPpT	1.332	0.890	1.497	0.783	1.044	1.173	6683	11864	14977	0.15	1.78	0.79	2.24
MU1	A1	LPpT	1.208	1.047	1.153	0.892	1.078	1.029	11736	17133	15616	0.15	1.46	1.10	1.33
MU4	A1	MvesT	1.369	1.049	1.305	0.816	1.118	1.066	9750	18272	16612	0.15	1.87	1.10	1.70
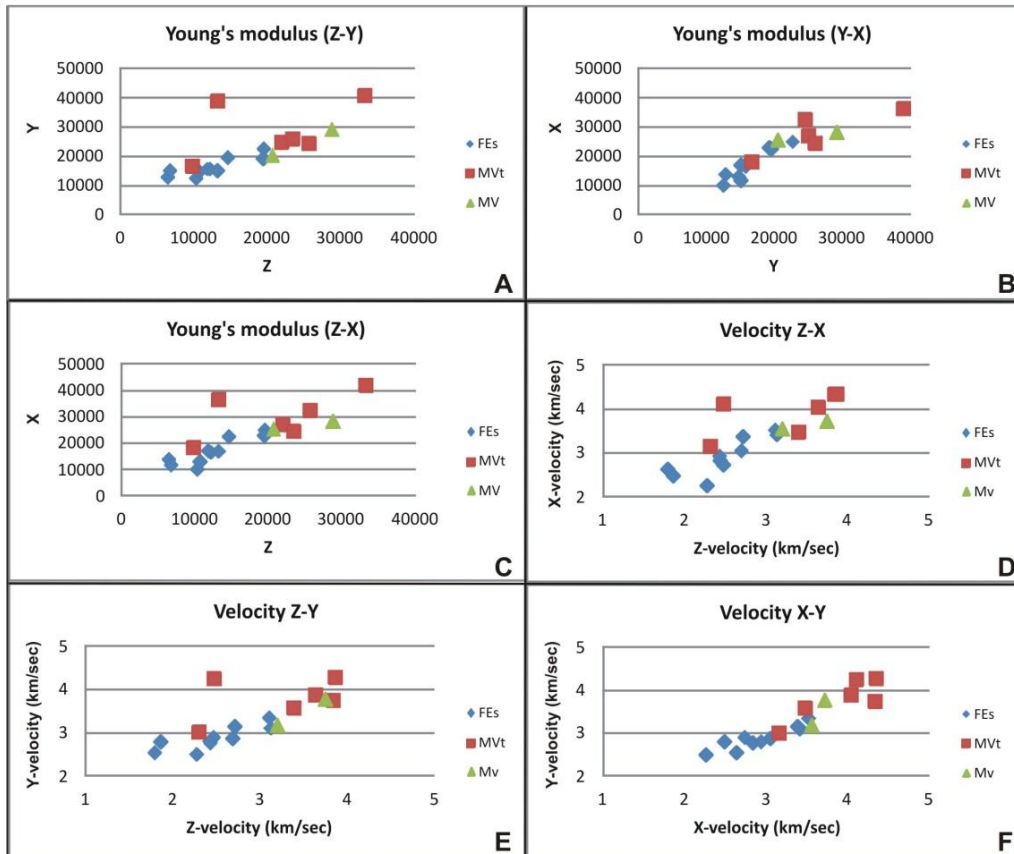
Fig. 6.5: *a - b - c)Young's modulus comparing the main lithofacies along the main directions; d - e - f) Velocity of main lithofacies along main directions*
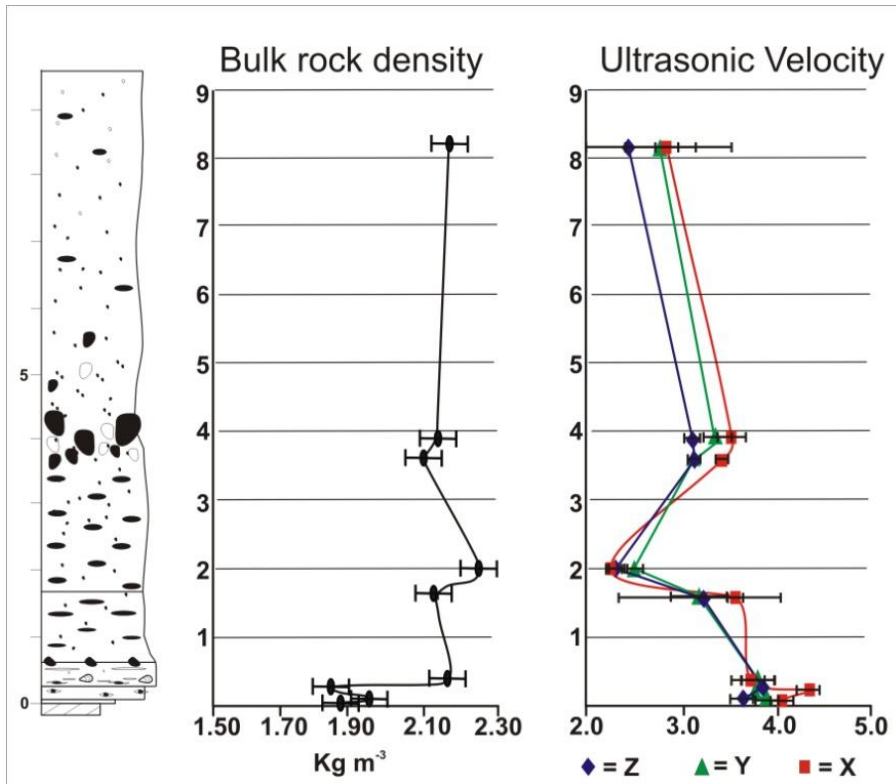
Fig. 6.6: *Section 14 - Punta Senoglio: bulk rock density values related with ultrasonic velocity*
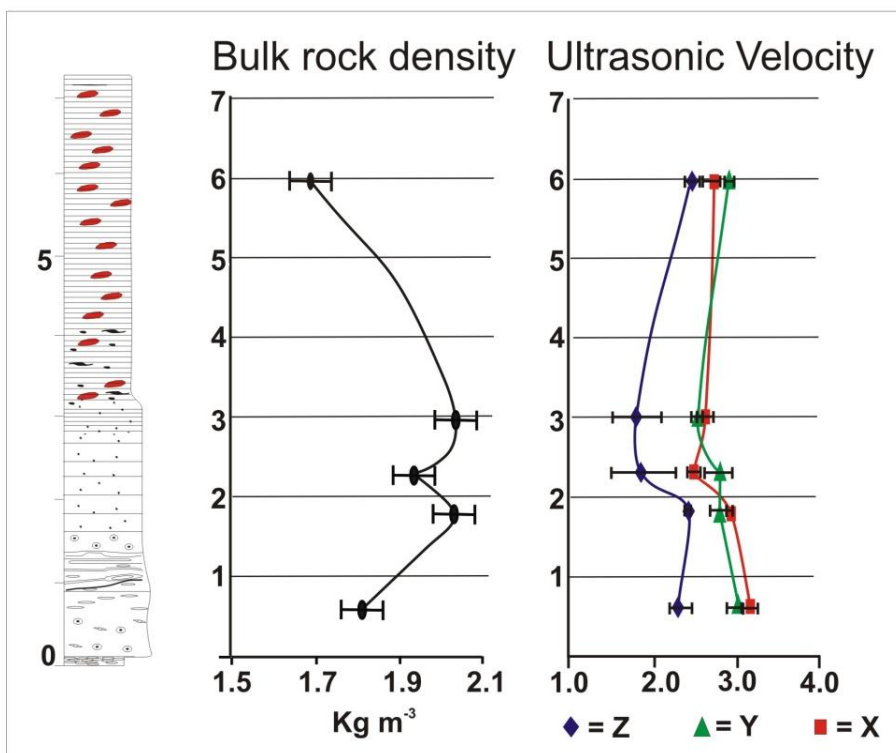
Fig. 6.7: *Section 6 - Matzaccara: bulk rock density values related with ultrasonic velocity*
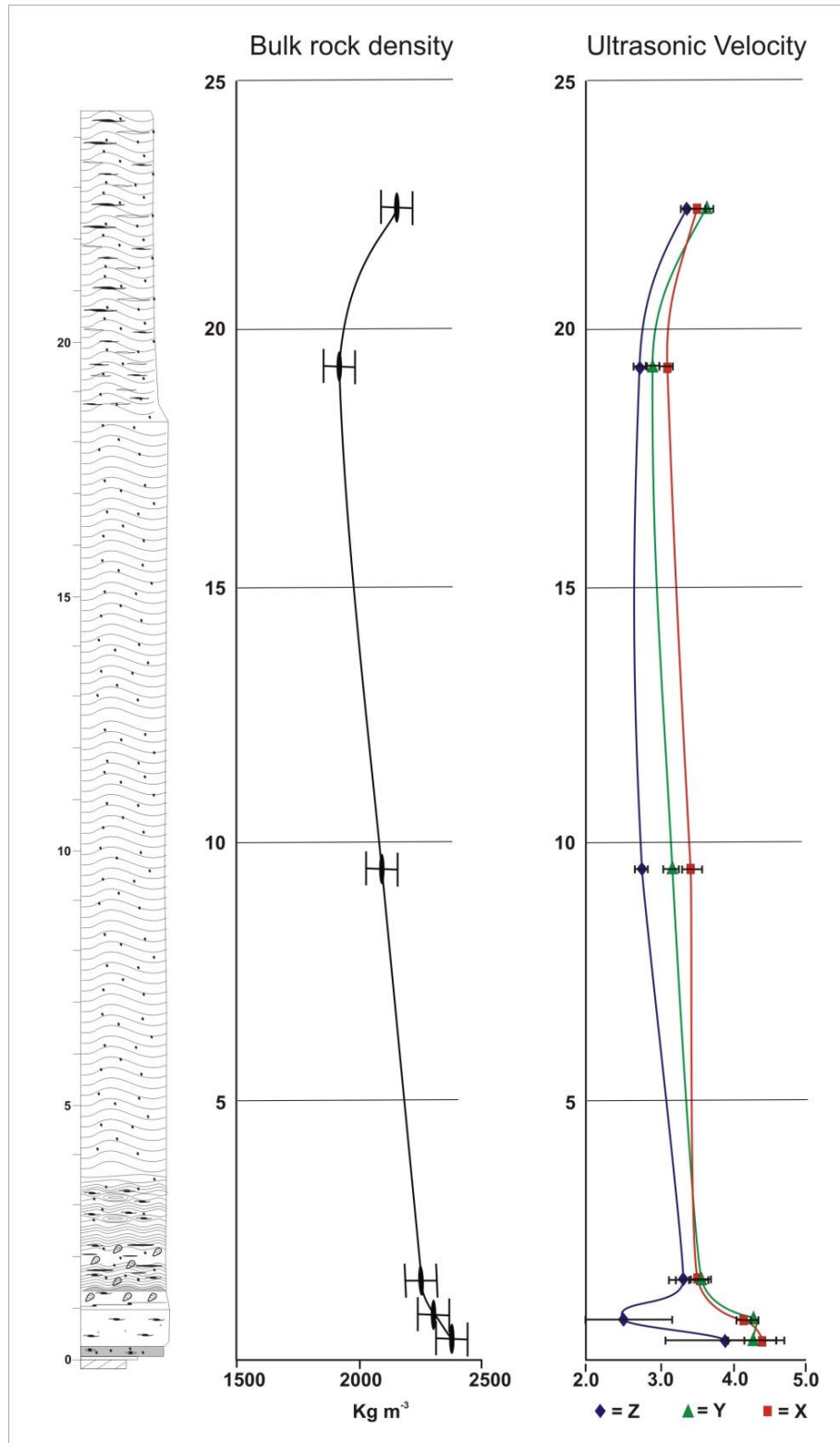
Fig. 6.8: *Section 29 - Mezzaluna: bulk rock density values related with ultrasonic velocity*
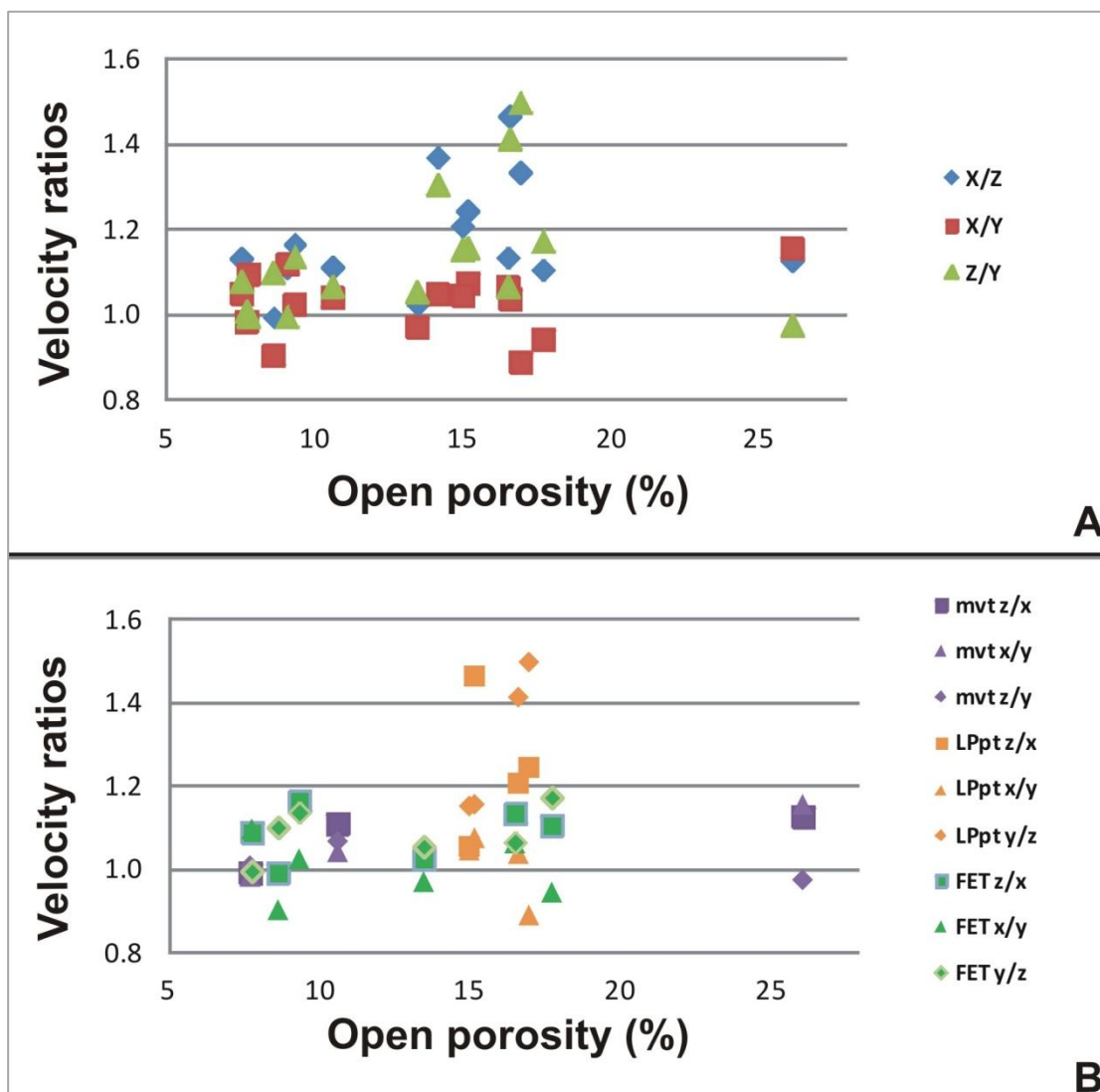
Fig. 6.9: *a) Velocity ratio in the main direction. b) The three main lithofacies are comprise inside three main breaks of open porosity.*

6.4 Petrographic and compositional features

6.4.1 Petrography

The petrographic features of the MUI were determined both form the mineralogical assemblage present in the fiammae, pumice and scoria fragments, and from the crystals or crystal beads present in the matrix. As a general rule, the evolved, nearly peralkaline nature of the ignimbrite reflects in the very poor content of mafic minerals. The loose crystals assemblage embedded in the matrix is invariant along the stratigraphic succession (<3.5 vol.% - determined with image analysis on thin sections) and it is

represented by sanidine, quartz and rare adversonite and clinopiroxene crystals. They are generally represented by mm-sized, loose euhedral crystals, broken crystals and crystals with resorbed rims (mainly quartz and sanidine). Differently from the matrix, fiammae are generally very porphyritic, with a crystal content variable between 15 vol.% (brownish spatters) and 18 vol.%. (blackish spatters). Sanidine crystals are the most abundant, and theyr are mainly mm-sized, euhedrals to sub-euhedrals, sometimes broken or with resorbed rims.

6.4.2 Compositional Data

The composition of the magma was determined from selected pieces of fiammae and pumice accurately isolated from the matrix by cutting them in the laboratory. Whole rock analyses on the matrix were only performed on fine-grained, glassy, isotropic samples from the basal vitrophyre. The complete dataset is reported in Tab. 6.5 (major elements) and Tab. 6.6 (trace elements). The SiO_2 content varies between 67 wt.% (vitrophyre) and 74 wt.% (matrix unit A1), while in juvenile and spatter fragments it ranges between 63 wt.% (unit B blackish fiamme) and 74 wt.% (unit B whitish fiamme). Total alkali content varies between 8-9 wt.% in the matrix and in the range 7 - 11 wt.% in the selected juvenile fragments. Analyses shows variable values in Al_2O_3 (9.56-16.25 wt.%) and relatively low contents in Fe_2O_3 (1.42-3.43 wt.%) typical of rhyolitic to trachytic, nearly peralkaline rocks (LeBas et al., 1986 - Fig. 6.9-a; Cox et al., 1979 - Fig. 6.9-b; Peccerillo and Taylor, 1976 - Fig. 6.9-c). Matrix and juvenile components are predominately rhyolite, while blackish spatters have a trachyte composition. In the classificative diagram of McDonalds (1974; Fig. 6.9-d) samples plot in the comendite to comenditic trachyte fields. Agpaitic index (molar Na_2O+K_2O/AL_2O_3) varies from 0.96 to 1.01, typical value of a slightly peralkaline rhyolite. According to Giordano et al. (2008), Tg temperature varies from 345 and 550 °C. Spider diagrams (Fig. 6.9-e) shows the trend of Rare earth elements (correct to Ordinary Condrite - Nakamura, 1974) with the classical Europium anomaly typical of highly fractionated magmas.

		MU-36b A0 matrix	MU-24 A1 matrix	MU-25 A1 fiamme	MU-27 B reddish fiamme	MU-28 B blackish fiamme	MU32b B whitish fiamme	MU-32C B blackish fiamme	MU-34 B whitish pomice
SiO_2	%	67.4	74.3	73.6	69.3	63.6	80.1	64.5	74
Al_2O_3	%	11.5	12.6	12.7	14.75	15.8	9.56	16.25	12.75
Fe_2O_3	%	2.76	3.09	3.19	3.43	3.62	1.42	3.47	2.35
FeO_{tot}	%	2.48	2.78	2.87	3.09	3.26	1.28	3.12	2.12
CaO	%	0.28	0.04	0.04	0.25	0.45	0.04	0.48	0.05
MgO	%	0.09	0.09	0.1	0.13	0.24	0.08	0.24	0.09
Na_2O	%	2.93	4.54	4.53	5.59	5.45	3.44	5.69	4.41
K_2O	%	5.1	4.72	4.87	5.03	5.77	3.69	5.86	4.69
Cr_2O_3	%	<0.01	<0.01	<0.01	<0.01	<0.01	<0.01	<0.01	<0.01
TiO_2	%	0.16	0.18	0.18	0.37	0.6	0.19	0.6	0.18
MnO	%	0.09	0.02	0.03	0.06	0.09	0.01	0.08	0.02
P_2O_5	%	0.03	0.03	0.01	0.02	0.09	0.02	0.11	0.04
SrO	%	<0.01	<0.01	<0.01	<0.01	<0.01	<0.01	<0.01	<0.01
BaO	%	0.04	<0.01	<0.01	<0.01	0.01	<0.01	0.01	<0.01
LOI	%	4.7	1.42	2.59	2.57	3.92	1.49	0.88	1
Total	%	95.08	101.03	101.84	101.5	99.64	100.04	98.17	99.58
Na_2O+K_2O	%	8.03	9.26	9.4	10.62	11.22	7.13	11.55	9.1
AIndex		0.90	1.00	1.00	0.99	0.96	1.01	0.97	0.97
Tg	(C°)	345	508	432	417	351	547	527	550

***Tab. 6.5:** Major elements of total rock analysis*

		MU-36b A0 matrix	MU-24 A1 matrix	MU-25 A1 fiamme	MU-27 B reddish fiamme	MU-28 B blackish fiamme	MU32b B whitish fiamme	MU-32C B blackish fiamme	MU-34 B whitish pomice
Ag	ppm	<1	<1	<1	<1	<1	<1	<1	<1
Ba	ppm	336	14.1	5.8	6.3	51.6	29	73.5	18.8
Ce	ppm	171.5	135	146	75.3	68.2	145.5	60.6	179.5
Co	ppm	0.7	<0.5	<0.5	<0.5	0.5	<0.5	0.5	1
Cr	ppm	<10	<10	<10	<10	10	<10	<10	<10
Cs	ppm	4.08	2.91	3.02	1.08	1.93	1.26	2.11	2.36
Cu	ppm	8	<5	<5	<5	12	<5	9	5
Dy	ppm	11.75	10.65	8.35	5.86	4.17	16.45	3.95	16.35
Er	ppm	7.29	6.86	4.76	3.83	2.33	12.8	2.09	10.15
Eu	ppm	0.14	0.26	0.22	0.23	0.95	0.63	0.99	0.84
Ga	ppm	25.8	28.7	28.5	28.8	23.6	24.5	23.5	28
Gd	ppm	11.45	9.87	8.18	5.43	4.64	11.15	4.23	16.15
Hf	ppm	15.7	17.1	17.7	10	4.5	16.6	4.5	17
Ho	ppm	2.39	2.19	1.62	1.24	0.79	3.9	0.75	3.35
La	ppm	91.7	77.3	78.8	40.4	34.4	60.1	31.5	107.5
Lu	ppm	1.04	1.13	0.74	0.59	0.28	2.2	0.26	1.58
Mo	ppm	7	2	3	2	3	<2	3	<2
Nb	ppm	86.6	95.9	99.7	57.1	39.8	90.3	37.5	91.8
Nd	ppm	72.5	65	61.4	34.4	29.4	47.5	26.9	85.9
Ni	ppm	5	<5	<5	<5	7	<5	6	<5
Pb	ppm	25	28	41	40	29	19	30	35
Pr	ppm	20.3	18.2	18	9.57	7.68	12.75	7.06	23
Rb	ppm	231	240	247	143	205	128.5	198.5	189.5
Sm	ppm	13.85	12.8	11.2	6.82	5.64	10.15	5.19	17.3
Sn	ppm	<1	6	7	5	<1	<1	<1	2
Sr	ppm	15.6	6.9	4.7	7.1	5.6	15.3	6.2	23.6
Ta	ppm	5.5	6.3	6.5	3.7	1.7	6.2	1.8	6.2
Tb	ppm	1.89	1.67	1.35	0.9	0.7	2.15	0.66	2.6
Th	ppm	25.6	28	28.7	12.65	6.19	22.6	6.2	27.5
Tl	ppm	0.5	<0.5	0.5	<0.5	<0.5	<0.5	<0.5	<0.5
Tm	ppm	1.06	1.08	0.73	0.58	0.32	2	0.3	1.52
U	ppm	6.06	4.95	5.53	2.85	1.41	5.05	1.46	7.38
V	ppm	5	<5	5	<5	5	<5	6	6
W	ppm	3	3	3	1	2	2	2	2
Y	ppm	66.5	56.1	42	36.7	21.5	120	19.6	91.2
Yb	ppm	6.96	7.33	4.82	3.81	2.01	13.5	1.86	9.95
Zn	ppm	106	74	97	128	204	28	208	58
Zr	ppm	618	686	721	414	162	672	166	672

Tab. 6.6: *trace elements of total rock analysis*
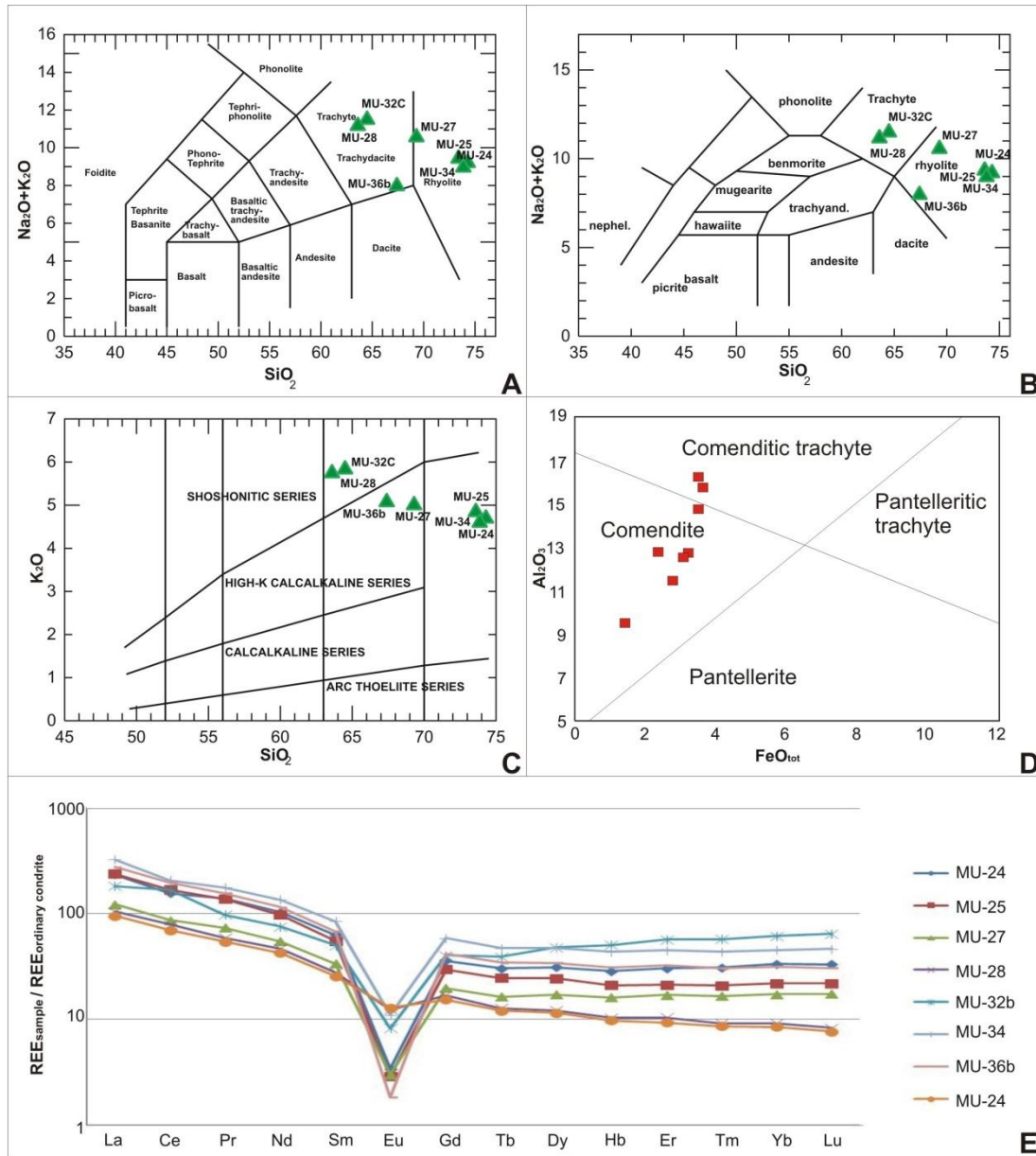
Fig. 6.10: *a) TAS digrams (Le Bas; 1976); b)SiO2-K2O diagrams(Cox et al. 1979); c) SiO2-Tot Alk diagrams (Pecerillo and Taylor,1976); d)Sample are comprise between comendite and comenditic trachyte (McDonald 1974); e) Spider diagrams of rare earth elements (normalized to Ordinary Condrite - Nakamura, 1974): all samples showed a decrease of Eu except samples MU24 and MU28.*

CHAPTER 7
DISCUSSION AND CONCLUSION

The Monte Ulmus Ignimbrite (MUI), despite the Miocene age, offers continuous, extensive exposures along several cliffs and erosive valleys of Sulcis mainland and the islands of San Pietro and Sant'Antioco. Tectonic deformation and metamorphism did not affect the region. The ignimbrite is dismembered by normal faulting along the N-S direction (N 10°) which in some cases offer an important view and access to the entire stratigraphy of the ignimbrite. The large exposure of the ignimbrite allows to identify variable paleotopographic setting which could be used to assess the transport, depositional and post-emplacement dynamics.

The detailed stratigraphic study of the ignimbrite provided significant data which allowed the location of the source area for the ignimbrite and the eruptive sequence responsible of the ignimbrite formation and emplacement. In addition, the MUI also represents a very clear example where several features typical of welded ignimbrites are clearly preserved and well exposed, such as primary structures (like foliation and lineation features, facies transitions, degassing structures,) and secondary structures related to rheomorphic flow also along very gently slopes.

7.1 Source area

The source areas of the MUI, and of the other ignimbrites of the Sulcis Volcanic District, are still object of debate, as no clear vent area or caldera is visible (except for some small domes and lava coulees of comenditic composition on the San Pietro Island). Only Pioli and Rosi (2005), basing on volcanological data from the Nuraxi Ignimbrite, suggested a possible vent area for this important ignimbritic unit in the sea, north of the San Pietro Island.

Data collected on MUI can help at defining the possible source area for the ignimbrite. Different lines of evidence derive from stratigraphic, lithological and sedimentological studies, but none of them may be considered as resolutive if taken singularly. We suggest that the integrated use of the different informations and their cross-checking is the most effective way for locating the possible vent(s) of the eruption.

- Fallout deposits at the base of the ignimbrite are thicker (and possibly coarser, given their often deep alteration) in the northern sector of the San Pietro Island; however, given the intense and pervasive argillification of these deposits, also their actual thickness may be locally modified.

- The flows directions were determined by the analysis of different kinds of kinematic indicators: i) embricated fiammae, ii) long axis of prolate vesicles, iii) ropy structures, iv) rotated fragments, v) lineated structures. Flow directions are roughly aligned along around the WNW-ESE direction, with some local divergence due to flow along paleovalleys or steep paleoslopes.

- The maximum clast size of lapilli embedded in the ignimbrite matrix show an important areal variability, with the largest clasts occurring in the areas dominated by the ExbT and MIbrT facies, in the northern sector of the San Pietro Island.

The integration of all these observations suggests that the most likely position for the source area is located a few kilometers N of the San Pietro Island, approximately in the same area proposed for the Nuraxi tuff (Pioli e Rosi, 2005).

7.2 Stratigraphy and timing of the eruption

The Monte Ulmus Ignimbrite is a rhyolitic to trachytic, high-grade, low aspect ratio ignimbrite cropping out on an area of 300 km^2 with a minimum estimated volume of 2.5 km^3. The thick reddish paleosoil below the MUI suggests a prolonged quiescence preceding the eruption. The cm-thick, normally graded, lapilli fallout bed immediately at the contact with the paleosoil testifies that the eruption started with a phase of convective, sustained column. The generally fine grain size of the fallout bed suggests a low altitude (tropospheric?) plume. The MUI is a composite deposit made by multiple

flow units, as suggested by the sharp contacts and sedimentological variations observed along the sequence, which was deposited in rapid succession, as suggested by the unique set of columnar jointing cross-cutting the entire deposit (single cooling unit).

The presence of a vitrophyre at the base of the first pyroclastic flow unit (A0), pervasively cross-cut by cm-spaced perlitic fractures, is indicative of rapid cooling processes on a wet surface that affected the first products emplaced. These first decimeters of the deposit does not show any clear relation with the preexisting topographic conditions, and this deposit possibly represented a thermal barrier for the following emplaced products. The following sub-units, both characterized by high matrix percentages, do not show evidence of prolonged breaks in deposition, and can be related with the occurrence of a few phases dominated by the formation of a collapsing fountain only staggered by brief pauses.

The thin, spherulite-rich, vitric layer at the base of sub-unit B and the evident unconformity (interpreted as erosional) between sub-unit A2 and B reinforce the hypothesis of the presence of short time breaks between these eruption phases.

Sub-unit B, characterized by a large amount of spatter fragments, a higher content of lithics fragments and lower percentage in matrix respect to the other sub-units, can be related with a phase of the eruption fed by a fissural vent, possibly during or after a phase of caldera forming, in agreement with similar products erupted at other volcanoes (Ignimbrite TL, Gran Canaria - Sumner and Branney, 2002).

7.3 Effects and change of topography during eruption

The Sulcis area and the islands of San Pietro and Sant'Antioco were characterized by a hilly topography with some important topographic irregularities before the eruption that emplaced the MUI. First emplaced deposits, showing a constant thickness (sub-unit A0), made a regular thin bed that mantled the preexisting topography, without inducing any substantial modification to it.

A NW-SE oriented valley, about 50 meters deep, located in the northern sector of the San Pietro Island strongly channelized the pyroclastic flows that deposited sub-unit A1, as testified by the variations in thickness distribution of this sub-unit, without producing a complete infill of the paleovalley. In medial to distal areas and inside this valley, sub-

unit A1 is thicker than A2, while on the topographic highs of the proximal area, sub-unit A1 presents a lower thickness respect to A2, suggesting a stronger topographic control on the flow path and on the depositional mechanisms (and possibly a lower associated kinetic energy) of A1 respect to those directly acting on A2.

The sub-unit A1 shows evidence of topographically-induced re-arrangement in the valley-filling deposits of the Sant'Antioco Island and thicknesses variable from 7 to 30 m between preexisting topographic highs and lows. Conversely, sub-unit A2 shows similar thickness in both these situations, possibly also a result of the quasi-flat conditions resulting from A1 emplacement. The important variability noted in the spacing of parting planes of the LPpT facies of both A1 and A2, with a large spacing (2 to 3 meters) at the base of the deposits infilling the topographic lows, and a thinner spacing corresponding to the facies deposited on the topographic reliefs, suggests an important influence of paleotopography on the sedimentation rate from the overriding pyroclastic current. Similarly, the effect of partial infilling of paleodepressions and progressive smoothing of topography exerted by the continuous, aggradational deposition is also recorded by the dm-spaced parting planes which characterize sub-unit A2.

The complete filling of the main paleovalleys of the San Pietro Island is finally related to the deposits of sub-unit B, which show important lateral variations in thickness, from 5 to 53 meters. The general orientation of the bedding planes of sub-unit B clearly records the local effects of paleotopography on transport and deposition: bedding planes gently dip in direction of the valley axis at the base, progressively passing upward into a plane parallel, horizontal foliation.

7.4 Dynamics of ignimbrite emplacement

The presence of the ignimbritic units above the basal fall deposit testifies that the ignimbrite was formed by collapse of eruptive column. The massive basal deposits of the first ignimbritic unit are well sorted with well-oriented, mm-sized glass shards in proximal area, becoming poorly sorted and progressively fine-grained in medial-distal areas. These deposits record a first emplacement phase with high depositional rates from a steady turbulent flow, as suggested by the MvesT lithofacies, which possibly

increased its thickness by gradual aggradation (Branney and Kokelaar, 1992). Locally, in the proximal area, the flow concentrated a thin basal non-particulate flow, that did not travel long distances, as suggested by partial coalescence between glass shards and the low rotational angle recorded by solid fragments. The contact with the substrate was the possible cause of a sudden decrease of temperature below the T_g (345 °C for sub-unit A0), resulting in the rapid quenching of the deposits and causing the early stop of the non-particulate flow. A second non-particulate flow formed and emplaced above this deposit. The presence of primary rheomorphic structures like sheath folds, less than 1m in size, possibly testifies the unsteady increase of shear stress inside the flow, mainly related to the coupling with of the overriding pyroclastic flows. Taking into account the well formed rotational structures inside the MVT lithofacies, it can be hypothesized that the formation of the non-particulate flow occurred during the emplacement phases.

The progressive increase of run-out of the ignimbrite units suggests that the pyroclastic cloud possibly became more dilute, as suggested by the general decrease of grain size and sorting, by the size decrease of the glass shards, and by the progressive decrease in the thickness of the massive lithofacies. We suggests that the initially turbulent flow that emplaced the massive portion gradually depleted in solid fragments, becoming more dilute and passing gradually to a laminar flow, in agreement with the model of Bursik and Woods (2000). With the increase of run-out, deposits record a change in emplacement processes. The presence of multiple parting planes (LPpT lithofacies) and breccia layers testifies to the freezing of different traction carpets emplaced en-masse, related with short depositional breaks, according with the "step-wise" aggradation model of Branney and Kokelaar (1992). The presence of the ropy structures between the different parting planes (which separate the multiple traction carpets) suggests an important gas entrapment linked with a high, although variable as suggested by the different spacing between the parting planes, sedimentation rate. The trapped gas, associated to the high temperature and low viscosity of the deposits at emplacement, favored the quick readjustment of the deposits in response also to small topographic irregularities, as in the case of Matzaccara area.

Strong changes in the eruption dynamics possibly occurred during the second part of the eruption. The absence of fall out deposits testify the early establishment of a high

eruption rate, with no sustained column phases (Freunt, 1999) and its consequent total collapse of the eruptive column.

The deposits of this phase are mainly characterized by a high percentage of juvenile and lithics lapilli to blocks, xenolitic metric-sized boulders (from the same eruption and from ancient eruptions), and by the presence of degassing pipes. The high amount of large spatters possibly suggests a low fragmentation degree of a low viscosity magma (Valentine et al., 2000). The vertical coarse-tail, reverse to normal grading of th spatter fragments can be interpreted in terms of mass flow variation in pyroclastic cloud, passing from a waxing phase of the eruption, to a steady to a waning phase. The eutaxitic texture and the absence of sharp changes in the lithological features suggest a gradual aggradation of the deposits from a steady current, and a depositional surface growing steadily. Deposits of Ignimbrite TL (Gran Canaria - Sumner and Branney, 2002) show similar features. The presence of coarse, platy, highly fragile blocks in the deposit of sub-unit B is suggestive of a rapid deposition within a laminar flow, in which blocks travelled like a surfboard, in the absence of important chaotic movements which could have induced breakage. The only weak folding of the single spatter fragments suggests a minor remobilization of the deposits just during emplacement, probably during the continuous passage of the overlying pyroclastic cloud. The abundant presence of degassing pipes is indicative of a deposits characterized by a fluid-rich depositional interface (Branney and Kokelaar, 2002).

Finally the presence of cognate fragments (from the lower sub-units) together with the large lithic boulders permit to hypotize that this eruption phase was possibly related with a caldera-forming phase, or with an important enlargement of the vent areas.

7.5 Welding processes

MUI shows evidences of syn-emplacement e post emplacement welding. Generally deposits show evidence of a syn-emplacement agglutination between particles, probably starting in a non-particulate flow, followed by a post-emplacement welding due to pure shear related to the progressively increasing lithostatic load (as testified by the bulk rock density profile in those sections not affected by rheomorphic processes or by strong post-emplacement degassing phases).

In sub-unit A0, the strong alignment of poorly compacted glass shards and the presence of Φ structures testify a welding process mainly controlled by lithostatic load. Evidence of mobilization like a non-particulate flow are rare in this deposit. The vitrophyric texture of the deposit (always present in the MVT facies) can be related to a high cooling rate affecting these basal portions of the ignimbrite, and poses a limit to the duration of the welding process. If put together, all these evidences are strongly suggestive of a rapidly aggrading, high concentration, particulate flow, in which deformation of glass shards was rapidly stopped at the reaching of the T_g of the glass , and compaction was mainly absorbed by total loss of void spaces and by the strong reorientation of the glass shards. Dense welding was possibly reached also thanks to the lack of a very fine-grained matrix, most prone to a rapid cooling, and to the very poor amount of ambient air incorporated into the depositional system of the pyroclastic current.

Differently from sub-unit A0, in the other sub-units of MUI welding processes were influenced also by the paleotopographic conditions. Sub-units A1, A2 and B, thermally isolated from the substrate, on topographic highs show evidence of a very early welding, under the effects of a pure shear component (lithostatic load) but also in the presence of a simple shear component. Simple shear was possibly related to the partial coupling of the progressively aggrading depositional surface with the base of the depositional system of the current, as suggested by the abundance of rotational structures and well developed lineations in the deposit. In correspondence of the topographic reliefs, agglutination in these sub-units possibly started only in the final phases of transport or during emplacement, with evidence of an incipient development of non-particulate flow behavior, mainly suggested by the poorly coalescent glass shards and by the poorly developed deformation of the coarse spatters.

On the contrary, deposits accumulated in paleovalleys present welding features that suggest an important role of secondary remobilization, especially in the presence of steeply dipping flanks. Re-adjustment processes of deposits which remained for prolonged times at high temperature (as also suggested by their granophyric texture), mainly due to gravitative effects or post-depositional deflation, resulted in the complete agglutination of particles, locally giving a "lava-like" aspect to deposits. The observed vertical gradients of bulk rock density justify this hypothesis (Schminke, 1974; 2010).

Finally, in the presence of a flat paleotopography, the microstructural features of the ignimbrite suggest that agglutination and welding of particles possibly started inside the current and were nearly completed under conditions of simple shear stress, as also evidenced by the W_k values close to 1. The high flow velocity, not affected by topographic irregularities, and the high temperature of the non-particulate flow favored the onset of early agglutination inside the current; the complexly folded glass shards and the σ rotational structures are evidences of this process.

7.6 Secondary rheomorphic phases

Some structures found in the MUI testify a multiphase post-emplacement remobilization of the deposits after their nearly complete welding and compaction. As a general rule, gravity exerted an important role on the post-emplacement deformation of the welded deposits, which could rapidly started moving along gently dipping slopes (lower than 10°).

Two main phases of secondary rheomorphic deformation possibly acted during and immediately after the deposition of the whole MUI. The first phase, occurred between the emplacement of sub-units A2 and B, was followed by another phase, which deformed the whole MUI after the emplacement of sub-unit B. The first rheomorphic phase is underlined by an angular unconformity particularly evident on the MUI sequences of the Sant'Antioco Island. The remobilization of the still hot deposits resulted in different structures, characterized by a plastic to rigid response of the deposits. In fact, deposits show a general plastic behavior at the macro-scale, with the development of decametric folds, while locally microscale fragile structures like breccia layers formed, possibly in response to local increases in the shear rate. The second, final rheomorphic phase affected the whole thickness of the deposit, developing decametric, roughly cylindrical folds with axis parallel to the strike of the paleoslope, associated with ramp structures and anticlinal large scale deformations (diapir-like). Deflating processes affecting the still plastic portions of deposits are testify from the vertical trend of bulk rock density that decrease in the central portion of the deposit.

7.7 Degassing phases

The MUI show structures which clearly testify the occurrence of an intens syn- and post-emplacement degassing during emplacement and after deposition.

Degassing-related structures formed at different scales. The microscopic pitting detected on the surface of glass shards of sub-unit A0 is clear evidence of a strong interaction between glass and gas trapped in deposit, able to chemically attack the glass. Conversely, the pervasive, centimetric perlitic fractures cutting across the MVT facies of sub-unit A0 testify to the occurrence of hydration processes before the complete cooling of the ignimbrite, and probably related with emplacement on a wet surface.

The MvesT facies, which characterizes some of the outcrops of sub-units A1and A2, is another evidence of an important phase of interaction between the fluids trapped in the ignimbrite and the ignimbrite itself. The high vesicularity present in the tuff is in agreement with an early welding of the deposit, which rapidly decreased its permeability creating a barrier to the gas loss and complete deflation of the deposit. Incipient welding and related degassing possibly occurred during deposition. The syn-emplacement character of the vesicles is in fact testified by their deformation under a simple shear stress, with the development of prolate vesicles and of the classical (at least in many ignimbrite deposits of the Sulcis area) ropy structures. The slightly prolate to oblate vesicle shapes are confirmed by the ultrasonic velocity ratios of MvesT lithofacies. Also the development of parting planes, especially those of the LPpT facies, can be associated to the presence of gas, which possibly accumulated along shearing planar structures during their formation. In this hypothesis, parting planes are formed by the local shearing of the ignimbrite due to the coupling with the still moving depositional system above. Shear planes preferentially concentrated millimetric to submillimetric gas vesicles (still evident in some cases), possibly also related to local temperature increase by friction and subsequent forced exsolution of magmatic gas from the glass shards. Post-emplacement deformation is recorded by the oblate shape of the vesicles and of the fiammae, and was mainly due to the lithostatic load.

The presence of metric- to decametric blisters is another clear evidence of the occurrence of an important, post-emplacement degassing phase. These structures clearly

formed during general degassing of the ignimbrite, in correspondence of facies with a very low internal permeability due to the rapid, syn- or immediately post-emplacement welding. The roughly hemispherical shape of blisters, and the intense coherent deformation of the foliation of the hosting deposit, suggest that degassing developed on a still plastic deposit and was caused by intrafolial migration of gas along the foliation and the parting planes. The abundance of these structures especially in the A2 sub-unit, not really close to the substrate, suggest that blisters formed by the general deflation-related degassing of the ignimbrite, rather than being related to local trapping of external fluids from the substrate, as described for example for blisters formed in an ignimbrite unit of Fantale (Ethiopia; Gibson, 1974).

Mainly in the proximal area, sub-unit B shows evidence of degassing at different stratigraphic heights. The main facies of the sub-unit are characterized by the presence of oblate vesicles and by well-formed degassing pipes. These structures are present at different stratigraphic height. The vertical elongation of the pipes testifies that these structures formed after the end of any laterally directed (shear) deformation of the deposit, during a pause in the local deposition of material. A crucial condition for the development of degassing pipes is that lithostatic load must allow fluid percolation. The presence of degassing structures truncated at top into the intermediate portions of the ignimbrite may be justified only with the occurrence of emplacement breaks during deposition and degassing of the ignimbrite.

7.8 Conclusion

MUI is a clearly example of a high grade ignimbrite forming by different emplacement processes of multiple pyroclastic flows.

Many features confirm that the deposits grew up by gradual aggradation or by step-wise aggradation from the pyroclastic currents, in agreement with the general model for ignimbrites of Branney and Kokelaar (1992). The different eruption phases were characterized by emplacement phases followed by a rapid rearrangement due to a topographic irregularities and separated by short emplacement breaks during the eruption. The rapid, mainly gravity-driven, rearrangement was favored by the combination of the low viscosity of the products, the high amount of gas in the deflating

deposits and the high emplacement temperatures of the pyroclastic flows, generally related also to a high sedimentation rate.

The deposits clearly show evidence of syn- and post-emplacement rheomorphism, that permit to discuss in detail the relative timing of emplacement, welding and deformation. The 15.5 Ma eruption started, few kilometers N of the San Pietro Island, with a column sustained phase followed by the emplacement of hot pyroclastic flows related to the transition from convective to collapsing conditions of the eruptive plume. After the deposition of basal deposits, rapidly quenched to form a vitrophyre, the following deposits possibly remained at temperature above the Tg for long periods. A first time-break separated the deposition of sub-unit A2 and B; during this time-break, the deposits moved down-slope like a non-particulate flow, mainly responding to deflating processes or rheomorphism linked with steeply dipping surfaces. The eruption possibly ended with a final caldera collapse phase, during which a fissural activity developed, characterized by coarse fragmentation of low viscosity magma. After this phase, the deposit underwent a final rheomorphic phase, interesting the whole of the sequence. The still plastic conditions favored the secondary partial or total remobilization of the deposits, during which a strong degassing phases developed, forming structures like blisters, anticlinal structures, megafolds and ramps. The ubiquitous occurrence of these structures allow to define the MUI as a rheomorphic ignimbrite (Chapin and Lowell, 1979; Wolff and Wright, 1981; Andrews at al. 2008). The final phase of cooling involved the whole thickness of the deposits, resulting in a single cooling unit. While the Tg value of rhyolitic products generally lays in the range 620-650 °C, the Tg values determined for the MUI was as low as about 345 °C, confirming the observation of a prolonged duration of conditions favorable to the development of rheomorphic deformation.

The study of MUI and its macro- and micro-structural features is strongly suggestive of a general step-wise aggradation from a continuous passage of the pyroclastic current(s) over the depositional interface. The upward decrease in the shear stress recorded in progressively decreasing rotation angle of the fragments of some sub-units, as well as the observed decrease in grain size, can be hardly correlated with an en-masse process of deposition.

The MUI well record also the different behavior of deposits on different paleotopographic conditions. On topographic highs, deposits are generally not affect by rheomorphic processes. On the contrary, on topographic lows and in flat conditions the deposits are clearly affected by rheomorphic processes just during emplacement phases. The vertical gradients of density and other physical properties observed in the ignimbrite clearly reflect this evidence, and can be used to discuss the relative importance of welding, rheomorphic and degassing processes.

APPENDIX

Methodology

Sample collection

69 samples were collected in the area of Sulcis, Sant'Antioco and San Pietro islands, at variable stratigraphic heights, where obvious lithofacies variations or stratigraphic contacts could be seen. Sections were selected by different features: sections where base were visible, paleotopographic conditions, distance from inferred source area.

DEM and geodatabase

The DEM (Digital Elevation Model) of the area was created starting from the TIN models of the CTR 1:10,000 maps, using the software ArcGis 9.3. Each georeferenced sections were located on the DEM. Finally was create a geodatabase with the main features of each sections (total and partial thickness, main structures and lithofacies).

Thin sections

In order to characterize the petrographycal associations, the main micro-structures and to describe devitrification textures of each samples, were analyzed about 46 oriented thin-sections representative of the entire MUI succession. They were prepared with two different size (2.5 x 3 cm and 4 x 6 cm) at the Sbrana Laboratories (Piombino-Italy). For each samples were prepared two thin-sections: one parallel oriented to the strain directions and foliation planes and one normal oriented respect to the strain directions and parallel to the foliation planes.

Thin-sections were firstly analyzed by optical microscope at low-magnification to examine welding degree, crystal paragenesis and the presence of kinematic indicators.

Thin sections were later scanned in Geneva using a thin-section high-resolution scanner that performed 3600 dpi TIFF images. Phenocrystals and lithic fragments were outlined using a graphic software and afterwards the images were binarized. The binary images were analyzed by Image-J software (Wohlez et al., 1989) to measured the percentage of crystals and lithic fragments, major and minor axes length, the angles between the main axes and shear versus. Crystals lower or equal to the pixel size or with AR near to one were doesn't taking in account.

The same thin sections were used for SEM analyses. These analyses were performed at the department of Mineralogy of Geneva with the Scanning electron microscope JEOL JSM7001F. Sem analysis were performed to investigate the morphologies and in general the main features of glass shards, microscale evidence of shear stress and gas/liquid phases interactions.

Chemical analyses

Bulk-rock chemical analyses were performed at ALS Minerals laboratories on 8 samples. Chemical analyses of Monte Ulmus Unit were focused principally on juvenile fragments (fiamme and scoria fragments) and only in the case of unit A0 and A1 on the matrix. Mayor elements were determinated by ICP-OES and trace elements with ICP-MS by digestion of melt disk of lithium metaborate/tetraborate. Tg temperature were determined using the Giordano et al (2008) model.

Lithofacies

About 41 stratigraphic sections (Tab.a-1), located in San Pietro and Sant'Antioco islands and in the Sulcis mainland (Fig. 5.1), were described and laterally correlated. The main lithofacies were distinguished for each sections and a qualitative descriptions of fragments (fiammae, lithic fragments and free crystals) were given for each lithofacies. In few representative stratigraphic sections, a quantitative evaluation of component percentages were performed with image analysis at the meso- and micro-scales. Evaluations of welding degree were determined using the classification proposed by Streck and Grunder (2005) and Mundula et alii (2009), based on the fiammae aspect ratios (ratio between major and minor axes) and on the orientation degree of juvenile fragments.

Tab. a-1: *Stratigraphic sections studied for Monte Ulmus Ignimbrite. Coordinate sistem is metric GCS Rome 1940*

Number	Section	Longitude	Latititude	Total thickness (m)
1	Cala Sapone (fronte bar)	1446850	4317860	2.50
2	Cala Sapone (lungo costa)	1446810	4317850	3.00
3	Villaggio Polifemo	1446620	4317510	30.50
4	Porto della signora	1446000	4318290	17.00
5	Penisola Porto di Triga	1446590	4317330	20.00
6	Matzaccara	1452220	4331370	7.10
7	Sud Villaggio Polifemo	1446680	4317420	22.00
8	S'ega de Arrexinus	1446810	4316870	16.00
9	Fianco nord cala sapone	1446610	4317920	23.00
10	Nord cala sapone	1446420	4317910	30.00
11	Porto della signora	1446110	4318240	24.00
12	Piramide	1438690	4331970	9.10
13	Strada cava carloforte	1438750	4332230	10.00
14	Punta senoglio	1435200	4335840	9.20
15	Giba	1468300	4326170	10.00
16	Sud monte Ulmus	1454600	4333970	10.00
17	Cala senoglio	1434970	4335630	2.00
18	Isola di stea	1436440	4336460	36.00
19	Nord Paese Carloforte (19a to 19 f)	1439180	4333470	55.00
20	Canale guidi	1436090	4336100	41.00
21	Golfo isola di stea	1436350	4336230	52.00
22	SW punta delle oche	1436640	4336680	30.00
23	Cala di memerosso	1437860	4336910	20.00
24	Pulpito	1437590	4336870	23.00
25	Grotte punta dell'oca	1436740	4336980	28.00
26	Punta di Stea A	1436220	4336200	44.00
27	Punta di Stea B	1435920	4336000	26.00
28	Cala lunga - sant'antioco	1445720	4319480	38.75
29	Poggio di mezzaluna	1447200	4316100	24.50
31	Vitrofiro strada cava	1437710	4333140	10.00
32	Punta regolina	1438600	4337180	16.00
33	Guardia dei mori	1438900	4335390	20.00
34	Monte ulmus(carottaggio)	1453730	4335040	45.00
35	Nord matzaccara(carottaggiof.s.37)	1452310	4333950	82.50
36	Sud-est paringianu(carotaggio f.s.36)	1451500	4335910	98.00
37	Is orixionis (carottaggio f.s.19)	1450830	4337380	62.50
38	Terra niedda(carotaggio f.s. 35)	1453840	4336630	57.50
39	Sa schina de mesu(carotaggio f.s. 22)	1452650	4337040	70.00
41	Riu s'ega marionis	1448280	4324960	20.00

Tab. a-2: *Samples used for the main analysis*

Sample	Section	Details
MU-1	6 - Matzaccara	A1 central
MU-3	6 - Matzaccara	A1 top
MU-4	6 - Matzaccara	A1 base
MU-7	1 - Cala Sapone	A0 (matrix)
MU-8	1 - Cala Sapone	A0 - A1
MU-10	12 - Piramide	B1 (scoria)
MU-11	12 - Piramide	B1 (scoria)
MU-12	12 - Piramide	B1 (scoria)
MU-24	14 - Punta Senoglio	A (base matrix)
MU-25	14 - Punta Senoglio	A (fiamme)
MU-26	14 - Punta Senoglio	A (top matrix)
MU-27	14 - Punta Senoglio	B (reddish scoria)
MU-28	14 - Punta Senoglio	B (blackish scoria)
MU-29	14 - Punta Senoglio	B (brownish scoria)
MU-30	14 - Punta Senoglio	B (base reddish matrix)
MU-31	14 - Punta Senoglio	B (top reddish matrix)
MU-32	14 - Punta Senoglio	B (base grayish matrix)
MU-33	14 - Punta Senoglio	B (reddish scoria)
MU-34	14 - Punta Senoglio	B (white pomice from reddish matrix)
MU-35	14 - Punta Senoglio	B (white pomice from greyish matrix)
MU-36	14 - Punta Senoglio	A0 (top)
MU-37	14 - Punta Senoglio	A0 (base)
MU-49	6 - Matzaccara	B (matrix)
MU-50	29 - Mezzaluna	A1 (base)
MU-51	29 - Mezzaluna	A1 (base)
MU-52	29 - Mezzaluna	A1 (base)
MU-54	29 - Mezzaluna	A2 (central)
MU-55	29 - Mezzaluna	A2 (top)
MU-56	29 - Mezzaluna	B (base)
MU-57	29 - Mezzaluna	B (top)
MU-58	6 - Matzaccara	B
MU-59	14 - Punta Senoglio	B (top)
MU-60	1 - Cala Sapone	Basal fall
MU-61	1 - Cala Sapone	A0 (4-6 cm from base)
MU-62	1 - Cala Sapone	A1
MU-63	1 - Cala Sapone	A1 (58 cm from base)
MU-64	1 - Cala Sapone	A1 (embricated fiamme - 60 cm from base)
MU-65	1 - Cala Sapone	A1 (tensiongauches - 110 from base)
MU-66	12 - Piramide	B (pomice)
MU-67	12 - Piramide	B (brownish spatter)
MU-68	12 - Piramide	B (blackish fiamma)
MU-69	12 - Piramide	B (blackish spatter)

Strain analyses

The strain analyses were performed on 20 samples, took principally on lineated lithofacies of sub-unit A1 (Matzaccara - Sect. 6) and on massive and lineated facies of sub-unit A0 and A1 (San Pietro Island - Sect. 14).

To performed the strain analyses, each solid particles (crystals and lithic fragments) were counturned using a graphic software (Adobe Photoshop) and then binarized. The dimensional features of each fragments (major and minor axes lenght, AR) and α (angle between the main axis and shear direction) were determined using the free-software Image-J (Abramoff et al., 2004). Fragments with size similar or smaller than the pixel size and particles with AR smaller than 1.5 weren't took in account.

Two main classes were considered during analyses on the base of their aspect ratios: one comprised between 1.5 and 2 and the second one comprised between 2 and 3.5. Fragments with aspect ratio lower than 1.5 weren't considered. Detailed Data were attached in Electronic Supplementary Material.

The contribution of pure shear and simple shear in rotational processes were determined using the kinematic vorticity number (W_k) (Tikoff and Fossen, 1998; Ventura, 2001):

$$W_k = \cos \{ \arctg[2\mathrm{Log}_n(\alpha)/\gamma] \}$$

where:

α is pure shear contribution and γ is the simple shear contribution. Values can ranges between 0 (pure shear) and 1 (simple shear).

Density:

Bulk rock density were studied on 23 cubic samples collected in three reference sections (number 6, 14 and 29), chosen on the base of paleotopographic conditions and their position respect to the source area.

Samples were cut into 5 cm side cubes, with two sides parallel to the foliation planes and oriented respect to the flow directions (Fig. a-2). Samples were oven-dried at 60 °C for 6 days. Bulk rock density on these samples were determined by different ways to evaluate the errors. Volume values firstly were geometrically determined. After that volume were determined in accord with the Archimedes' principle: dry samples firstly were weighted in air and after that covered by parafilm and weighted in air and in water.
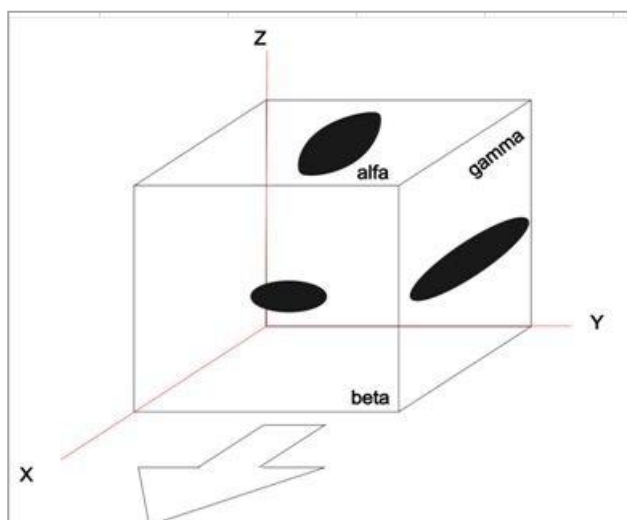
Fig. a-2: *Side nomenclature in cubic samples*

Helium picnometer

Two different helium picnometers were used for analyses: a Quantachrome Instruments' Ultrapycnometer-1000 of the Department of Chemical and Geological Sciences of Cagliari, and a Quantachrome Instruments' Ultrapyc-1200 sited at Department of Mineralogy of Geneva.

Helium picnometer was used to investigate the samples micro-porosities. The analyses were taken on 6 samples, 6 mm side, took in section 14 (Tab. a-3). Volume values were determined, with an accepted standard deviations of 0.005%, using different settings to understand what measure weren't affected by instrument errors. Different purge methods were set to determine the volume values: continue flow with different purge time (1, 3 and 5 minutes) and pulse flow with different pulse numbers (30, 50 and 80) for each series.

DRE (dense rock equivalent) were calculated measuring dry powder densities from 4 samples (A0, A1, B base and B top) using a helium picnometer. Measures were repeated 15 times with 5 minutes flow purge times with standard deviation requested lower than 0.005% (Fig. a-3).

Tab. a-3: *single measurements of micro-cubic sample with average value of different purging time*

Sample		1 min.			3 min.			5 min.	
		Volume	Density		Volume	Densità		Volume	Densità
MU-24 1	1	2.9048	2544.10	1	2.9255	2530.82	1	2.9426	2516.11
	2	2.9175	2533.02	2	2.9302	2526.76	2	2.9438	2515.08
	3	2.9192	2531.55	3	2.9328	2524.52	3	2.9421	2516.54
weight	4	2.9191	2531.64	4	2.9313	2525.81	4	2.9405	2517.91
7.3901	5	2.9180	2532.59	5	2.9300	2526.93	5	2.9406	2517.82
	6	2.9201	2530.77	6	2.9310	2526.07	6	2.9397	2518.59
	7	2.9199	2530.94	7	2.9315	2525.64	7	2.9450	2514.06
	8	2.9214	2529.64	8	2.9326	2524.69	8	2.9386	2519.53
	9	2.9220	2529.12	9	2.9293	2527.53	9	2.9380	2520.05
	10	2.9228	2528.43	10	2.9344	2523.14	10	2.9384	2519.70
MU-24 2	1	2.6741	2530.98	1	2.6894	2527.44	1	2.6877	2529.04
	2	2.6772	2528.05	2	2.6926	2524.44	2	2.6845	2532.05
	3	2.6772	2528.05	3	2.6888	2528.01	3	2.6850	2531.58
weight	4	2.6786	2526.73	4	2.6885	2528.29	4	2.6848	2531.77
6.7681	5	2.6797	2525.69	5	2.6878	2528.95	5	2.6843	2532.24
	6	2.6785	2526.82	6	2.6894	2527.44	6	2.6841	2532.43
	7	2.6786	2526.73	7	2.6898	2527.07	7	2.6824	2534.04
	8	2.6793	2526.07	8	2.6869	2529.79	8	2.6819	2534.51
	9	2.6800	2525.41	9	2.6861	2530.55	9	2.6854	2531.21
	10	2.6817	2523.81	10	2.6872	2529.51	10	2.6857	2530.92
MU-24 3	1	2.3522	2542.90	1	2.3571	2546.86	1	2.3509	2553.58
	2	2.3582	2536.43	2	2.3561	2547.94	2	2.3550	2549.13
	3	2.3607	2533.74	3	2.3555	2548.59	3	2.3562	2547.83
weight	4	2.3615	2532.88	4	2.3541	2550.10	4	2.3545	2549.67
5.9814	5	2.3631	2531.17	5	2.3529	2551.40	5	2.3545	2549.67
	6	2.3628	2531.49	6	2.3532	2551.08	6	2.3528	2551.51
	7	2.3639	2530.31	7	2.3539	2550.32	7	2.3525	2551.84
	8	2.3644	2529.77	8	2.3529	2551.40	8	2.3517	2552.71
	9	2.3648	2529.35	9	2.3518	2552.60	9	2.3517	2552.71
	10	2.3648	2529.35	10	2.3501	2554.44	10	2.3527	2551.62
MU-24 4	1	2.7392	2542.42	1	2.7639	2521.80	1	2.7617	2523.81
	2	2.7490	2533.36	2	2.7662	2519.70	2	2.7651	2520.70
	3	2.7503	2532.16	3	2.7662	2519.70	3	2.7642	2521.53
weight	4	2.7521	2530.50	4	2.7663	2519.61	4	2.7632	2522.44
6.9642	5	2.7509	2531.61	5	2.7636	2522.07	5	2.7615	2523.99
	6	2.7540	2528.76	6	2.7632	2522.44	6	2.7611	2524.36
	7	2.7537	2529.03	7	2.7621	2523.44	7	2.7607	2524.72
	8	2.7517	2530.87	8	2.7626	2522.99	8	2.7614	2524.08
	9	2.7561	2526.83	9	2.7623	2523.26	9	2.7590	2526.28
	10	2.7557	2527.20	10	2.7624	2523.17	10	2.7601	2525.27

Tab. a-3: *continue*

Sample		1 min. Volume	Densità		3 min. Volume	Densità		5 min. Volume	Densità
MU-24 5	1	2.5283	2521.02	1	2.5494	2500.86	1	2.5432	2506.96
	2	2.5396	2509.80	2	2.5502	2500.08	2	2.5447	2505.48
	3	2.5389	2510.50	3	2.5513	2499.00	3	2.5481	2502.14
weight	4	2.5405	2508.92	4	2.5500	2500.27	4	2.5510	2499.29
6.3739	5	2.5430	2506.45	5	2.5531	2497.24	5	2.5477	2502.53
	6	2.5423	2507.14	6	2.5497	2500.57	6	2.5486	2501.65
	7	2.5401	2509.31	7	2.5524	2497.92	7	2.5465	2503.71
	8	2.5429	2506.55	8	2.5509	2499.39	8	2.5037	2546.51
	9	2.5416	2507.83	9	2.5464	2503.81	9	2.5051	2545.09
	10	2.5400	2509.41	10	2.5470	2503.22	10	2.4997	2550.59
MU-24 6	1	1.9849	2570.21	1	1.9863	2568.90	1	2.0331	2521.03
	2	1.9950	2557.19	2	2.0423	2498.46	2	2.0371	2516.08
	3	1.9967	2555.02	3	2.0387	2502.87	3	2.0316	2522.89
weight	4	1.9973	2554.25	4	2.0306	2512.85	4	2.0367	2516.57
5.1016	5	1.9985	2552.71	5	2.0341	2508.53	5	2.0361	2517.31
	6	2.0009	2549.65	6	2.0337	2509.02	6	2.0292	2525.87
	7	2.0010	2549.53	7	2.0343	2508.28	7	2.0399	2512.62
	8	2.0001	2550.67	8	2.0332	2509.64	8	2.0319	2522.52
	9	1.9989	2552.20	9	2.0323	2510.75	9	2.0301	2524.75
	10	1.9996	2551.31	10	2.0394	2502.01	10	2.0295	2525.50
MU-26 1	1	2.7882	2553.73	1	2.8083	2535.77	1	2.8095	2534.69
	2	2.7999	2543.06	2	2.8093	2534.87	2	2.8130	2531.53
	3	2.8008	2542.24	3	2.8092	2534.96	3	2.8092	2534.96
weight	4	2.8012	2541.87	4	2.8084	2535.68	4	2.8119	2532.52
7.1203	5	2.8011	2541.97	5	2.8078	2536.22	5	2.8071	2536.85
	6	2.8023	2540.88	6	2.8072	2536.76	6	2.8122	2532.25
	7	2.8043	2539.07	7	2.8075	2536.49	7	2.8092	2534.96
	8	2.8019	2541.24	8	2.8089	2535.23	8	2.8067	2537.21
	9	2.8035	2539.79	9	2.8073	2536.67	9	2.8062	2537.67
	10	2.8047	2538.70	10	2.8047	2539.02	10	2.8075	2536.49
MU-26 2	1	3.1123	2603.48	1	3.1689	2557.35	1	3.1688	2557.43
	2	3.1253	2592.65	2	3.1716	2555.18	2	3.1721	2554.77
	3	3.1298	2588.92	3	3.1707	2555.90	3	3.1713	2555.42
weight	4	3.1336	2585.78	4	3.1714	2555.34	4	3.1687	2557.52
8.1028	5	3.1338	2585.61	5	3.1699	2556.55	5	3.1665	2559.29
	6	3.1330	2586.28	6	3.1698	2556.63	6	3.1666	2559.21
	7	3.1338	2585.61	7	3.1694	2556.95	7	3.1666	2559.21
	8	3.1329	2586.36	8	3.1708	2555.82	8	3.1664	2559.37
	9	3.1370	2582.98	9	3.1690	2557.27	9	3.1659	2559.78
	10	3.1367	2583.22	10	3.1698	2556.63	10	3.1657	2559.94

Tab. a-3: *continue*

Sample		1 min. Volume	1 min. Densità		3 min. Volume	3 min. Densità		5 min. Volume	5 min. Densità
MU-26 3	1	3.2301	2573.91	1	3.2389	2502.08	1	3.2352	2570.60
	2	3.2386	2567.16	2	3.2395	2501.62	2	3.2387	2567.82
	3	3.2412	2565.10	3	3.2409	2500.54	3	3.2402	2566.63
weight	4	3.2414	2564.94	4	3.2406	2500.77	4	3.2370	2569.17
8.3140	5	3.2427	2563.91	5	3.2404	2500.93	5	3.2368	2569.33
	6	3.2422	2564.31	6	3.2393	2501.78	6	3.2358	2570.12
	7	3.2417	2564.70	7	3.2406	2500.77	7	3.2377	2568.61
	8	3.2429	2563.75	8	3.2389	2502.08	8	3.0745	2704.96
	9	3.2437	2563.12	9	3.2393	2501.78	9	3.2381	2568.30
	10	3.2441	2562.81	10	3.2385	2502.39	10	3.2380	2568.38
MU-26 4	1	2.5623	2552.90	1	2.5787	2537.56	1	2.5745	2541.70
	2	2.5772	2538.14	2	2.5799	2536.38	2	2.5795	2536.77
	3	2.5792	2536.17	3	2.5792	2537.07	3	2.5796	2536.67
weight	4	2.5800	2535.39	4	2.5777	2538.54	4	2.5786	2537.66
6.5413	5	2.5822	2533.23	5	2.5768	2539.43	5	2.5777	2538.54
	6	2.5824	2533.03	6	2.5761	2540.12	6	2.5759	2540.32
	7	2.5815	2533.91	7	2.5758	2540.41	7	2.5765	2539.72
	8	2.5835	2531.95	8	2.5757	2540.51	8	2.5761	2540.12
	9	2.5836	2531.85	9	2.5777	2538.54	9	2.5765	2539.72
	10	2.5820	2533.42	10	2.5762	2540.02	10	2.5740	2542.19
MU-26 5	1	3.1769	2578.30	1	3.2312	2535.37	1	3.2283	2537.65
	2	3.2010	2558.89	2	3.2333	2533.73	2	3.2337	2533.41
	3	3.2059	2554.98	3	3.2339	2533.26	3	3.2337	2533.41
weight	4	3.2082	2553.15	4	3.2336	2533.49	4	3.2334	2533.65
8.1910	5	3.2088	2552.67	5	3.2326	2534.28	5	3.2326	2534.28
	6	3.2090	2552.51	6	3.2318	2534.90	6	3.2315	2535.14
	7	3.2119	2550.20	7	3.2323	2534.51	7	3.2317	2534.98
	8	3.2111	2550.84	8	3.2328	2534.12	8	3.2312	2535.37
	9	3.2119	2550.20	9	3.2330	2533.96	9	3.2323	2534.51
	10	3.2135	2548.93	10	3.2307	2535.77	10	3.2299	2536.39
MU-26 6	1	2.6381	2557.79	1	2.6793	2518.90	1	2.6900	2508.88
	2	2.6525	2543.90	2	2.6882	2510.56	2	2.6925	2506.56
	3	2.6528	2543.61	3	2.6880	2510.75	3	2.6904	2508.51
weight	4	2.6526	2543.81	4	2.6867	2511.97	4	2.6906	2508.33
6.7477	5	2.6515	2544.86	5	2.6865	2512.15	5	2.6891	2509.72
	6	2.6531	2543.33	6	2.6864	2512.25	6	2.6891	2509.72
	7	2.6539	2542.56	7	2.6884	2510.38	7	2.6880	2510.75
	8	2.6515	2544.86	8	2.6862	2512.43	8	2.6885	2510.28
	9	2.6534	2543.04	9	2.6840	2514.49	9	2.6893	2509.54
	10	2.6533	2543.13	10	2.6872	2511.50	10	2.6897	2509.16

Tab. a-3: *continue*

Sample		1 min. Volume	Densità		3 min. Volume	Densità		5 min. Volume	Densità
MU-32 1	1	3.3021	2507.37	1	3.3604	2463.93	1	3.3582	2465.55
	2	3.3131	2499.05	2	3.3648	2460.71	2	3.3613	2463.27
	3	3.3172	2495.96	3	3.3629	2462.10	3	3.3607	2463.71
weight	4	3.3205	2493.48	4	3.3628	2462.17	4	3.3600	2464.23
8.2796	5	3.3210	2493.10	5	3.3602	2464.08	5	3.3595	2464.59
	6	3.3214	2492.80	6	3.3620	2462.76	6	3.3586	2465.25
	7	3.3197	2494.08	7	3.3631	2461.95	7	3.3595	2464.59
	8	3.3232	2491.45	8	3.3632	2461.88	8	3.3588	2465.11
	9	3.3230	2491.60	9	3.3621	2462.69	9	3.3583	2465.47
	10	3.3202	2493.71	10	3.3623	2462.54	10	3.3586	2465.25
MU-32 2	1	3.4068	2522.40	1	3.4363	2501.79	1	3.4278	2507.99
	2	3.4231	2510.39	2	3.4365	2501.64	2	3.4281	2507.77
	3	3.4243	2509.51	3	3.4345	2503.10	3	3.4294	2506.82
weight	4	3.4259	2508.33	4	3.4343	2503.25	4	3.4280	2507.85
8.5933	5	3.4263	2508.04	5	3.4323	2504.71	5	3.4280	2507.85
	6	3.4247	2509.21	6	3.4325	2504.56	6	3.4280	2507.85
	7	3.4275	2507.16	7	3.4314	2505.36	7	3.4274	2508.29
	8	3.4282	2506.65	8	3.4308	2505.80	8	3.4276	2508.14
	9	3.4272	2507.38	9	3.4312	2505.51	9	3.4290	2507.12
	10	3.4271	2507.46	10	3.4329	2504.27	10	3.4304	2506.09
MU-32 3	1	2.6040	2555.88	1	2.6207	2539.86	1	2.6158	2544.61
	2	2.6161	2544.05	2	2.6217	2538.89	2	2.6198	2540.73
	3	2.6135	2546.59	3	2.6202	2540.34	3	2.6178	2542.67
weight	4	2.6148	2545.32	4	2.6182	2542.28	4	2.6149	2545.49
6.6555	5	2.6161	2544.05	5	2.6177	2542.77	5	2.6147	2545.68
	6	2.6132	2546.88	6	2.6167	2543.74	6	2.6158	2544.61
	7	2.6158	2544.35	7	2.6173	2543.16	7	2.6129	2547.44
	8	2.6141	2546.00	8	2.6153	2545.10	8	2.6142	2546.17
	9	2.6147	2545.42	9	2.6142	2546.17	9	2.6144	2545.98
	10	2.6143	2545.81	10	2.6164	2544.03	10	2.6147	2545.68
MU-32 4	1	3.4147	2503.24	1	3.4595	2472.26	1	3.4585	2472.98
	2	3.4283	2493.31	2	3.4607	2471.41	2	3.4622	2470.34
	3	3.4306	2491.63	3	3.4586	2472.91	3	3.4598	2472.05
weight	4	3.4304	2491.78	4	3.4582	2473.19	4	3.4589	2472.69
8.5478	5	3.4315	2490.98	5	3.4580	2473.34	5	3.4567	2474.27
	6	3.4307	2491.56	6	3.4573	2473.84	6	3.4571	2473.98
	7	3.4314	2491.05	7	3.4579	2473.41	7	3.4558	2474.91
	8	3.4319	2490.69	8	3.4589	2472.69	8	3.4555	2475.13
	9	3.4316	2490.91	9	3.4598	2472.05	9	3.4544	2475.91
	10	3.4332	2489.75	10	3.4577	2473.55	10	3.4541	2476.13

Tab. a-3: *continue*

Sample		1 min. Volume	Densità		3 min. Volume	Densità		5 min. Volume	Densità
MU-32 5	1	3.5546	2492.85	1	3.5829	2475.03	1	3.5820	2475.66
	2	3.5728	2480.16	2	3.5836	2474.55	2	3.5858	2473.03
	3	3.5725	2480.36	3	3.5839	2474.34	3	3.5853	2473.38
weight	4	3.5733	2479.81	4	3.5830	2474.97	4	3.5832	2474.83
8.8611	5	3.5734	2479.74	5	3.5826	2475.24	5	3.5827	2475.17
	6	3.5703	2481.89	6	3.5843	2474.07	6	3.5811	2476.28
	7	3.5752	2478.49	7	3.5828	2475.10	7	3.5804	2476.76
	8	3.5741	2479.25	8	3.5818	2475.79	8	3.5794	2477.45
	9	3.5740	2479.32	9	3.5811	2476.28	9	3.5789	2477.80
	10	3.5745	2478.98	10	3.5821	2475.59	10	3.5759	2479.88
MU-32 6	1	3.3329	2474.36	1	3.3500	2462.54	1	3.3468	2464.89
	2	3.3464	2464.38	2	3.3518	2461.21	2	3.3502	2462.39
	3	3.3480	2463.20	3	3.3519	2461.14	3	3.3493	2463.05
weight	4	3.3488	2462.61	4	3.3486	2463.57	4	3.3481	2463.93
8.2468	5	3.3483	2462.98	5	3.3502	2462.39	5	3.3471	2464.67
	6	3.3524	2459.97	6	3.3494	2462.98	6	3.3463	2465.26
	7	3.3517	2460.48	7	3.3488	2463.42	7	3.3448	2466.37
	8	3.3512	2460.85	8	3.3485	2463.64	8	3.3461	2465.41
	9	3.3539	2458.87	9	3.3477	2464.23	9	3.3452	2466.07
	10	3.3530	2459.53	10	3.3475	2464.38	10	3.3456	2465.78
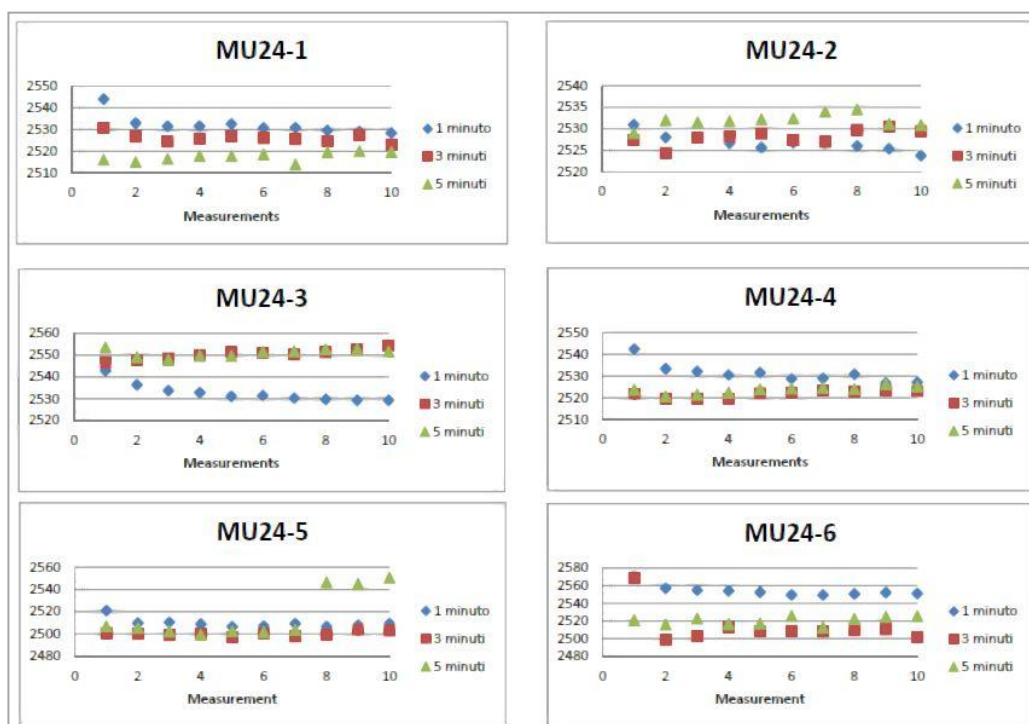
Fig. a-3: *Graphs show how at different purging time on the same sample values can change. Generally 3 min and 5 min after an early discrepancy were concordant*

Ultrasonic velocity:

When a surface is disturbed by a dynamic or vibratory load, three types of mechanical waves were created: I) compressional o P-waves (highest velocity); II) Shear o S-waves (in concrete usually have velocities equal to 60% respect to P-waves); III) Surface o Rayleight waves (55% velocity respect to P-waves).

The compressional wave velocity is given by:

$$V = (KE / \rho)^{\frac{1}{2}}$$

where:

V= compressional wave velocity

K= (1-μ)/(1+μ)(1-2μ)

E= dynamic modulus of elasticity

ρ=density

μ= dynamic Poisson's ratio

Velocity of propagation is strictly related with frequency *f* and wavelenght *λ* by *V=fλ*.

The dynamic modulus of elasticity (or Young modulus) is given by:

$$E = V^2 \rho \; \frac{(1+\mu)(1-2\mu)}{(1-\mu)}$$

where:

V = Velocity

ρ = Density

μ = Poisson ratio (0.15 for welded ignimbrite)

For these analyses a Controls' Ultrasonic Pulse Velocity Tester was used. The instrument consists of a 150 Khz pulse generator (introducing a wave pulse into the sample), a receiver and a display that signs the first time arrive of the waves (Fig. a-4). The measurements can be taken following three main geometry: I) direct transmission (transducers on opposite sample faces); ii) semi-directly (transducers on adjacent faces); iii) indirectly (transducers on the same face) (Karakus et al., 2005). In this work,

according with Binal (2009), ultrasonic velocity measurement were performed using the direct transmission method on opposite facies, on 23 cubic oriented samples. Calibration process were made using cylinder with knows arriving times. To standardize measurements, the samples were inserted inside a home-made support that permitted to apply an equal normal force upon sensors helping with a 3 kilograms iron plate. To calculate the standard deviations each measure was repeated three times.
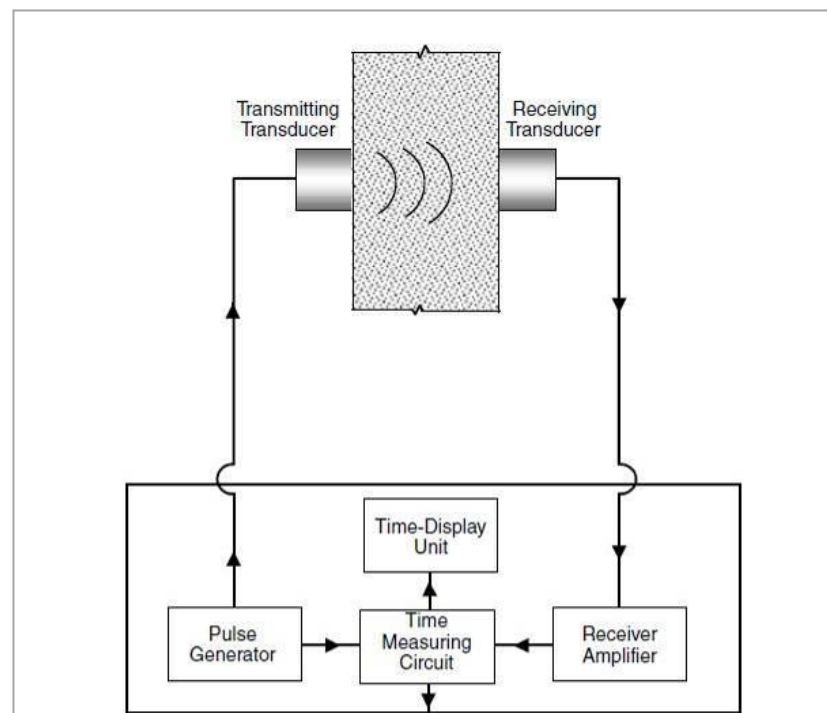
Fig. a-4: *Geometry of pulse velocity instrument (modif. from Naik et al 2004)*

Tab. a-4: Single ultrasonic velocity measurement on the three main directions

Sample		First cicle			Second cicle			Third cicle		
		Lenght (mm)	Time (μsec)	Speed (m/sec)	Lenght (mm)	Time (μsec)	Speed (m/sec)	Lenght (mm)	Time (μsec)	Speed (m/sec)
MU1	z	52.0	21.6	2407	52.0	21.2	2453	52.0	21.4	2430
	x	51.0	17.4	2931	51.0	17.2	2965	51.0	17.5	2914
	y	52.0	19.3	2694	52.0	18.4	2826	52.0	18	2889
MU3	z	52.0	25.9	2008	52.0	36.8	1413	52.0	23.9	2176
	x	50.0	20.2	2475	50.0	20.8	2404	50.0	19.4	2577
	y	52.0	19.9	2613	52.0	17.6	2955	52.0	18.5	2811
MU4	z	51.0	23.7	2152	51.0	21.5	2372	51.0	21.2	2406
	x	51.5	16.9	3047	51.5	16.1	3199	51.5	15.9	3239
	y	51.0	17.5	2914	51.0	17.1	2982	51.0	16.2	3148
MU24	z	43.0	10.8	3981	43.0	12.2	3525	43.0	11.5	3739
	x	42.0	11.3	3717	42.0	11.7	3590	42.0	10.9	3853
	y	42.0	10.8	3889	42.0	11.7	3590	42.0	10.9	3853
MU26	z	51.0	16.9	3018	51.0	14.3	3566	51.0	16.9	3018
	x	51.0	14.6	3493	51.0	14.0	3643	51.0	14.4	3542
	y	51.5	13.6	3787	51.5	23.3	2210	51.5	14.5	3552
MU31	z	39.5	12.9	3062	39.5	12.5	3160	39.5	12.5	3160
	x	40.0	11.6	3448	40.0	11.9	3361	40.0	11.7	3419
	y	39.0	12.8	3047	39.0	12.5	3120	39.0	12.3	3171
MU32	z	52.0	17.2	3023	52.0	16.8	3095	52.0	16.2	3210
	x	51.0	15.2	3355	51.0	14.1	3617	51.0	14.2	3592
	y	51.0	16.4	3110	51.0	15.0	3400	51.0	14.4	3542
MU36a	z	36.5	9.8	3724	36.5	9.2	3967	36.5	9.5	3842
	x	36.0	8.3	4337	36.0	8.4	4286	36.0	8.2	4390
	y	36.0	9.9	3636	36.0	9.2	3913	36.0	9.7	3711
MU37b	z	36.0	9.6	3750	36.0	10.2	3529	36.0	9.9	3636
	x	36.0	7.9	4557	36.0	8.7	4138	36.0	10.5	3429
	y	34.0	8.4	4048	34.0	8.7	3908	34.0	9.2	3696
MU42	z	42.0	29.4	1429	42.0	26.2	1603	42.0	17.2	2442
	x	44.0	18.4	2391	44.0	22.9	1921	44.0	20.2	2178
	y	45.5	16.9	2692	45.5	17.2	2645	45.5	17	2676
MU49	z	52.0	25.9	2008	52.0	35.8	1453	52.0	26.9	1933
	x	51.0	20.4	2500	51.0	19.1	2670	51.0	18.7	2727
	y	52.0	21.0	2476	52.0	20.6	2524	52.0	19.9	2613
MU50	z	52.0	17.7	2938	52.0	11.8	4407	52.0	12.2	4262
	x	51.0	11.9	4286	51.0	11.1	4595	51.0	12.2	4180
	y	52.0	11.9	4370	52.0	11.3	4602	52.0	13.4	3881
MU51	z	51.0	25.9	1969	51.0	23.5	2170	51.0	15.5	3290
	x	52.0	13.1	3969	52.0	12.5	4160	52.0	12.4	4194
	y	52.0	12.1	4298	52.0	12.3	4228	52.0	12.3	4228

Sample		First cicle			Second cicle			Third cicle		
		Lenght (mm)	Time (μsec)	Speed (m/sec)	Lenght (mm)	Time (μsec)	Speed (m/sec)	Lenght (mm)	Time (μsec)	Speed (m/sec)
MU52	z	52.0	16.4	3171	52.0	16.0	3250	52.0	15.2	3421
	x	52.0	14.3	3636	52.0	16.2	3210	52.0	14.7	3537
	y	52.0	13.9	3741	52.0	15.0	3467	52.0	15.1	3444
MU54	z	51.0	19.0	2684	51.0	18.1	2818	51.0	19.2	2656
	x	51.0	15.9	3208	51.0	14.5	3517	51.0	14.9	3423
	y	50.0	16.5	3030	50.0	16.0	3125	50.0	15.2	3289
MU56	z	51.0	19.5	2615	51.0	18.9	2698	51.0	18.4	2772
	x	50.5	16.5	3061	50.5	16.9	2988	50.5	16.2	3117
	y	50.5	18.2	2775	50.5	17.4	2902	50.5	17.2	2936
MU57	z	51.0	15.4	3312	51.0	15.2	3355	51.0	14.5	3517
	x	50.0	15.0	3333	50.0	13.7	3650	50.0	14.5	3448
	y	50.0	14.7	3401	50.0	13.9	3597	50.0	13.4	3731
MU58	z	51.0	21.5	2372	51.0	20.4	2500	51.0	20	2550
	x	52.0	19.9	2613	52.0	19.0	2737	52.0	18.2	2857
	y	52.0	18.4	2826	52.0	17.9	2905	52.0	17.5	2971
MU59	z	51.0	43.1	1183	51.0	16.8	3036	51.0	16.5	3091
	x	51.0	18.9	2698	51.0	17.6	2898	51.0	17.5	2914
	y	51.0	21.6	2361	51.0	17.6	2898	51.0	16.7	3054
MU30	z	26.0	11.2	2321	26.0	11.9	2185	26.0	11.2	2321
	x	26.5	12.2	2172	26.5	11.5	2304	26.5	11.5	2304
	y	24.0	10.0	2400	24.0	9.4	2553	24.0	9.4	2553

Tab. A-5: *Average values and errors of single measurements*

Sample		Mean		Median		Err. Rel Lenght (+- 0,5)	Err. Rel Speed (m/sec)	Err. Rel Time (μsec)	Dev.St. Speed (m/sec)	Dev.St. Time (μsec)	Var. Speed (m/sec)	Var. Time (μsec)
		Speed (m/sec)	Time (μsec)	Speed (m/sec)	Time (μsec)							
MU1	z	2430	21.40	2430	21.40	0.96	0.93	0.93	22.71	0.20	516	0.04
	x	2937	17.37	2931	17.40	0.98	0.87	0.86	25.90	0.15	671	0.02
	y	2803	18.57	2826	18.40	0.96	3.47	3.50	99.31	0.67	9863	0.44
MU3	z	1865	28.87	2008	25.90	0.96	20.44	22.34	400.74	6.94	16059	48.20
	x	2485	20.13	2475	20.20	1.00	2.05	1.49	87.19	0.70	32534	0.49
	y	2793	18.67	2811	18.50	0.96	6.11	6.16	171.45	1.16	29395	1.34
MU4	z	2310	22.13	2372	21.50	0.98	5.49	5.65	137.84	1.37	19001	1.86
	x	3162	16.30	3199	16.10	0.97	3.03	3.07	101.06	0.53	10213	0.28
	y	3015	16.93	2982	17.10	0.98	3.88	3.84	120.27	0.67	14465	0.44
MU24	z	3748	11.50	3739	11.50	1.16	6.09	6.09	228.59	0.70	52252	0.49
	x	3720	11.30	3717	11.30	1.19	3.54	3.54	131.76	0.40	17361	0.16
	y	3777	11.13	3853	10.90	1.19	3.96	4.04	163.39	0.49	26696	0.24
MU26	z	3201	16.03	3018	16.90	0.98	8.57	8.11	316.78	1.50	10035	2.25
	x	3559	14.33	3542	14.40	0.98	2.10	2.09	76.38	0.31	5834	0.09
	y	3183	17.13	3552	14.50	0.97	24.76	28.31	850.48	5.36	72331	28.72
MU31	z	3127	12.63	3160	12.50	1.27	1.57	1.58	56.57	0.23	3200	0.05
	x	3409	11.73	3419	11.70	1.25	1.27	1.28	44.21	0.15	1955	0.02
	y	3113	12.53	3120	12.50	1.28	1.99	1.99	62.26	0.25	3877	0.06

Sample		Mean Speed (m/sec)	Mean Time (μsec)	Median Speed (m/sec)	Median Time (μsec)	Err. Rel Lenght (+- 0,5)	Err. Rel Speed (m/sec)	Err. Rel Time (μsec)	Dev.St. Speed (m/sec)	Dev.St. Time (μsec)	Var. Speed (m/sec)	Var. Time (μsec)
MU31	z	3127	12.63	3160	12.50	1.27	1.57	1.58	56.57	0.23	3200	0.05
	x	3409	11.73	3419	11.70	1.25	1.27	1.28	44.21	0.15	1955	0.02
	y	3113	12.53	3120	12.50	1.28	1.99	1.99	62.26	0.25	3877	0.06
MU32	z	3109	16.73	3095	16.80	0.96	1.16	2.99	94.12	0.50	8858	0.25
	x	3521	14.50	3592	14.20	0.98	3.72	3.79	144.34	0.61	20833	0.37
	y	3350	15.27	3400	15.00	0.98	6.45	6.55	220.17	1.03	48476	1.05
MU36a	z	3845	9.50	3842	9.50	1.37	3.16	3.16	121.47	0.30	14755	0.09
	x	4338	8.30	4337	8.30	1.39	1.20	1.20	52.27	0.10	2732	0.01
	y	3754	9.60	3711	9.70	1.39	3.69	3.65	143.10	0.36	20476	0.13
MU37b	z	3639	9.90	3636	9.90	1.39	3.03	3.03	110.31	0.30	12169	0.09
	x	4041	9.03	4138	8.70	1.39	13.96	14.39	570.39	1.33	32534	1.77
	y	3884	8.77	3908	8.70	1.47	1.80	4.56	177.23	0.40	31412	0.16
MU42	z	1824	24.27	1603	26.20	1.19	27.77	25.14	541.73	6.33	29346	40.01
	x	2164	20.50	2178	20.20	1.14	10.86	10.98	235.29	2.26	55363	5.13
	y	2671	17.03	2676	17.00	1.10	0.88	0.88	23.89	0.15	571	0.02
MU49	z	1798	29.53	1933	26.90	0.96	15.44	16.76	301.32	5.45	90796	29.70
	x	2632	19.40	2670	19.10	0.98	4.32	4.38	118.23	0.89	13978	0.79
	y	2538	20.50	2524	20.60	0.96	2.70	2.68	69.44	0.56	4822	0.31
MU50	z	3869	13.90	4262	12.20	0.96	18.98	21.22	809.61	3.30	65546	10.87
	x	4354	11.73	4286	11.90	0.98	4.76	4.69	215.30	0.57	46355	0.32
	y	4284	12.20	4370	11.90	0.96	8.42	8.61	368.15	1.08	13553	1.17
MU51	z	2477	21.63	2170	23.50	0.98	26.67	24.04	711.89	5.45	50678	29.65
	x	4108	12.67	4160	12.50	0.96	2.73	2.76	120.86	0.38	13553	0.14
	y	4251	12.23	4228	12.30	0.96	0.82	0.82	40.34	0.12	1628	0.01
MU52	z	3281	15.87	3250	16.00	0.96	3.82	3.78	127.93	0.61	16367	0.37
	x	3461	15.07	3537	14.70	0.96	6.16	6.31	223.22	1.00	49827	1.00
	y	3550	14.67	3467	15.00	0.96	4.19	4.09	165.42	0.67	27363	0.44
MU54	z	2719	18.77	2684	19.00	0.98	2.97	2.93	86.27	0.59	7443	0.34
	x	3383	15.10	3423	14.90	0.98	4.58	4.64	158.73	0.72	25195	0.52
	y	3148	15.90	3125	16.00	1.00	4.12	4.09	131.14	0.66	17198	0.43
MU56	z	2695	18.93	2698	18.90	0.98	2.90	2.90	78.23	0.55	6120	0.30
	x	3055	16.53	3061	16.50	0.99	2.11	2.12	64.72	0.35	4189	0.12
	y	2871	17.60	2902	17.40	0.99	2.81	2.84	85.09	0.53	7240	0.28
MU57	z	3395	15.03	3355	15.20	0.98	3.03	2.99	108.31	0.47	11731	0.22
	x	3477	14.40	3448	14.50	1.00	4.55	4.51	160.11	0.66	25634	0.43
	y	3577	14.00	3597	13.90	1.00	4.61	4.64	165.95	0.66	27538	0.43
MU58	z	2474	20.63	2500	20.40	0.98	2.58	3.63	91.75	0.78	8419	0.60
	x	2736	19.03	2737	19.00	0.96	4.46	4.47	122.04	0.85	14894	0.72
	y	2901	17.93	2905	17.90	0.96	2.51	2.51	72.76	0.45	5294	0.20
MU59	z	2437	25.47	3036	16.80	0.98	39.14	52.23	1085.78	15.27	11789	233.22
	x	2837	18.00	2898	17.60	0.98	3.80	3.89	120.14	0.78	14434	0.61
	y	2771	18.63	2898	17.60	0.98	12.50	13.15	363.38	2.61	13204	6.80
MU30	z	2276	11.43	2321	11.20	1.92	3.00	3.06	78.84	0.40	6216	0.16
	x	2260	11.73	2304	11.50	1.89	2.92	2.98	76.34	0.40	5827	0.16
	y	2502	9.60	2553	9.40	2.08	3.06	3.13	88.45	0.35	7823	0.12

REFERENCES

Andrews G.D.M. and Branney M.J.(2010) Emplacement and rheomorphic deformation of a large, lava–like rhyolitic ignimbrite Grey's Landing, southern Idaho. Geological Society of America Bulletin v. 123 (3-4):725-743.

Andrews G.D.M., Branney M.J., Bonnichsen B., McCurry M.(2008) Rhyolitic ignimbrites in the Rogerson Graben, southern Snake River Plain volcanic province: volcanic stratigraphy, eruption history and basin evolution. Bull. Volcanol. 70:269-291.

Andrews G.D.M. (2006) The emplacement and deformation of high-temperature tuffs:a structural analysis of the Grey's Landing ignimbrite, Snake River Plain, Idaho. Phd thesis. Department of Geology. University of Leicester.

Assorgia A., Brotzu P., Morbidelli L., Nicoletti E., Traversa G. (1984) Successione e cronologia K/Ar degli eventi vulcanici del complesso calco-alcalino Oligo-Miocenico dell'Arcuentu (Sardegna centro-occidentale). Per. Mineral. 53:89-102.

Assorgia A., Fadda, A., Gimeno D., Morra V., Ottelli L., Pujolriu L.L., Secchi F.A., (1992). Tectono-sedimentary evolution of the upper tertiary volcanic succession of Sulcis area (SW Sardinia, Italy). Paleontol. Evol. 24–25, 307–320.

Assorgia A., Fadda A., Gimeno Torrente D., Morra V., Ottelli L., Secchi F.A., (1990). Le successioni ignimbritiche terziarie del Sulcis (Sardegna sud-occidentale). Mem. Soc. Geol. Ital. 45, 951– 963. Beccaluva, L., Civetta, L., 1985. Geochronology in Sardinia: results and problems. Rend. Soc. Ital. Mineral. Petrol. 40, 57– 72.

Barca S., Carmignani L., Oggiano G., Pertusati P. C., Salvadori I., Conti P., Eltrudis A., Funedda A., Pasci S. (1996) - Carta geologica della Sardegna (scala 1:200.000). Serv Geol. d'It., L.A.C. - Firenze.

Bardintzeff J.M. (1984) Merapi volcano (Java, Indonesia) and Merapi-type nueè ardente. Bull Volcanol. 47:433-446.

Beccaluva L., Brotzu P., Macciotta G., Morbidelli L., Serri G., Traversa G., (1987) Cenozoic tectono-magmatic evolution and inferre mantle sources in the Sardo-Tyrhenian area. In: "The lithosphere in Italy:Advances in earth science research". Accad. Naz. Lincei 80:229-248.

Bindeman I.N., Valley J.W. (2003) Rapid generation of both high- and low-$\delta 18O$, large-volume silicic magmas at the Timber Mountain / Oasis Valley calderacomplex, Nevada. Geol Soc Am Bull 15:581-595.

Bonnichsen B., Citron G.P. (1982) The Cougar Point Tuff, southwestern Idaho. In: Bonnichsen B, Breckinridge RM (eds) Cenozoic Geology of Idaho. Idaho Bur Min Geol Bull 26:255-281.

Branney M.J., Kokelaar B.P. (1992) A reappraisal of ignimbrite emplacement: progressive aggradation and changes from particulate to non-particulate flow during emplacement of high-grade ignimbrite. Bull Volcanol 54:504-520.

Branney M.J., Kokelaar, B.P. (2002) Pyroclastic density currents and the sedimentation of ignimbrites. Geol Soc Mem 27.

Branney M.J., Barry T.L., Godchaux MM (2004) Sheath folds in rheomorphic ignimbrites. Bull Volcanol 66:485-491.

Bryan, S.E., Martí, J., Kas, F.A.F. 1998. Stratigraphy of the B&as del Sur ormation. an extracaldera record of Quaternary phonolitic explosive eruptions from the Las Cañadas edifice, Tenerife .Canary Islands. Geological Magazine,v. 135, p. 605–636.

References

Bursik M.I., Woods A.W. (2000) The effects of topography on sedimentation from particle-laden turbulent density currents. Journ Sediment. Res. 70(1):53-63.

Capaccioni B., Cuccoli F. (2005) Spatter and welded air fall deposits generated by fire-fountaining eruptions: cooling of pyroclasts during transport and deposition. J Volcanol Geotherm Res 145:263-280.

Carey S.N. (1991) Transport and deposition of tephra by pyroclastic flows and surges. In: Fisher RV, Smith GA (eds) Sedimentation in volcanic settings SEPM Spec Publ 45:39-57.

Carmignani L., Oggiano G., Barca S., Conti P., Salvatori I., Eltrudis A., Funedda A., Pasci S. (2001) Geologia della Sardegna. Note illustrative della Carta Geologica della Sardegna a scala 1:200.000. Mem. Descr. Carta Geolol. It., 60, 283 pp.

Carmignani L., Decandia F.A., Disperati L., FantozziP., Lazzarotto A., Liotta D., Oggiano G., Tavarnelli E. (1995) Relazioni tra il bacino balearico, il Tirreno settentrionale e l'evoluzione neogenica dell'Appennino settentrionale. Studi Geologici Camerti, Vol.Spec. 1:255-268.

Carmignani L., Barca S., Disperati L., Fantozzi P., Funedda A., Oggiano G., Pasci S. (1994) Tertiary compression and extension in the Sardinian basement. Boll. Geof. Teorica Appl. 36(141-144): 45-62.

Carminati E., Lustrino M., Doglioni C. (2012) Geodynamic evolution of the central and western Mediterranean: Tectonics vs. igneous petrology constraints. Tectonoph. doi:10.1016/j.tecto.2012.01.026.

Cas R.A.F., Wright J.V. (1987) Volcanic successions: modern and ancient. Allen and Unwin, London, 529 pages.

Chapin C.E., Lowell G.R. (1979) Primary and secondary flow structures in ash-flow tuffs of the Gribbles Run palaeovalley, central Colorado. In: Chapin CE, Elston WE (eds) Ash-flow tuffs. Geol Soc Am Sp Pap 180:137-154.

Cioni R., Gurioli L., Lanza R., Zanella E. (2004) Temperature of the A.D. 79 pyroclastic density current deposits (Vesuvius, Italy). Journ. Geophys Res 109:B02207. doi:10.1029/2002JB002251

Cioni R., Salaro L., Pioli L. (2001) The Cenozoic volcanism of San Pietro Island (Sardinia, Italy). Rend. Sem. Sc. Univ. Cagliari 71(2):149-163.

Cole P.D., Calder E.S., Druitt T.H., Hoblitt R., Robertson R., Sparks R.S.J., Young S.R. (1998) Pyroclastic flows generated by gravitational instability of the 1996-97 lava dome of Soufriere Hills Volcano, Montserrat. Geoph Research Lett. 25:3425-3428.

Costa A. (2005) Viscosity of high crystal content melts: Dependence on solid fraction. Geoph. Researc. Lett. 32(22) DOI: 10.1029/2005GL024303.

Cox K.G., Bell J.D., Pankhurst R.J. (1979) The Interpretation ofIgneous Rocks. George, Allen and Unwin, London.

Davis B.K., McPhie J. (1996) Spherulites, quench fractures and relict perlite in a Late Devonian rhyolite dyke, Queensland, Australia. Journ. Volcanol. Geoth. Res. 71(1):1-11.

Dingwell D.B. (1998) Recent experimental progress in the physical description of silicic magma relevant to explosive volcanism. In: Gilbert JS, Sparks RSJ (eds) The physics of explosive volcanic eruptions. Geol Soc Lon Spec Pub 145:9-26.

Dingwell D.B., Hess K.U. (1998) Melt viscosities in the system Na-Fe-Si-O-F-Cl: contrasting effects of F and Cl in alkaline melts. Am Mineral 83:1016-1021.

Druitt T. H. (1998) Pyroclastic density currents. In: The physics of explosive volcanic eruptions. Ed. Gilbert J.S. and Sparks R.S., Geological Society Special Pubblication 145:145-182.

References

Fisher R.V. (1986) Systems of transport and deposition within pyroclasticsurges: evidence from Mount St. Helens, Washington.EOS Trans Am Geophys Union 67:1246.

Fisher R.V., Schminke H.U. (1984) Pyroclastic rocks. New York, Springer-Verlag p.472.

Freundt A.(1999) Formation of high-grade ignimbrites; 2: A pyroclastic suspension current model with implications also for low-grade ignimbrites.Bull Volc 60:545-567.

Freundt A. (1998) The formation of high-grade ignimbrites; 1: Experiments on high- and low-concentration transport systems containing sticky particles. Bull Volc 59:414-435.

Freundt A., Bursik M. (1998) Pyroclastic flow transport mechanism. In: From Magma to Tephra. Ed. Freunt A. and Rosi M., Elselvier, pp 336.

Freundt A., Schminke H.U. (1995) Eruption and emplacement of a basaltic welded ignimbrite during caldera formation on Gran Canaria. Bull Volc 56:640-659.

Garbarino C., Maccioni L. (1968) – Contributo sulla conoscenza delle vulcaniti dell'Isola di S.Pietro (Sardegna sud-occidentale) Nota I: Le comenditi – Periodico di Mineralogia, 37, 895-1018.

Gattacceca J., Deino A., Rizzo R., Jones D.S., Henry B., Beaudoin B., Vadeboin F. (2007) Miocene rotation of Sardinia: new paleomagnetic and geochronological constraints and geodynamic implications. Earth Plan Sc. lett 258:359-377.

Gattacceca J., Rochette P. (2001) Pseudopaleosecular variation due to remanence anisotropy in a pyroclastic flow succession, Geophys. Res. Lett. 29, doi:10.1029/2002GL014697.

Gibson I.L. (1974). Blister caves associated with an Ethiopian ash-flow tuff. Studies in speleology, 2(6):225-232.

Giordano D., Russell J.K., Dingwell D.B. (2008). Viscosity of magmatic liquids: A model. Earth and Planetary Science Letters 271 123–134.

Giordano D., Nichols A.R.L., Dingwell D.B. (2005) Glass transition temperatures of natural hydrous melts: a relationship with shear viscosity and implications for the welding process. J Volcanol Geotherm Res 142:105-118.

Gosh S.K., Ramberg H. (1976) Reorientation of inclusions by combination of pure and simple shear. Tectonophysics 34:1-70.

Grunder A.L., Laporte D., Druitt T.H. (2005) Experimental and textural investigation of welding: effects of compaction, sintering, and vapour-phase crystallization in the rhyolitic Rattlesnake Tuff. J Volcanol Geotherm Res 142:89-104.

Hoblitt R.P., (1986) Observation of the eruptions of July 22 and August 7, 1980 at Mount St. Helens, Washington. US Geological Survey Prof. Paper 1335:1-44.

Johnson A.M. (1970) Physical processes in Geology. Freeman, San Francisco, CA.

Kirstein L.A., Hawkesworth C.J., Garland F.G. (2001) Felsic lavas or rheomorphic ignimbrites: is there a chemical distinction? Cont Mineral Petrol 142:309-322.

Kobberger G., Schminke H.U. (1999) Deposition of rheomorphic ignimbrite D (Mogán Formation), Gran Canaria, Canary Islands, Spain. Bull Volcanol 60:465-485.

Lacombe O., Jolivet L. (2005) Structural and kinematic relationships between Corsicaand the Pyrenees–Provence domain at the time of the Pyrenean orogeny. Tectonics24, TC1003. doi:10.1029/2004TC001673.

Le Bas M.J., Le Maitre R.W., Streckeisen A., Zanettin B., and IUGS Subcommission on the Systematics of Igneous Rocks (1986) A chemichal classification of volcanic rocks based on the Total Alkali-Silica diagram. Journ. Petrol.27(3):745-750.

References

Lecca L., Lonis R., Luxoro S., Melis E., Secchi F., Brotzu P. (1997). Oligo-Miocene volcanic sequences and rifting stages in Sardinia: a review. Period. Mineral. 66, 7 –61.

Lesti C., Porreca M., Giordano G., Mattei M., Cas R.A.F., Wright H.M.N., Folkes C.B., Viramonte J. (2011) High-temperature emplacement of the Cerro Galàn and Toconquis Group ignimbrites (Puna plateau, NW Argentina) determined by TRM analyses. Bull. Volc.73:1535-1565

Lustrino M., Morra V., Fedele L., Franciosi L. (2009) The beginning of the Apennine subduction system in central-western Mediterranean: constraints from Cenozoic "orogenic" magmatic rocks of Sardinia (Italy). Tectonics 28. doi:10.1029/2008TC002419.

McArthur A.N., Cas R.A.F., Orton G.J. (1998). Distribution and significance of crystalline, perlitic and vesicular textures in the Ordovician Garth Tuff (Wales). Bull. Volcanol. 60, 260– 285.

McClelland E.A., Wilson C.J.N., Bardot L. (2004) Paleotemperature determinations for the 1.8 ka Taupo ignimbrite, New Zealand, and implications for the emplacement history of a high-velocity pyroclastic flow. Bull. Volc 66:492-513

McClelland E.A,, Druitt T.H. (1989) Paleomagnetic estimates of emplacement temperatures of pyroclastic deposits on Santorini, Greece. Bull Volc 51:16-27

McPhie J., Doyle M., Allen R. (1993) Volcanic textures, a guide to the interpretation of textures in volcanic rocks.

Morra V., Secchi F.A., Assorgia A. (1994). Petrogenetic significance of peralkaline rocks from Cenozoic calc-alkaline volcanism from SW Sardinia, Italy. Chem. Geol. 118, 109– 142.

Mountigny R., Edel J.B., Thuizat R. (1981) Oligo-Miocene rotation of Sardinia: K-Ar Ages and paleomagnetic data of Tertiary volcanics. Earth Planet Sc. Letters 54:261-271.

Mulas M., Mundula F., Cioni R. (2011) Stratigraphy of the rheomorphic, densely welded, Monte Ulmus Ignimbrite (SW Sardinia, Italy). Acta Vulcanologica 23(1-2): 15-24. (in press).

Mundula F., Cioni R., Rizzo R. (2009) A simplified scheme for the description of textural features in Welded Ignimbrites: the example of San Pietro Island (Sardinia, Italy). Italian journal of Geosciences 128(3):615-627.

Mundula F., Cioni R., Mulas M. (submitted) Diapirism and rheomorphic structures in densely welded ignimbrites: the "Serra di Paringianu" ignimbrite (Sardinia, Italy).

Naik T.R., Mohan Malhotra V., Popovics J.S. (2002) The ultrasonic pulse velocity method. Handbook on Nondestructive Testing of Concrete , VM Malhotra and NJ Carino(eds.),2nd ed. , Chapter 8 . CRC Press , Boca Raton , FL.

Pasci S., Pioli L., Pisanu G., Rosi M., Sale V., Benvenuti E., Laurenzi M., (2001) Tettonica e vulcanismomiocenici nel Sulcis (Sardegna SW), Abstract in Geoitalia, III FIST meeting, 5–8 September 2001,Chieti (Italy), 2001.

Passchier C.W., Trouw R.A.J. (2005) Microtectonics. Springer Verlag, Berlin pp366.

Passchier C.W., Trouw R.A.J. (1996) Microtectonics. Springer Verlag, Berlin, 290 pages.

Pecerillo A., Taylor S.R. (1976) Geochemistry of Eocene calc-alkaline volcanic rocks from the Kastamuonu area, northern Turkey. Contrib. Mineral. Petrol. 58:63-81.

References

Pioli L., 2002. High-grade ignimbrites from the Sulcis volcanic district (SW Sardinia, Italy): the example of Nuraxi tuff. PhD thesis, Dipartimento di Scienze della Terra, University of Pisa.

Pioli L., Rosi M. (2005) Rheomorphic structures in a high-grade ignimbrite: the Nuraxi Tuff, Sulcis volcanic district (SW Sardinia, Italy). J Volcanol Geotherm Res 142:11-28 Pioli, 2003.

Pioli L., Rosi M. (2008) Magnetic fabric, welding texture and strain fabric in the Nuraxi Tuff, Sardinia, Italy. Bull. Volcanolog 70:1123-1137.

Quane S.L., Russell J.K. (2005) Ranking welding intensity in pyroclastic deposits. Bull Volcanol 67:129-143.

Riehle J.R., Miller T.F., Bailey R.A. (1995) Cooling, degassing, and compaction of rhyolitic ash-flow tuffs: a computational model. Bull Volcanol 57:319-336.

Riehle J.R., Miller T.F., Paquereau-Lebti P. (2010). Compaction profiles of ash-flow tuffs: Modeling versus reality. Journal of Volcanology and Geothermal Research 195:106–120.

Rodriguez-Losada J.A., Hernandez-Gutierrez L.E., Lomoschitz Mora-Figueroa A. (2007) Geothecnical features of the welded ignimbrites of Canary Islands. In: Volcanic Rocks. Malheiro & Nunes Eds. (ISBN 978-0-415-45140-6) pg 29-33.

Ronga F. (2010) Petrogenesi delle vulcaniti del Sulcis (Sardegna Sud-occidentale). Phd thesis (XXIII). Università degli Studi di Catania.

Rosenbaum G., Lister G.S., Duboz C. (2002), Reconstruction of the tectonic evolution of the western Mediterranean since the Oligocene, J. VirtualExplorer, 8:107–130.

Ross C.S., Smith R.L. (1961) Ash-flow tuffs: their origin, geologic relations and identification. US Geol Surv. Prof. Pap 366:1-81.

Nakamura, N. (1974) Determination of REE, Ba, Fe, Mg, Ba, and K in carbonaceous and ordinary chondrites, Geochim. Cosmochim. Acta, 38: 757-775.

Savelli C., Beccaluva L., Deriu M., Macciotta G., Maccioni L. (1979) K/Ar geochronology and evolution of the Tertiary "calcalkalic" volcanism of Sardinia (Italy). Journ. Volc. Geotherm. Res. 5:257-269.

Savelli C. (2002) Time-space distribution of magmatic activity in the western Mediterranean and peripheral orogens during the past 30 Ma (a stimulus to geodynamic considerations). Journal of Geodynamics 34:99-126.

Schmincke H.U., Sumita M. (2010) Geological evolution of the Canary Islands. Görres Verlag, Koblenz, pp 1–196.

Schmincke H.U. (1982) Volcanic and chemical evolution of the Canary Islands. In Geology of the northwest African margin, U. Von Rad, K. Hinz, M. Sarnthein, E. Seibold. eds., 273–306. Springer.

Schmincke H.U. (1974) Volcanological aspects of peralkaline silicic welded ashflow tuffs. Bull Volcanol 38:594-636.

Sheridan M.F., Wang Y. (2005) Cooling and welding history of the Bishop Tuff in Adobe Valley and Chidago Canyon, California. J Volcanol Geotherm Res 142:119-144.

Smith R.L. (1960a) Ash flows. Geol Soc Am Bull 71:795-841.

Smith R.L. (1960b) Zones and zonal variations in welded ash-flows. US Geol Surv Prof Pap 354-F: 149-158. In: New Mex Geol Soc Spec Pub (1980).

Sparks R.S.J, Tait S.R., Yanev Y. (1999) Dense welding caused by volatile resorption. J Geol Soc Lon 156:217-225.

Sparks R. S. J. (1976). Grain size variations in ignimbrites and implications for the transport of pyroclastic flows. Sedimentology, 23:147-188.

References

Sparks R.S.J., Self S., Walker G.P.L. (1973) Products of ignimbrite eruptions. Geology 1:115-118.

Speranza F., Villa I.M., Sagnotti L., Florindo F., Cosentino D., Cipollari P., Mattei M. (2002) Age of the Corsica-Sardinia rotation and Liguro-Provencal basal spreading: new paleomagnetic and Ar/Ar evidence. Tectonophys. 347:231:251.

Stevenson D.S., Bagdassarov N.S., Dingwell D.B., Romano C. (1998) The influence of trace amounts of water on the viscosity of rhyolites. Bull Volcanol 60:89-97.

Stevenson R.J., Dingwell D.B., Webb S.L., Sharp T.G. (1996) Viscosity of microlite bearing rhyolitic obsidians: an experimental study. Bull Volcanol 58:298-309.

Streck M.J., Grunder A.L. (1995) Crystallization and welding variations in a widespread ignimbrite sheet - the Rattlesnake Tuff, Eastern Oregon, USA. Bull Volcanol 57:151-169.

Sumner J.M., Branney M.J. (2002) The emplacement history of a remarkable heterogeneous, chemically zoned, rheomorphic and locally lava-like ignimbrite: 'TL' on Gran Canaria. J Volcanol Geotherm Res 115:109-138.

Taricco M. (1934). Geologia del foglio Isola di San Pietro-Capo Sperone. Boll. R. Uff. Geol. It. 59(2):1-78.

Thomas R.M.E., Sparks R.S.J. (1992) Cooling of tephra during fallout from eruption columns. Bull Volcanol 54:542-553.

Tikoff B. and Fossen H. (1993) Simultaneous pure and simple shear, the unifying deformation matrix. Tectonophysics 217; 267-283.

Twiss R.J., Moore E.M. (1992) Structural geology. Freemen Press, New York, 532 pages.

Valentine G.A., Perry F.V., WoldeGabriel G. (2000) Field characteristics of deposits from spatter-rich pyroclastic density currents at Summer Coon volcano, Colorado. Journ Volc. Geoth. Researcg 104:187-199.

Ventura G. (2001) The strain path and emplacement mechanism of lava flows: an example from Salina (southern Tyrrhenian Sea, Italy). Earth and Planetary Sciences Letters 188; 229-240.

Walker G.P.L. (1983) Ignimbrite types and ignimbrite problems. J Volcanol Geotherm Res 17:65-88.

Wilson L., Head, J.W. (1981). Morphology and theology of pyroclastic flows and their deposits, and guidelines for future observations. In. Lipman, P. W. & Mullineaux, D. R. (eds) The 1980 Eruptions of Mount St Helens, Washington, USA. US Geological Survey, Professional Papers, 1250:513-524.

Wolff J.A., Wright J.V. (1981) Rheomorphism of welded tuffs. J Volcanol Geotherm Res 10:13-34.

Wright J.V., Walker, G.P.L. (1981). Eruption, transport and deposition of ignimbrite - a case study from Mexico. Journ. Volcanol.Geoth. Res., 9:111-131.

Zanella E., Gurioli L., Lanza R., Sulpizio R., Bontempi M. (2008) Deposition temperatures of the AD 472 Pollena pyroclastic density current deposits, Somma-Vesuvius, Italy. Bull. Volcanol. DOI 10.1007/s00445-008-0199-9